Epitaxial Hexagonal Boron Nitride: from Color Centers to Wafer Scale Heterostructures

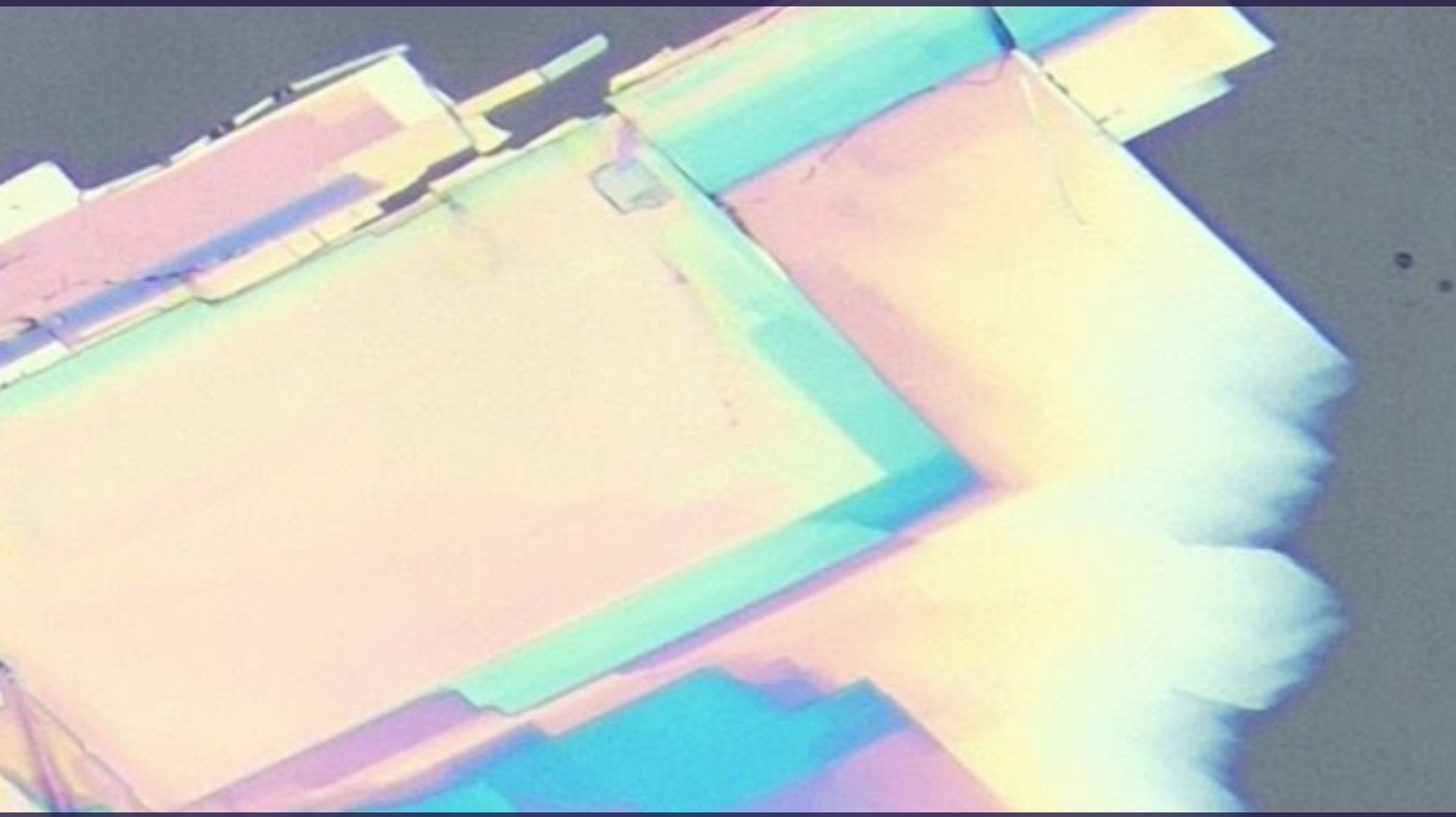

PhD Thesis

by

Katarzyna Ludwiczak

Warsaw 2025

Epitaxial Hexagonal Boron Nitride: from Color Centers to Wafer Scale Heterostructures

A DISSERTATION PRESENTED
BY
Katarzyna Ludwiczak

IN FULFILLMENT OF THE REQUIREMENTS
FOR THE DEGREE OF
Doctor of Philosophy
IN THE SUBJECT OF
Physical Sciences

Thesis advisors: Dr hab. Johannes Binder
and Prof. Dr hab. Andrzej Wysmołek

Faculty of Physics, University of Warsaw
Warsaw, Poland
June, 2025

Epitaxial Hexagonal Boron Nitride: from Color Centers to Wafer Scale Heterostructures

Abstract

In recent years, hexagonal boron nitride (hBN) has established its position among two dimensional materials as an irreplaceable component of ultrathin heterostructures. Owing to its high durability, wide bandgap, and flat surface with ideally no dangling bonds, it was found to improve the performance and provide protection for other van der Waals crystals. The material has also gathered a lot of attention due to its potential use in quantum technological applications. Point defects in the atomic structure of hexagonal boron nitride can be optically active. The emission from such color centers can be highly sensitive to local environmental properties like strain, electric and magnetic field, making them promising candidates for nanosensors.

This thesis addresses the topic of hBN applications and properties in two ways: on a macro- and nano-scale. In the studies, we use large-area, ultrathin material grown by Metalorganic Vapor Phase Epitaxy (MOVPE) to fabricate heterostructures with other two-dimensional materials.

Chapters from 1 to 4 present the motivation, the theoretical background, and the overview of studied materials, as well as fabrication and characterization methods. Chapter 5 describes the experimental setups used and the developed large-area transfer technique, which is key to other elements of the work.

In chapter 6, we present a combined heteroepitaxial growth method aimed at the large-area fabrication of high optical quality monolayers of molybdenum diselenide ($MoSe_2$) - a representative of 2D material semiconductors. We tested the utility of epitaxial hBN as a substrate that improves the performance of the subsequently grown monolayer crystal. Our studies include two approaches: $MoSe_2$ growth on as-grown and on transferred hBN layers. Morphology, structural, and optical spectroscopy studies unveil a high uniformity and repeatability of fabricated samples. Photoluminescence measurements performed at low temperatures show a high optical quality of the grown $MoSe_2$ layers manifested by narrow and resolved excitonic lines. An additional transfer step of the hBN layer onto a silicon/silicon dioxide substrate allowed us to perform electrical gating of the structures, which enabled control of the well-resolved $MoSe_2$ charged-to-neutral exciton intensity ratio.

In chapter 7, we delve into the nanoscale interactions between 2D magnets and color centers in epitaxial hBN. We show the fabrication scheme and challenges related to the stability of the heterostructures. Optical studies allow us to characterize defects typically found in untreated epitaxial layers. Spectroscopy measurements performed with varying temperature resulted in an intriguing observation of a change in defect-related emission energy and a cut-off correlated with an antiferromagnetic-paramagnetic phase transition in a 2D magnet, chromium thiophosphate. Further studies performed in an external magnetic field showed additional interesting effects. At a magnetic field corresponding to the so-called spin-flop

transition in a 2D magnet, the intensity of the hBN color center emission drastically drops, and its energy slightly shifts. We discuss the origin of the observed phenomena, considering mechanical strain and/or changes in an electric and magnetic field as possible explanations. Studies of the hBN/2D magnet heterostructures are supplemented by the results of polarization-resolved optical probing. We present the angular dependencies collected at various magnetic fields for the Raman signal of a 2D magnet and the hBN defect-related emission, which provides valuable information about the symmetry of the electronic states involved in the investigated optical properties.

The thesis is concluded in chapter 8, pointing out opportunities for further development and applications of the presented research.

The described results show that hBN is a prospective material that can already be scaled up and used in macro-sized heterostructures and devices. Simultaneously, hBN provides a great platform for studying basic physical phenomena related to 2D semiconductor systems on the nanoscale. The presented findings, considering color centers in hBN and their interaction with 2D magnets, open a wide path to applications related to quantum technologies and sensing, while the combined growth of $MoSe_2$ on hBN holds great promise for scaling up van der Waals heterostructure fabrication.

Epitaksjalny Heksagonalny Azotek Boru: od Centrów Barwnych po Wielkopowierzchniowe Heterostruktury

Streszczenie

W ostatnich latach heksagonalny azotek boru (hBN) ugruntował swoją pozycję wśród materiałów dwuwymiarowych (2D) jako niezastąpiony element ultracienkich heterostruktur. Ze względu na wysoką trwałość, szeroką przerwę pasmową i płaski iterfejs bez tzw. wolnych wiązań, może on poprawiać własności i zapewniać ochronę innym kryształom van der Waalsa. hBN przyciągnął również wiele uwagi ze względu na jego potencjalne zastosowanie w rozwoju technologii kwantowych. Punktowe defekty w strukturze atomowej heksagonalnego azotku boru mogą być czynne optycznie. Emisja z takich centrów barwnych może być wysoce wrażliwa na lokalne warunki, takie jak naprężenia czy pole elektryczne i magnetyczne, czyniąc je obiecującymi kandydatami do budowy nanosensorów.

Niniejsza praca podejmuje temat zastosowań i właściwości hBN na dwóch skalach: makro i nano. W opisywanych badaniach wykorzystujemy wielkopowierzchniowy, ultracienki materiał wytworzony metodą Epitaksji z Fazy Gazowej ze Związków Metaloorganicznych (eng. MOVPE) do wytwarzania heterostruktur hBN z innymi materiałami 2D.

Rozdziały od 1 do 4 przedstawiają motywację, podstawy teoretyczne i przegląd badanych materiałów, a także metody ich wytwarzania i charakteryzacji. Rozdział 5 opisuje wykorzystane układy pomiarowe, a także opracowaną technikę transferu wielkopowierzchniowych warstw hBN, która jest kluczowa dla innych elementów pracy.

W rozdziale 6 przedstawiamy heteroepitaksjalną metodę wzrostu, mającą na celu wytwarzanie wielkopowierzchniowych monowarstw diselenku molibdenu ($MoSe_2$), przedstawiciela dwuwymiarowych półprzewodników, o wysokiej jakości optycznej. Przetestowaliśmy funkcjonalność epitaksjalnych warstw hBN jako podłoża, które poprawia jakość kolejno hodowanych monowartw. Nasze badania obejmują dwa podejścia: wzrost $MoSe_2$ bezpośrednio na wyhodowanych metodą MOVPE warstwach hBN, a także na warstwach hBN transferowanych na inne podłoża. Badania morfologii, struktury i własności optycznych ujawniają wysoką jednorodność i powtarzalność wytworzonych próbek. Pomiary fotoluminescencji wykonane w niskich temperaturach wykazują wysoką jakość optyczną hodowanych warstw $MoSe_2$, przejawiającą się wąskimi i rozdzielonymi liniami ekscytonowymi. Transfer warstw hBN na podłoża krzem/dwutlenek krzemu pozwolił na elektryczne bramkowanie struktur i umożliwił kontrolę stosunku intensywności naładowanego do neutralnego ekscytonu $MoSe_2$.

W rozdziale 7 przedstawiamy badania nad interakcjami w skali nano pomiędzy magnesami 2D i centrami barwnymi w epitaksjalnych warstwach hBN. Przedstawiamy schemat wytwarzania próbek i wyzwania związane z niską stabilnością heterostruktur. Badania optyczne pozwalają nam scharakteryzować defekty zwykle występujące w wyhodowanych warstwach epitaksjalnych. Pomiary spektroskopowe wykonane w szerokim zakresie temperatur zaowocowały obserwacją zmiany energii emisji związanej z defektami w hBN skorelowaną

z przejściem fazowym antyferromagnetyk-paramagnetyk w użytym dwuwymiarowym magnesie. Pomiary przeprowadzone w zewnętrznym polu magnetycznym wykazały intrygujący efekt zanikania i zmiany energii emisji z centrum barwnego w hBN zachodzący w polu magnetycznym odpowiadającym tak zwanemu przejściu spin-flop w magnesie 2D. W rozdziale dyskutujemy możliwe przyczyny obserwowanych zjawisk, wskazując na odkształcenia mechaniczne lub zmiany w lokalnym polu elektrycznym i magnetycznym. Badania heterostruktur hBN/magnesy 2D są uzupełnione o wyniki spektroskopii optycznej przy pobudzaniu i detekcji z różnymi polaryzacjami światła. Przedstawiamy zależności kątowe widm zebranych w zewnętrznych polach magnetycznych dla sygnałów Ramanowskich pochodzących od badanego magnesu 2D i emisji związanej z defektami hBN, co dostarcza cennych informacji o symetrii stanów elektronowych w badanych strukturach.

Rozprawa jest podsumowana w rozdziale 8, wskazując możliwości dalszego rozwoju i zastosowań przedstawionych badań.

Opisane wyniki pokazują, że hBN jest przyszłościowym materiałem, który można skalować i stosować w heterostrukturach i urządzeniach o rozmiarach makro. Jednocześnie hBN zapewnia doskonałą platformę do badania podstawowych zjawisk fizycznych w skali nano. Przedstawione wyniki dotyczące centrów kolorów w hBN i ich interakcji z magnesami 2D otwierają szeroką ścieżkę do zastosowań związanych z technologiami kwantowymi i nanosensorami, podczas gdy heteroepitaksjalny wzrost $MoSe_2$ na hBN ma potencjał na zwiększenie skali wytwarzania heterostruktur van der Waalsa.

List of abbreviations used in the work

- 2D – two dimensional
- AFM – atomic force microscope
- $CrBr_3$ – chromium bromide
- $CrPS_4$ – chromium thiophosphate
- hBN – hexagonal boron nitride
- HWP – half waveplate
- MBE – molecular beam epitaxy
- $MoSe_2$ – molybdenum diselenide
- MOVPE – metalorganic vapour phase epitaxy
- PL – photoluminescence
- PSB – phonon sideband
- SEM – scanning electron microscope
- TMDC – transition metal dichalcogenides
- vdW – van der Waals
- ZPL – zero phonon line

[This page intentionally left blank]

Contribution of the author and collaborators to the conducted research

Raman spectroscopy	**MSc Katarzyna Ludwiczak**
Photoluminescence measurements	**MSc Katarzyna Ludwiczak**
Exfoliation and heterostructures assembly	**MSc Katarzyna Ludwiczak**
MOVPE growth	Dr Aleksandra Krystyna Dąbrowska
MBE growth	MSc Julia Kucharek Prof. Wojciech Pacuski
SEM imaging	Dr Mateusz Tokarczyk, **MSc Katarzyna Ludwiczak**
AFM imaging	MSc Rafał Bożek, Dr Jan Pawłowski
TEM imaging	Eng. Jakub Turczyński MSc Eng. Bogusława Kurowska
Large-area hBN delamination and transfer	**MSc Katarzyna Ludwiczak**
X-ray diffraction	Dr Mateusz Tokarczyk
Electrical measurements	**MSc Katarzyna Ludwiczak**, Dr hab. Marta Gryglas-Borysiewicz
Photolithography	**MSc Katarzyna Ludwiczak**, Dr Karol Nogajewski MSc Jakub Rogoża
CrX_3 crystal growth	Dr Joanna Wincukiewicz Prof. Jacek Jasiński

[This page intentionally left blank]

Acknowledgments

Completing this doctoral thesis would not be possible without the support of many people who have accompanied me at every stage of this scientific journey.

First of all, I would like to express my gratitude to my supervisors. Prof. dr hab. Andrzej Wysmołek welcomed me warmly into his research group when I was still pursuing my bachelor's studies. Throughout all these years, he has shown great support and understanding, shaping me as a scientist and a person. Before the PhD, dr hab. Johannes Binder was also the supervisor of my bachelor's and master's theses. Throughout this entire time, he was always available for discussions and taught me a lot while always taking my opinion into account. The deep knowledge and great intuition of my mentors allowed me to successfully realize ambitious projects from the early steps of my scientific career.

I have had the great pleasure of working alongside my colleagues from the Layered Materials Laboratory. I am thankful to MSc Jakub Rogoża, especially for our scientific and non-scientific discussions that helped me push through the up and downs of pursuing the PhD studies. I thank my younger colleagues, MSc Piotr Tatarczak and MSc Jakub Iwański, who created a collaborative atmosphere promoting the realization of various projects. I am very grateful to dr Aleksandra Dąbrowska, who always willingly provided me with new samples and impressed me with her time management skills. I also thank dr Mateusz Tokarczyk for his invaluable contribution to the SEM and XRD characterization of the samples.

My deep gratitude goes to our collaborators from other research groups at the University of Warsaw. I am especially thankful to MSc Julia Kucharek and prof. dr. hab Wojciech Pacuski for our joint work on combined epitaxial growth. I thank MSc Natalia Zawadzka and dr hab. Maciej Molas for explaining and letting me use the high-magnetic field experimental setup. I would like to express my gratitude to dr hab. Marta Gryglas-Borysiewicz for the help with electrical measurements. I would like to thank dr Joanna Wincukiewicz and prof. Jacek Jasiński for providing 2D magnet crystals. I am grateful to other colleagues, students, and collaborators whom I met during my studies.

I would also like to thank dr Karol Nogajewski and MSc Natasza Gajda for providing training and flawless maintenance of the *Nanotech* laboratories. My gratitude also goes to our collaborators from the Polish Academy of Sciences, especially engr. Jakub Turczyński and MSc engr. Bogusława Kurowska.

I thank the administrative and technical staff of our Faculty for providing excellent con-

ditions for work and grant realization. I am especially grateful to MSc Olga Babicka, BSc Ewelina Król, Marcin Król, and MSc Małgorzata Melon.

Last but not least I would like to express my gratitude to my family. My parents, Anna and Witold, who always supported me in realizing my dreams and wanted the whole world of opportunities to be open to me. I thank my fiancé Michał for increasing my confidence in myself and my skills, pushing me to achieve more, and always being there for me.

This research was funded in whole or in part by the National Science Centre, Poland grants: 2021/41/N/ST3/03579, 2019/33/B/ST5/02766.

Contents

[This page intentionally left blank]

1

Motivation

Quantum technologies have become one of the most intensively developing fields, promising significant improvements over their classical counterparts. Quantum communication may offer more security, while quantum computers could be used to solve specific mathematical problems or calculate protein conformations, indispensable in the search for new medicines [1]. New sensors would push the boundaries of knowledge giving access to atomic-scale resolution [2].

All of these thrilling applications need the development of appropriate building blocks,

ready to meet high expectations. Only one atomic layer thick, so-called two-dimensional materials are innately rooted in the quantum world, making them great platforms for advancing various technologies. To utilize 2D crystals we must establish ways to fabricate them on a large scale, as well as profoundly discover and understand their properties.

In this work, we focus on hexagonal boron nitride (hBN): a promising two-dimensional material, that has become an irreplaceable component of most structures consisting of other ultrathin crystals. We explore large-area epitaxial hBN in two ways: on a nano- and macroscale.

The first aim of the dissertation was to test the potential of using large-area hBN as a substrate for further, scalable fabrication of high-quality monolayers of other two-dimensional materials, namely molybdenum diselenide. We additionally explore the possibility of creating functional devices from the fabricated heterostructures by gating. The second aim of this work was to study the interactions between epitaxial hBN and nano-magnets. In particular, to explore the possibility of using hBN as a sensor of local strain or magnetic field. Unveiling the properties of hBN color centers on an atomic scale opens the path for applications like the development of operating on a nanoscale sensing foil – a material integrated into the structure, and providing information about the local environment.

We hope that our discoveries will contribute to the development of quantum technologies, both at the level of understanding the basic processes occurring in two dimensions, as well as advancing fabrication methods that can be used on a large scale.

2

Materials

2.1 Introduction

Rapid technical development constantly demands more efficient, miniaturized, and reliable solutions, propelling the search for novel materials. Studies of graphene opened the way for a whole new branch of research focusing on ultrathin crystalline layers [3, 4]. In these materials, atoms strongly connected via covalent bonds form layers. These in turn are stacked on top of each other and connected only by relatively weak van der Waals interaction. Such

a structure allows for the study of physical phenomena of two-dimensional systems, which can vary greatly from their bulk counterparts. Intriguing optical, electrical, and mechanical properties make 2D crystals a viable solution for the development of novel devices, as well as create a playground for basic research. Moreover, various 2D materials can be stacked on one another to create so-called van der Waals heterostructures – carefully designed systems that derive their properties from selected materials. Up to this day, more than a thousand crystals are predicted to be stable in their 2D form [5]. In the next sections, we present the structure, properties, and production method of 2D materials that are of interest to this work.

2.2 Boron nitride

Boron nitride belongs to the nitrides family – inorganic compounds consisting of nitrogen atoms. Among them, the group of semiconductor, III-V group materials was intensively studied due to their applications in various optical and electrical devices. The best-known representatives of these nitrides are: gallium nitride (GaN), aluminum nitride (AlN), and indium nitride (InN). They crystallize either in zinc blend or wurtzite form, with the latter being the most thermodynamically favorable and stable polytype. The mentioned nitrides possess a very similar lattice constant of 3.2 Å, which enables the creation of mixed crystals (ex. Al_xIn_xN, where $0 < x < 1$). Due to the bandgap varying from ∼0.5 eV for InN up to ∼6.3 eV for AlN, changing the amount of group III element in an alloy allows for a wide range of bandgap engineering [6].

Overcoming the obstacle of doping GaN for p-type allowed to construct an efficient blue light-emitting diode [7]. For this advancement the Nobel Prize was granted to Isamu Akasaki, Shuji Nakamura, and Hiroshi Amano. High energy, efficient light sources revolutionized the display market, pushing the development of ubiquitous TV and smartphone screens. The

discovery was also unprecedented in more professional applications, as it allowed to building lasers emitting light in the deep-UV range. These light sources found their purpose ex. in: material research, lithography, medicine, and surface decontamination [8]. Additionally, III-V group nitrides possess high electron mobility and saturation velocity, making them perfect materials for electronic applications [9]. For instance, in recent years GaN-based ultrafast chargers proved to be commercially available, more efficient alternatives than widely used silicon-based chargers. It is no wonder that finally scientists turned their attention to a much less studied III-V nitride – boron nitride. The material occurs in multiple forms:

- Amorphous: Atoms do not form long-range arrangement, as the material consists of multiple grains with sp^2 or sp^3 bonding type. Amorphous BN is usually formed as an intermediate layer during the growth process of other, crystalline BN phases. [10, 11]

- Cubic: crystallizes in zinc-blende structure with lattice constants: a=2.55 Å, c=4.17 Å (fig. 2.1a) [12, 13]. The material is extremely hard, hence its wide use as an abrasive and a protective coating for cutting tools. Moreover, cubic BN manifests high thermal conductivity, wide (6.1-6.4 eV) bandgap, and (unlike diamond) is insoluble in ferrous metals at high temperatures. Due to its high transmittance over a wide spectral range, it can be used in X-ray membranes [14].

- Wurtzite: metastable boron nitride polytype with lattice constants a=2.55 Å, c= 4.21 Å (fig. 2.1b) [15]. It can be produced from the hexagonal boron nitride in a high-pressure shock compression process. Obtaining bulk crystals of wurtzite BN constitutes a challenge due to technical difficulties in stabilizing it at atmospheric pressure. Some solutions like introducing three-dimensional networks of defects were proposed to overcome this problem [16], however, more research is needed to develop a reliable synthesis scheme.

- Hexagonal: crystallizes in a honey-comb structure, similar to graphite (fig. 2.1c), and is the most stable polymorph of boron nitride. As a material crucial to this work, it is described in more detail in the next sections.

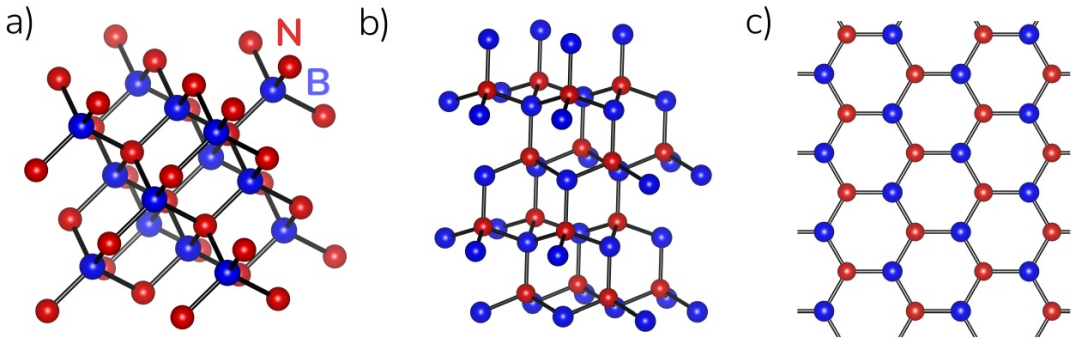

Figure 2.1: Schematic illustration of different crystal structures of boron nitride: a) cubic, b) wurtzite, c) hexagonal. The illustration was made using VESTA software [17].

2.2.1 Boron nitride with sp^2 hybridisation

Orbital hybridization describes the idea of mixing atomic orbitals to correctly predict the shape and structure of molecules and crystals. For instance, in the case of a simple methane molecule (CH_4), we observe a tetrahedral geometry with C-H bonds arranged around a central carbon atom. Bonds are of the same length and strength, with angles equal to 109.5 deg between them [18]. One 2s and three 2p orbitals of carbon form covalent bonds with four hydrogen atoms to create an energetically favorable structure. Such hybridization (called sp^3) is present in classical nitrides (like previously mentioned GaN, InN, and AlN) and is intrinsically three-dimensional.

On the contrary, in the case of sp^2 hybridization, one s orbital is mixed with two p orbitals to form a flat, two-dimensional structure, with 120° bond angles. Boron nitride with sp^2 hybridization combines the advantages of typical III-V semiconductors like a large bandgap

and high thermal and chemical stability, with possibilities deriving from its two-dimensional nature [19].

2.2.2 Structure

Boron nitride with sp^2 hybridization is a representative of van der Waals materials: boron and nitrogen atoms are arranged alternately in a flat, honey-comb structure with interatomic distances of 1.45 Å. Atomic layers can be stacked differently in respect to each other forming various polytypes. The most stable one is hexagonal boron nitride (hBN), with point group symmetry P63/mmc and lattice constants of a=2.503 Å and c=6.661 Å. Layers are arranged in AA' pattern, with nitrogen atoms from one layer lying directly over boron atoms from another layer and so on (fig. 2.2a).

Another sp^2 hybridized polytype is rhombohedral boron nitride (rBN), where three adjacent layers are translated and set in ABC configuration (figure 2.2b). The material possesses R3m symmetry with lattice constants: a=2.504 Å and c=10.008 Å [20, 21].

The next representative of sp^2 bonded boron nitride is its turbostratic form (tBN). In this least ordered polytype, layers are translated and twisted randomly with respect to each other (figure 2.2 c) [19, 22]. It is worth noting that there are even more BN polytypes following different stacking orders (like AB, CA etc.) [23]. It is worth mentioning that all three mentioned polytypes: hBN, rBN, and tBN, are often called hexagonal boron nitride, especially when talking about a single-layer material, where there is no stacking of different layers. In this work we also adopt this naming approach, even though our epitaxial layers are usually a mixture of different polytypes [24].

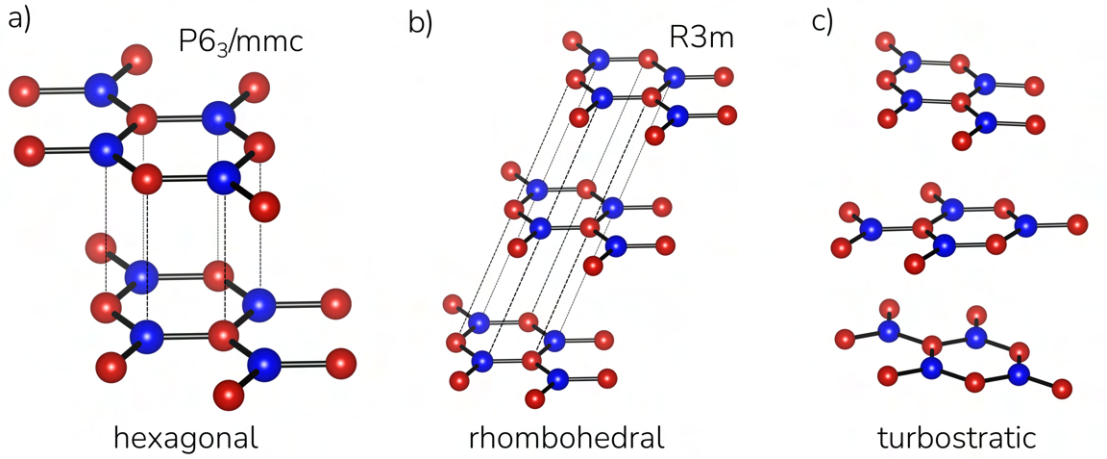

Figure 2.2: Schematic illustration of different crystal structures of sp^2 bonded boron nitride: a) hexagonal, b) rhombohedral, c) turbostratic. The illustration was made using VESTA software [17].

2.2.3 Fabrication

Boron nitride with sp^2 hybridization does not occur naturally and has been fabricated synthetically since the beginning of the XX century. To obtain the material, we distinguish two approaches: bulk crystals and deposition techniques.

Bulk crystal growth As sp^2 hybridized BN is a promising material, a lot of effort came into obtaining high purity and structural quality crystals. After decades of growth optimization, crystals made by Takashi Taniguchi and Kenji Watanabe are believed to possess the best structural, physical, and chemical properties [25, 26].

For this approach, the temperature gradient method utilizing high pressure (HP) high temperature (HT) apparatus is used. Hot-pressed hBN discs and powder hBN are initially heated at temperatures over 2000 °C in a nitrogen flow to remove the oxygen. Then, the material is placed in a barium boron nitride ($Ba_3B_2N_4$) solvent and encapsulated in a molybdenum chamber. The sample is then compressed at pressures varying between 4-5 GPa at temperatures over 1500 °C for 20-80 h (varying on the process). After the growth, the molyb-

denum capsule is dissolved in aqua regia [26, 27]. The obtained crystals are almost transparent and just around 1x1x0.1 mm small. Performed secondary-ion mass spectrometry (SIMS) characterization indicates that the number of oxygen and carbon impurities is as low as 10^{18} atoms/cm^3. Cathodoluminescence studies show, that the material possesses a large bandgap of $\sim$6 eV and additionally can emit light from the defects at various energies [28].

hBN crystals grown by Taniguchi and Watanabe were proven essential to produce high-quality 2-dimensional heterostructures. Another method worth noting for fabricating bulk hBN crystals is metallic flux growth technology using high-temperature Ni-Cr flux to grow high-quality crystals [29, 30].

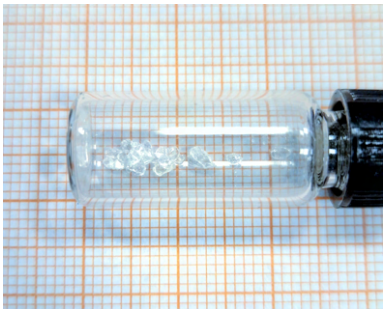

Figure 2.3: A photo of commercially available hBN crystals (*hq graphene*).

As a material indispensable for layered crystals studies, hBN has also become commercially available and is offered by various manufacturers like *hq graphene* (figure 2.3) or *Saint-Gobain*. Its quality, especially the number of impurities is slightly worse than for the hBN offered by Taniguchi and Watanabe, but still sufficient for most of the research [31, 32].

Deposition methods For any material to be used in real-world devices, it is crucial to produce it in a reproducible manner on a large scale. Despite the high structural quality of bulk crystals grown in the HPHT method, their small lateral size prevents them from being used in any industrial applications. Bottom-up approaches, where thin materials are grown on large-area substrates, provide a solution to the scalability problem, however simultaneously open up a whole new package of challenges.

One of the most established bottom-up approaches is Chemical Vapor Deposition (CVD) dating back to the XIX century. In principle, this method requires a reaction chamber, where

volatile precursors can react on or in the vicinity of a heated substrate to form the given solid material [33]. The term CVD describes a whole family of fabrication methods with the same working principle, differing by various parameters like operating pressure, temperature, type of reagents, etc. Figure 2.4 shows a CVD reactor typically used in a laboratory environment. It uses a quartz tube as a reaction chamber and is a hot-wall system, meaning that the substrate is heated externally by the radiation from the heated tube walls. Pipes supply the tube with a controllable, continuous flow of carrier gases and source material. So far, large-area

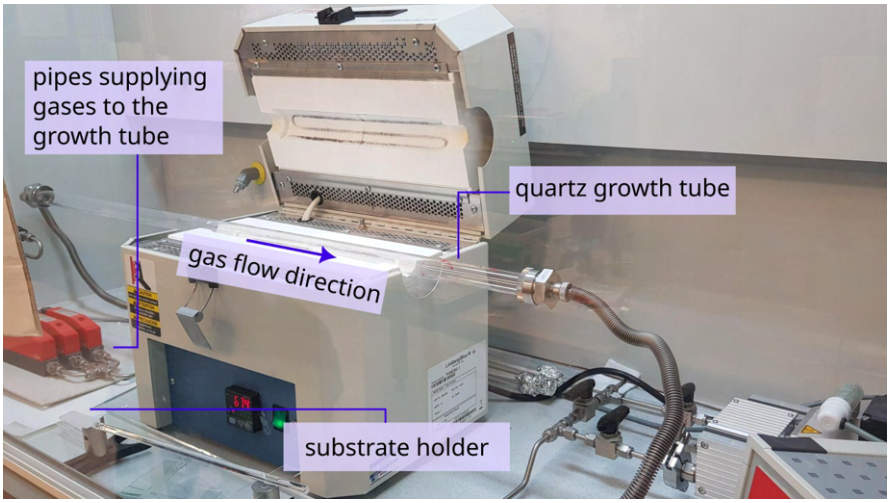

Figure 2.4: A photo of *Thermo Scientific* CVD reactor used at ICFO institute in Spain. The setup consists of a quartz tube placed in a furnace that can heat it up to 1050°C. The substrate is put on a spoon-like holder and placed in the middle of the growth tube before the process. During the growth, various gases are supplied into the tube continuously in specific proportions for a given material. Some of the gases, like argon or hydrogen serve as carrier gases while others, like methane, provide the material for the growth.

hBN CVD growth was demonstrated on metallic foils like copper and platinum [34, 35], or without using a metal catalyst [36]. Some groups reported the formation of a single crystal on the whole wafer [37–39]. However, it is challenging to achieve high-quality thicker than mono- or few-layer samples [40]. Even though CVD-grown hBN became commercially available, recent studies show that the provided samples do not meet the properties given in the

manufacturer's specifications [41].

Another approach to grow hBN includes utilizing molecular beam epitaxy (MBE). This technique (described in more detail in chapter 3) allows to precisely grow subsequent layers of the material in an ultra-pure environment. MBE growth performed on a nickel foil allowed to obtain highly crystalline atomically thin hBN star-like islands [42–44]. The biggest drawbacks of using MBE to grow large-area layers are its high cost and slow rate of material growth.

In comparison, Metalorganic Vapor Phase Epitaxy (MOVPE) allows to grow relatively high-quality layers of hBN cheaper and faster. In this work we explore the quality of the hBN layers produced by our group with this method. We study the utility of obtained samples for two main applications: as a large-area substrate for further growth of other 2D materials, and as a host for color centers.

2.2.4 Properties

hBN is characterized by a high chemical and thermal stability making it a very resistant material toward any environmental factors [19, 45, 46]. Interestingly, the material possesses a negative thermal expansion coefficient in-plane (-2.83$\times 10^{-6}$ K^{-1} at room temperature), which significantly influences the morphology of the samples obtained during epitaxial growth at high temperatures [47].

hBN possesses a wide bandgap determined to be $\sim$5.95 eV [25]. There was a long discussion about the nature of the energy gap and band structure, with some sources claiming the occurrence of a direct bandgap [25] or that the bandgap changes from indirect to direct in the monolayer limit [48]. Eventually, the consensus is that the bandgap has an indirect nature; however, due to the high photoluminescence effectiveness, the material can, under some circumstances, act as a direct bandgap semiconductor [28].

Symmetry analysis classifies the optical phonons of hBN in the center of the Brillouin zone as the irreducible representations of the $P6_3/mmc$ group as follows: $E_{1u}+A_{2u}+2E_{2g}+2B_{1g}$. Out-of-plane A_{2u} and in-plane E_{1u} modes are infrared active, in-plane E_{2g} modes are Raman active, and B_{1g} modes are optically inactive [49, 50]. Experimental studies showed infrared active modes at 783 cm^{-1} and 1510 cm^{-1} for excitation with light polarized parallel, and 767 cm^{-1} and 1367 cm^{-1} for light polarization perpendicular to the hBN c-axis. Raman signal is detected at 51.8 cm^{-1} and 1366.2 cm^{-1} [49]. Position and width of the observed Raman peak are useful indicators of the material's quality: strain and disorder caused by the presence of defects, which will also be used in this work.

Color centers

Real-life crystals are not perfect: sometimes they can lack an atom in some places, or one atom can be replaced by another. Doping – a deliberate replacement of some of the atoms of one element with another allows for improving and controlling material conductivity. Efficient doping has become crucial for the development of modern electronics.

Defects that appear only around a single lattice point in the crystal structure are called point defects and can be useful in developing new devices. The appearance of defects result in the formation of additional energy levels within the bandgap of a given material, which effectively acts like an artificial atom. Such centers can emit light or be sensitive to the magnetic field. One of the best-known and described defects are nitrogen vacancies in diamond, which are used for magnetometry [51, 52]. However, for some applications it is beneficial to place color centers very close to the studied samples. Hence, intrinsically two dimensional materials started to be intensively studied in the search of well-performing defects.

hBN with its large bandgap hosts a wide range of impurities, vacancies, substitutions, interstitial, or self-interstitial defects [53]. Various symmetries of color centers result in light

emission with wavelengths ranging from UV [54], through visible [55], to infrared [56].

Ultrathin hBN layers exfoliated from bulk are usually of very high quality, so light emission from the defects has to be activated artificially. It can be done, for example, by annealing in a high temperature [55, 57], slight destruction of the layers by neutron or ion beam irradiation [56, 58, 59], or by applying strain [60].

Second-order correlation function measurements allow to qualify some of the emitters found in hBN as single photon sources [61, 62]. Emitted photons manifest antibunching behavior, making them purely quantum optical objects. Single photon sources are essential building blocks for quantum information applications.

Another intriguing class of emitters found in hBN includes optically active spin defects. So far, negative boron vacancies (V_B^-) are the best-understood system manifesting an electronic spin-triplet with a ground state zero-field splitting (ZFS) [2]. The photoluminescence signal of V_B^- is centered around 850 nm and spectrally wide. Recent studies show, that other types of defects (ex. carbon-related) can be also sensitive to magnetic field [63–65].

Light emission from the color centers in hBN can be altered by a number of external factors. Firstly, some emitters are sensitive to the electric field, and manifest Stark effect [66–68]. Other emitters can be switched on and off on demand by applying the voltage [69–71]. Lastly, color centers can be sensitive to local mechanical stress in the material [72–74].

2.2.5 Applications

Due to its structure and easy detachment of the layers, hBN has been used in the cosmetics industry and as a lubricant [75]. It is also an excellent absorbent of oils and organic compounds, making it a prominent platform for purification technologies [76]. Due to its wide bandgap, hBN may find applications as a deep UV light source [77]. However, the real boom in the popularity of the material came with the development of other 2D materials. hBN became

an omnipresent component of practically all ultrathin heterostructures. It serves as a protective layer against environmental conditions, as well as a non-conductive spacer. Additionally, a flat interface of hBN, ideally without any dangling bonds, provides a good dielectric environment and no charge traps for neighboring crystals.

Recent studies considering light emitting defects in hBN show their potential in the field of quantum technologies. Single photon emitters could prove useful in quantum information processing [62]. hBN can be also used for the development of ultrasensitive, atomic-scale sensors of pressure, strain, or magnetic field [2].

2.3 Transition metal dichalcogenides

Intensive studies of graphene at the beginning of the XXI century have resulted in numerous proposals of possible applications of this material in the fields of energy storage, solar cells, and biomedical [78, 79]. However, due to the zero-energy gap, the construction of logic electronic devices with graphene is limited [80]. Hence, yet another group of 2D materials: transition metal dichalcogenides (TMDC) has become a hot topic in the materials study [81, 82]. The whole family of TMDCs shares the same general formula MX_2, where M denotes a transition metal atom ($M = Mo, Ta, W, Ti...$), and S – chalcogen atoms ($S = S, Se, Te$). One-layer TMDC is built out of three atomic planes, with a transition metal element plane sandwiched between two chalcogenide planes: X-M-X (Fig. 2.5).

TMDCs manifest various exciting electronic, optical, and catalytic characteristics, depending strongly on the number of atomic layers of a given material. The most prominent example of such behavior is a transition from an indirect to a direct bandgap in a single-layer limit, firstly observed and described in molybdenum disulfide [83–85]. Additionally, TMDCs offer a wide range of band engineering realized by doping, straining, or creating

heterostructures and alloys [86–89]. Due to the reduced dielectric screening, in 2D form, TMDCs possess strongly bound excitons with binding energies even an order of magnitude greater than in traditionally used 3D semiconductors [90, 91]. Some TMDCs manifest spin and valley degrees of freedom, opening possibilities of utilizing them in novel spintronic and valleytronic devices [92–95]. Described materials make a great platform for studying basic physical phenomena like charge density waves [96, 97], or topological effects [98, 99].

Many proof-of-principle devices like field-effect transistors [90], photodetectors [100] and quantum emitters [101, 102] have been realized using TMDCs layers. However, the highest quality (best structural properties, highest mobility, etc.) samples are still obtained via mechanical exfoliation. There is an ongoing effort toward large-area production of ultrathin crystal layers using methods like MBE [103], MOVPE [104], CVD [105] or ALD [106].

The next section presents a representative of the TMDC family, molybdenum diselenide ($MoSe_2$), which is one of the main subjects of this work.

2.3.1 Molybdenum diselenide

$MoSe_2$, like other TMDCs, follows the general formula MX_2 and its single atomic layer is built of three atomic planes: selenium, molybdenum, and selenium. Mo and Se atoms are covalently bound, while subsequent atomic layers are weakly bound via van der Waals forces. The material may exist as different polymorphs: namely 2H and 1T phases (Fig. 2.5). However, only the 2H phase is thermodynamically stable.

In the bulk form, $MoSe_2$ manifests an indirect bandgap, which undergoes a transition to a direct bandgap (1.55 eV) in the monolayer limit [107]. The D_{6h} point group predicts four Raman active modes: three in-plane E_{1g}, E^1_{2g}, and E^2_{2g}, and one out-of-plane mode A_{1g}. In the backscattering geometry we usually see the E_{2g} mode at $\sim$286 cm^1 and A_{1g} mode at $\sim$242 cm^1 [108]. The energy and intensity of the modes changes with the number of layers

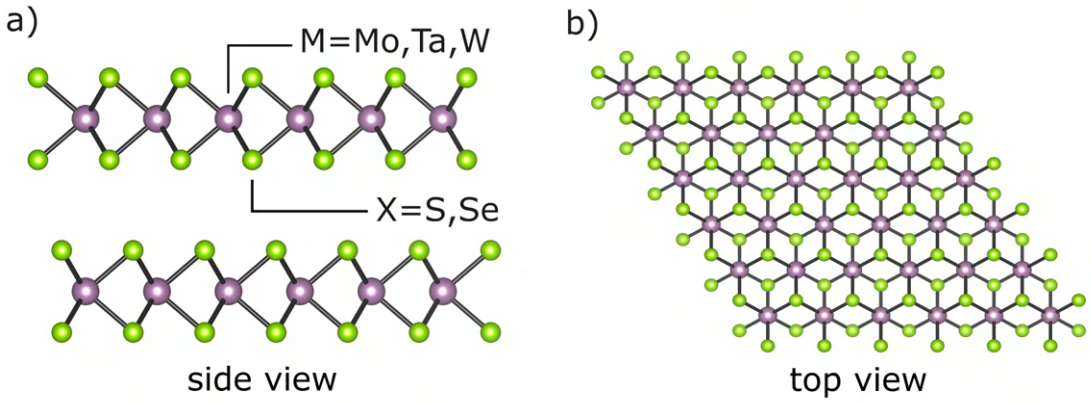

Figure 2.5: Schematic illustration of a crystal structure of molybdenum diselenide, a representative of TMDC. The illustration was made using VESTA software [17].

of the material, making Raman spectroscopy a great tool for determining the thickness of the $MoSe_2$ layer. Similarly, photoluminescence can also provide information about the material thickness. At room temperature, the PL signal from a monolayer forms a single maximum and is ∼20 times more intense than the one obtained for a bilayer (which branches into two wide maxima) [108]. For high-quality $MoSe_2$ samples, low-temperature PL spectra unveil narrow and well-resolved excitonic peaks [109]. Properties of $MoSe_2$ make it a promising material for applications like photoelectrochemical and solar cells, electrocatalysts, or biosensors [110].

2.4 Ultrathin magnets

2.4.1 Theoretical description

Magnetism in solids

Magnetic materials have been known to humans for ages. First mentions of magnetite: naturally occurring mineral and iron ore, can be found as far back as 4th century BC in ancient China and Greece. For centuries people were using magnetic materials to produce compasses

invaluable for navigation. A mathematical description of the connection between electricity and magnetism was developed in the XIX century with the works of Hans Christian Ørsted, Michael Faraday, and James Clerk Maxwell.

Magnetism in a material is associated with an ordered arrangement of magnetic moments on a large, macroscopic scale, as well as with a spontaneous breaking of the time-reversal symmetry.

The magnetic moment is defined as a vector that describes the magnitude of torque that an object experiences in a magnetic field as follows:

$$\tau = \mu \times B, \tag{2.1}$$

where: τ – torque, μ – magnetic moment, B – uniform magnetic field. It can be attributed to macroscopic objects like planets and stars, loops of electric current, and microscopic scale objects like elementary particles and molecules.

Some materials manifest a spontaneous arrangement of their intrinsic magnetic moments (ferromagnets, ferrimagnets, antiferromagnets). Other materials (or all materials above their proper critical temperature) do not possess a spontaneous magnetization and react differently to the applied magnetic field and thus can be categorized by the magnetic susceptibility (usually denoted as χ): a quantity that determines how much the material will be magnetized when put into the magnetic field. For $\chi > 0$ we distinguish paramagnets and for $\chi < 0$ we distinguish diamagnets [111].

The formulation of Maxwell's equations, as well as Boltzmann's statistical thermodynamics, allowed the development of the first microscopic models of magnetism in systems of atoms and molecules. In these approximations, magnetic moments are permanently assigned to particles, acting like micro-magnets, which can align with the applied magnetic field. At

absolute zero temperature, all of the elementary magnets would be aligned parallel to the field, while with increasing temperature, thermal fluctuations would destroy the order following the formula known also as Curie's law:

$$\chi = \frac{C}{T}, \tag{2.2}$$

where χ stands for magnetic susceptibility, T is the temperature and C is the Curie constant dependent on the number density and magnetic moments of the particles. Curie's law describes systems only in a classical limit: high temperatures and relatively low magnetic field. It is also applicable just to paramagnets: materials weakly attracted to a magnetic field that can induce an internal magnetic field in the same direction.

Parallelly, Langevin formulated a classical description of diamagnetism: a situation where a magnetic field induced in a material has the opposite direction to the external magnetic field, the material is repelled from the magnetic field. For diamagnetics (like copper, water, or bismuth), magnetic susceptibility is smaller than 0 and described by the following formula:

$$\chi = -\frac{\mu_0 N Z e^2}{6m} < r^2 >, \tag{2.3}$$

where μ_0 is vacuum permeability, r – mean square distance of the electrons from the nucleus, Z – number of charged particles, electrons, N – number of atoms per unit volume, m – electron mass, and e – electron charge [111].

However, with the works of Hendrika van Leeuwen, it became clear that magnetic phenomena can not be explained classically. Hence, a quantum mechanical approach is necessary to describe magnetism in solids, especially in 2D materials.

The Quantum mechanical electron state in an atom can be fully represented by a set of quantum numbers:

- principal $n \in 1, 2, 3...$ – denoting the electron shell (energy level) of a particle,
- azimuthal $l \in 0, 1, 2, ..., n-1$ – describing orbital angular momentum and hence the shape of the orbital,
- magnetic $m_l \in -l, ...0, ...l$ – characterizing the direction of an orbital in three-dimensional space,
- spin $m_s \in -1/2, +1/2$ – describing the intrinsic angular momentum (or spin) of an electron.

By using quantum numbers and introducing a so-called molecular field responsible for spontaneous magnetic ordering, Pierre Weiss formulated a formula describing ferromagnets in their paramagnetic regime, known also as Curie-Weiss law:

$$\chi = \frac{C}{T - T_C}, \text{ where } C = \frac{\mu_B g}{3k_B} M_0(J+1), \tag{2.4}$$

with M_0 – magnetic moment at $T = 0$, μ_B – Bohr magneton, g – Lande factor, k_B – Boltzmann constant, and J – angular momentum quantum number. Below the critical temperature T_C (known also as Curie temperature), the system is spontaneously magnetized [111].

To describe magnetic phenomena in crystals, one must take into consideration the interaction between neighboring atoms and electrons. Some spin arrangements are favored in specific systems and can spread in the whole object. At hypothetical zero temperature long-range spin ordering can occur in any-dimensional system. With the increase of the temperature, thermal fluctuations start to overcome the spin ordering on large scales and destroy it above the phase transition temperature T_C. Whether this critical temperature is finite or equals zero, is determined by the effectiveness of thermal fluctuations in a given system, specified by its various parameters such as the dimensionality.

The most commonly used model of magnetic effects in crystals is the Heisenberg model, first formulated in 1928. It assumes a periodic lattice with sites (denoted with i, j) occupied by a spin that can be described as an operator **S**. Spin is treated as a quantum mechanical observable. The energy of such a system is given by a Heisenberg Hamiltonian H:

$$H = -\frac{1}{2}\sum_{<ij>}(J\mathbf{S}_i \cdot \mathbf{S}_j + \Lambda S_i^z S_j^z) - \sum_i A(S_i^z)^2, \tag{2.5}$$

where J is the exchange coupling constant, decreasing quickly with the distance between lattice sites i and j. For $J > 0$ spins are arranged parallelly (ferromagnetic behaviour) and for $J < 0$ spins are arranged in an anti-parallel manner (anti-ferromagnetic behaviour). J can be calculated theoretically from first-principles calculations or found experimentally by fitting the inelastic neutron scattering data to the Heisenberg Hamiltonian. Λ describes exchange (inter-site) and A describes on-site magnetic anisotropies, crucial for the occurrence of a long-range magnetic ordering in two dimensions [112, 113].

Why 2D magnets remained elusive for so long?

In 1966, the Mermin-Wagner theorem was published, analyzing the isotropic (spins can point in any direction) Heisenberg model [114]. The theorem states, that continuous symmetries can not be spontaneously broken in a two or less-dimensional system exhibiting short-range interactions, at finite temperatures.

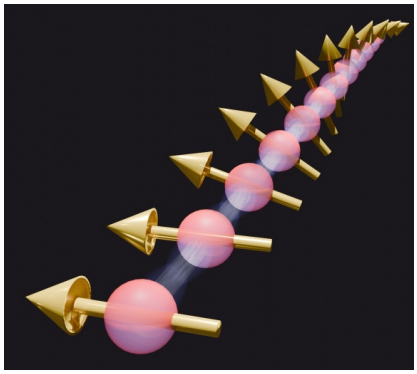

Figure 2.6: Schematic illustration of a spin wave in a 1-dimensional array of interacting spins.

In the case of a one-dimensional system, one can consider a chain of interacting spins. At $T = 0$, they are perfectly ordered, however, at a higher temperature,

one spin can be thrown out of the alignment and start

rotating. Due to the interactions, other spins will also start rotating, forming a so-called spin wave (fig. 2.6). Such an elementary excitation of the spin-lattice is also called a magnon in the quasiparticle approach. For a considered chain of spins in the infinite length limit, the total energy of the lowest excitation mode goes to zero. Simultaneously, excitations increase the system entropy and, therefore, are favored. In other words, a long-range magnetic ordering in a one-dimensional case is possible only for $T = 0$.

The situation is different in the case of two-dimensional systems. To describe spontaneous magnetization in 2D materials, it is important to consider so-called spin dimensionality (n) – the number of spin components (fig 2.7).

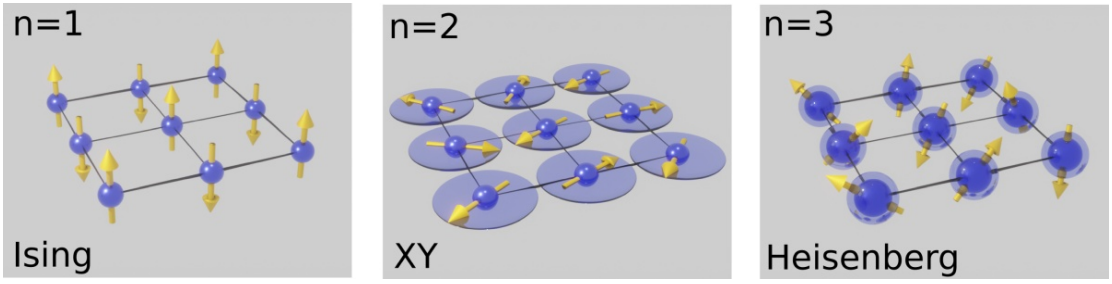

Figure 2.7: Schematic illustration of a concept of spin dimensionality (illustration based on [112]). n denotes the number of spin components for systems described by Ising, XY, and isotropic Heisenberg models.

For $n = 1$ spins can only point in two possible orientations (”up” and ”down”). Such a system of one-component localized spins is called the Ising model, and its solution shows a magnetic order phase transition for $T_C > 0$ [115].

For $n = 2$ spin direction is restricted to a plane, described by the XY model. Such a system can undergo Berezinskii–Kosterlitz–Thouless transition at finite temperature to a quasi-long-range order phase. This is an example of *infinite order* phase transition that is continuous but does not break any symmetry [116].

For $n = 3$ spins possess 3 components – it is the case of the previously described isotropic Heisenberg model. Mermin-Wagner theorem prevents any long-range magnetic ordering in such a system.

Such theoretical predictions, as well as experimental difficulties, impeded the 2D magnets research. However, with the discoveries in the van der Waals materials family, in 2016, 2D magnets were finally obtained experimentally [117, 118].

In the real world, 2D material flakes have typical sizes in at most millimeter range. It was recently shown [119] that the short-range interactions in such a small, laboratory setup are, indeed, strong enough to stabilize magnetic ordering at finite temperatures without the magnetic anisotropy. Moreover, the calculations show that the so-called crossover temperature (maximum temperature where short-range interactions may grant magnetic ordering in the sample) is over 4 K for a system as large as the entire known universe (order of 10^{25} m).

Exchange interaction mechanisms in 2D magnets

Another aspect of exploring magnetism in 2D is understanding the type of exchange interaction in specific materials. The symmetry and specific elements building the crystal constitute different spin localizations and interactions.

The magnetic ground state of an atom can be determined using Hund's rules, which describe spin-spin coupling, orbital-orbital, and spin-orbit coupling. The application of these rules to various atoms specifies the order of filling of the electron shells and subshells. Then, spins can interact via the following exchange types [113]:

- **Direct exchange** occurs for systems where electronic wavefunctions overlap and therefore the interaction is short-ranged and relatively weak [120]. It requires hopping between nearest neighbors' orbitals. It is usually found in transition metals with localized

d-orbitals [121]. Despite being weak, direct exchange was found as the main mechanism for magnetic coupling for example in 1T-TaN_2 2D magnet [122]. It can also accompany other types of interactions and be responsible for one electron-hopping path like in the case of monolayer $MnSeS_3$ [123, 124].

- **Superexchange** interaction occurs between non-neighboring magnetic ions but needs to be mediated by the neighboring non-magnetic ions. This type of interaction between p and d orbitals is very common and is the predominant mechanism responsible either for ferromagnetic or antiferromagnetic ordering in various 2D magnets like the family of MX'enes [125, 126], chromium trihalides [127–129] and other layered materials like $Cr_2Ge_2Te_6$ [130].

  Sometimes, the interaction is mediated not by one, but more non-magnetic ions. It is then called **super-superexchange** interaction and was found in CrI_3 [118, 131]

- **Double exchange** occurs when two ions are in different oxidation states. The interaction works similarly to the superexchange: an electron can hop from one magnetic ion to the other by a mediating non-magnetic ion, however in the double exchange case one magnetic ion has to have an extra electron compared to the other [132]. In the field of 2D magnets, double exchange was found as the main ordering mechanism for Cr_3X_4 (where X=S, Se, Te) [133].

- **RKKY** (Ruderman–Kittel–Kasuya–Yosida interaction) is a type of exchange mechanism that couples different nuclear magnetic moments or strongly localized spins of electrons occupying inner d or f shells via the conduction electrons [134–136]. RKKY interaction is most commonly found in 3D rare-earth metals [137] but can be also used to describe magnetic interactions in two-dimensional $MnSiTe_3$ [138].

- **Itinerant magnetism** occurs for metallic materials, where unpaired delocalized electrons can transfer magnetic interaction. In such systems, electrons can occupy narrow bands – different for electrons with spin-up and spin-down. We can define an effective exchange energy per electron pair, that describes the energy gained when switching from anti-parallel to parallel spins. In order to gain such energy, electrons need to move from one eg. spin-up subband to the spin-down subband. Such transfer however increases also the kinetic energy. Thus, the interplay between the exchange energy and kinetic energy (given by a Stoner criterium) in the ground state of the system at a given temperature determines whether the material is para- or ferromagnetic [139]. In 2D materials itinerant magnetism is responsible for high, (around 300 K) Curie temperature in VX_2 (X=S, Se, Te) compounds [140, 141], as well as in Fe_3GeTe_2 and $NiTa_4Se_8$ crystals [142, 143].

Figure 2.8 depicts schematically various types of exchange interactions found in 2D magnets, their division in terms of the localization of spins, and the metallic/non-metallic nature of the compounds.

2.4.2 Selected 2-dimensional magnets

Chromium trihalides

Among discovered 2D magnets, the family of chromium trihalides (with general formula CrX_3, where X=Cl, Br, I) provides a perfect platform for studying different spin arrangements as each of these materials exhibits different spin-dimensionality and magnetic ordering [144].

Heterostructures consisting of chromium trihalides allow exploration of various phenomena like exchange bias [138], magnon-assisted tunneling [145] or layer-resolved mag-

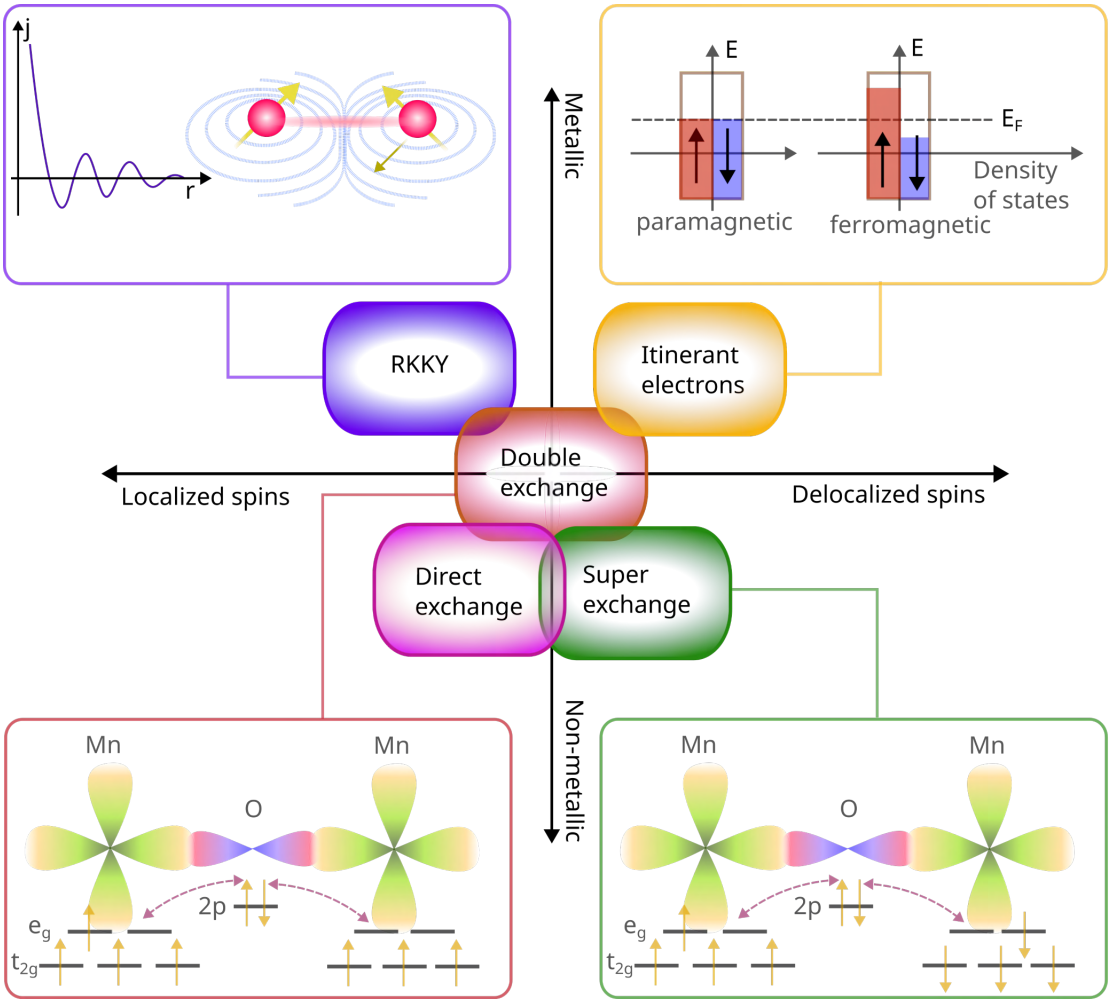

Figure 2.8: Diagram of various exchange interactions occurring in 2D magnets [113]. RKKY (violet frame): coupling constant j as a function of r distance from the magnetic ion nucleus. In this type of interaction, well-localized nuclear spins interact via conduction electrons. Non-localized itinerant electrons (yellow frame) dominate systems' magnetic interactions when parallelly ordered spins minimize the energy of the ground state, despite the gained kinetic energy. Double exchange (red frame) occurs between two magnetic ions with different numbers of electrons on the outer shell and is mediated by a non-magnetic ion. Superexchange (green frame) occurs between two magnetic ions with the same number of electrons on the outer shell and is mediated by a non-magnetic ion. The double and super exchange interaction scheme was shown using manganese and oxygen ions as examples.

netic proximity effect [146, 147]. When combined with transition metal dichalcogenides, chromium trihalides can influence the optical response of given materials [148, 149].

Chromium thiophosphate

Another 2D magnet used in this work is chromium thiophosphate ($CrPS_4$). The material manifests monoclinic symmetry with space group C2/m [150, 151]. Lattice constants are $a = 10.871$ Å, $b = 7.254$ Å, $c = 6.140$ Å, $\beta = 91.88$[150]. Layers of sulfur atoms are arranged in a puckered fashion, adopting hexagonal close packing along the a-axis, while chromium atoms form a square lattice. Each chromium atom is surrounded by six sulfur atoms, forming a subtly distorted octahedron. Additionally, three CrS_6 octahedra are connected by a singular phosphorus atom (figure 2.9). The material belongs to the van der Waals materials family and, hence can be exfoliated down to single atomic layers. $CrPS_4$ is a representative of ternary transition metal chalcogenides (TTMC): layered compounds consisting of three elements. In contrast to the intensively studied transition metal dichalcogenides, many of the TTMC exhibit magnetic ordering.

Bulk $CrPS_4$ crystals can be synthesized using the CVT method and have been synthesized this way since the 70s [152]. The theoretical analysis predicts vibrational symmetries of Γ = 17A + 19B, where all modes are both infrared and Raman active [153, 154]. Raman measurements are a powerful tool for determining the thickness of the material in a few-layer limit [150]. $CrPS_4$ is a semiconductor with a bandgap of around 1.4 eV [150, 155]. It was shown [155], that under high pressure (over 3 GPa), the material exhibits an insulator-metal phase transition.

$CrPS_4$ demonstrates antiferromagnetic behavior with a Neel temperature of 36 K [156] for bulk samples. Neel temperature decreases with the decreasing number of layers and was found to be 25 K for a single atomic layer [157]. The type of antiferromagnetic ordering was intensively discussed with some works opting for a c-type [156] and others for a-type [157, 158] antiferromagnetism. The current consensus leans towards a-type antiferromagnetism,

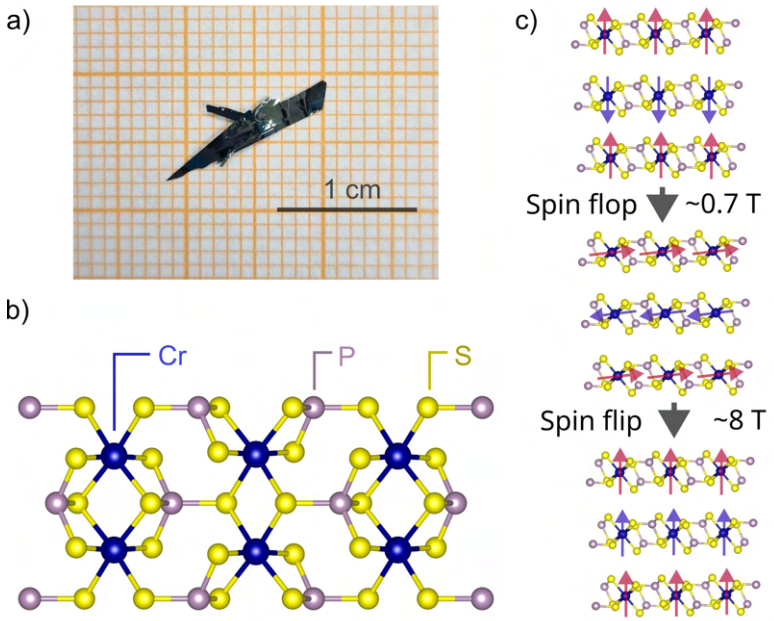

Figure 2.9: a) A photo of a bulk $CrPS_4$ crystal. b) Structure of $CrPS_4$ crystal (top view). The material crystallizes in a c/2m monoclinic structure. c) Side view of $CrPS_4$ crystal. Arrows schematically indicate spin arrangements between the layers. Antiferromagnetic ordering appears below the Neel temperature of around 36 K. The visualization was prepared using VESTA software [17].

meaning that spins within one layer are ordered ferromagnetically out of plane, while spins from different layers are facing in the opposite direction (fig. 2.9 c). In the few-layer limit, such a spin arrangement grants ferromagnetic behavior for odd and antiferromagnetic behavior for even number of atomic layers. At an external magnetic field (applied perpendicularly to the material plane) of around 0.7 T, $CrPS_4$ displays a so-called spin-flop transition, when it is energetically favorable to "flop" spins (or more accurately Neel vector) from out-of-plane to in-plane direction [156]. This behavior makes $CrPS_4$ an attractive candidate for spintronics devices. The spin-flop transition can be electrically detected and controlled, making a step toward read-out technologies for future memory devices [159, 160]. Further increase of the external magnetic field causes further canting of the flopped magnetic moments. At higher fields of $\sim$8 T, this state becomes saturated and the material undergoes yet another: spin flip

transition. Magnetic moments flip in the same out-of-plane direction, resulting in ferromagnetic behavior [161].

The possibility of changing the spin direction in the $CrPS_4$ crystal is also important for this work. Such tunability allows us to study the influence of different magnetic states applied locally to other 2D materials.

Chromium thiophosphate is a highly anisotropic system. X-ray diffraction and nanoresonator frequency measurements show that the material exhibits temperature-dependent anomalous behavior of the *b* lattice parameter [162, 163]. While heating, lattice parameters *a* and *c* manifest a typical, slightly positive tensile strain. However, chromium-chromium distances decrease along the *b* axis, pointing at the negative temperature expansion coefficient, with a well-pronounced feature near the phase transition temperature [163].

Unlike other 2D magnets, $CrPS_4$ does not require special storage or handling in an inert gas chamber. It is one of the most air-stable 2D magnets, that does not show signs of degradation over days in normal conditions even in its few-layer form [157]. That is also the reason why this material was extensively used to create heterostructures studied in this work.

3

Epitaxial techniques

The term epitaxy comes from Greek and literally means *epi*– "on top of, above" and *taxis*– "an ordered matter". In the epitaxial manufacturing process, a thin layer of a crystalline material is grown on top of a crystalline substrate, duplicating its crystal lattice. We distinguish two main types of epitaxy, depending on the used substrate:

- homoepitaxy: when the grown material is the same as the substrate
- heteroepitaxy: when the grown material is different than the one used as a substrate.

In the case of heteroepitaxy, it is important to carefully select the optimal substrate with a similar lattice constant as the grown material. A significant mismatch between lattice constants can lead to strain in the produced material, as well as non-epitaxial growth and the formation of islands (3-dimensional clusters of atoms) [164, 165].

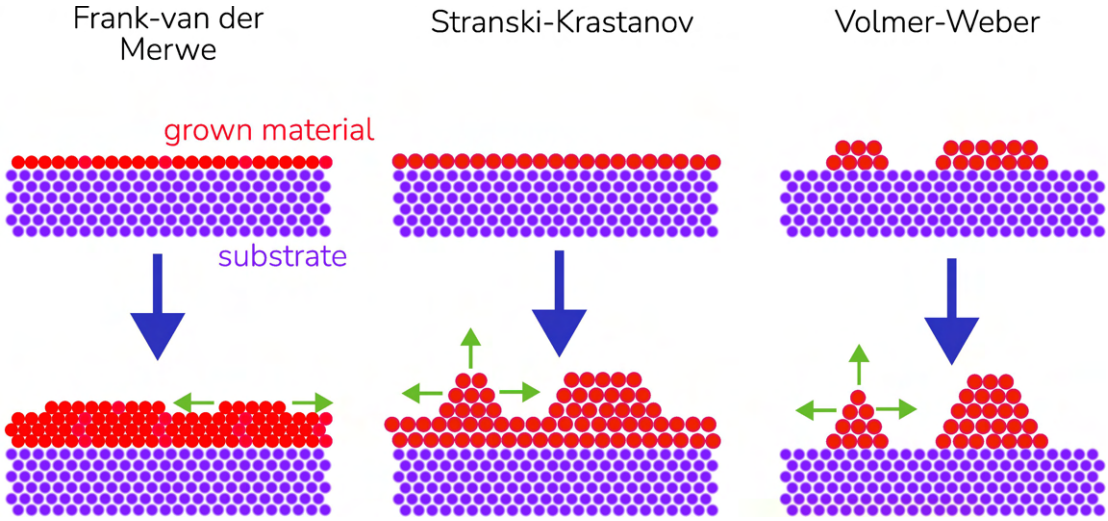

Figure 3.1: A schematic illustration of three epitaxial growth modes. Green arrows depict the direction of further growth of the material. Figure is based on [166]

Figure 3.1 depicts three primary epitaxy modes [166]:

- *Frank-van der Merwe* growth occurs when the lattice constant of the substrate is aligned with the grown material. The new crystal grows layer by layer, maintaining the crystallinity of the substrate.

- *Stranski-Krastanow* growth is present when vertical interaction energies between material-substrate atoms are significantly larger than material-material atoms and the lattice constant is not matched. The initial growth of a few layers of the material is followed by the formation of 3-dimensional islands.

- For *Volmer-Weber* growth vertical interaction energies between material-material atoms

are much greater than those for substrate-material atoms. Such a situation results in the formation of 3-dimensional islands from the very beginning of the growth process.

Epitaxial techniques allow the growth of high-quality, crystalline materials on large-area substrates. While epitaxial growth is not the main subject of this dissertation, epitaxial samples were intensively studied and post-processed. Therefore, for a better understanding, it is crucial to present the techniques, their capabilities, and limitations.

3.1 MOVPE

MOVPE: Metalorganic Vapor Phase Epitaxy is a method that uses chemical reactions between metal-organic compounds to grow a chosen, crystalline material. Precursors of a chosen element are transported in a flow of carrier gas (like nitrogen or hydrogen) into the reactor. hBN samples described in this work were grown in *AIXTRON CCS 3x2"* setup depicted in Fig. 3.2 by Dr. Aleksandra Krystyna Dabrowska.

Figure 3.2: A photo of MOVPE setup at the Faculty of Physics, University of Warsaw.

For the growth of hBN, ammonia (NH_3) is used as a nitrogen and triethylborane (TEB) as a boron precursor. Before the growth, ammonia, and hydrogen (used as a carrier gas in the process) flow through *Entegris* purifiers to minimize the concentration of any foreign elements. TEB is stored in a liquid form in a so-called metallic "bubbler", where it evaporates and is transported further by hydrogen gas. Precursors enter the *showerhead* reactor (Fig. 3.3), where at temperatures as high as 1400 $^{\circ}C$, the growth process takes place.

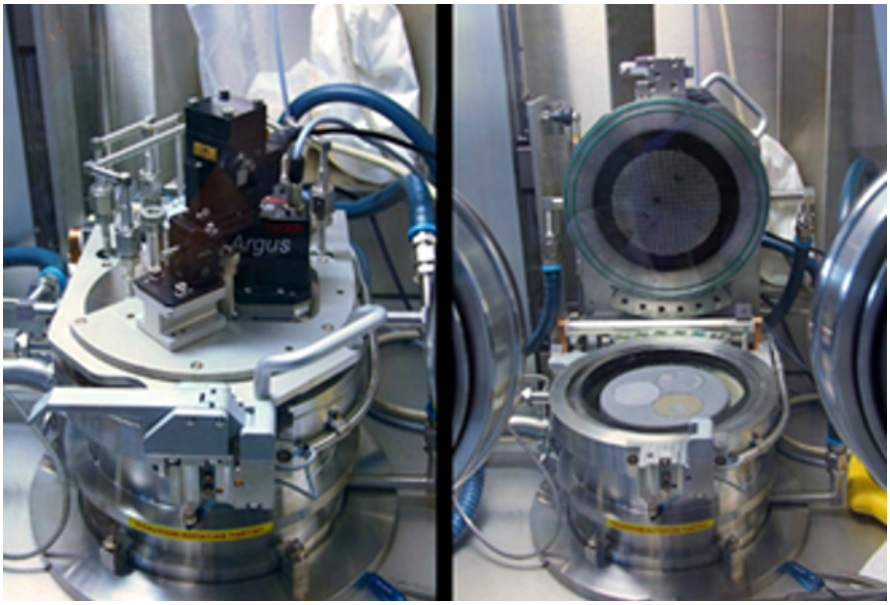

Figure 3.3: A photo of MOVPE showerhead at the Faculty of Physics, University of Warsaw.

Reagents are injected through small (dia. 0.6 mm), densely packed (100/inch^2) holes in the upper lid of the reactor. Chemical reactions occur over three 2" sapphire substrates placed in a graphite susceptor covered by a 100 μm layer of silicon carbide for protection from heat and chemicals. Substrates (together with the susceptor) can be rotated during the growth and are heated from the bottom by a three-zone coil heater. The temperature of the substrates during the growth is read with an optical pyrometer. The pressure in the reactor chamber can be varied from 0 up to 1300 mbar.

All by-product gases from the growth process are neutralized in a *scrubber* purifier and either recovered (ammonia) or released into the atmosphere.

TEB reacts with ammonia by the following chemical reaction:

$$(C_2H_5)_3B + NH_3 \rightarrow BN + 3C_2H_6. \tag{3.1}$$

Growth conditions like temperature, pressure, ammonia, and TEB flows or substrate off-cut influence the quality of the grown sample. hBN used in this work was produced by the following growth modes:

- CFG (*Continuous Flow Growth*). In this mode, precursors are injected into the reactor simultaneously. The growth can occur either in the oversaturation of TEB (very fast) or ammonia (very slow, self-limiting growth) [167]. In this mode, growth conditions must be precisely selected as it is extremely challenging to obtain highly crystalline, epitaxial hBN [168, 169].

- FME (*Flow-rate Modulation Epitaxy*) method involves using alternating TEB and ammonia flow pulses lasting for seconds. This growth technique allows to overcome the self-limiting behavior of hBN layers. However, the produced samples are not of the highest structural quality, with lots of crystal defects [168, 170].

- CGM (*Combined Growth Mode*) developed in-house mainly by Dr. Aleksandra Dabrowska merges two growth modes (CFG and FME) to produce high structural quality material. In this scheme, CFG mode is used to grow a few-layers buffer, and then, FME mode is used to further grow the material. Such a growth mode can be seen as a homoepitaxial growth of hBN on hBN buffer and was found to result in higher crystallinity and better control of the density of point-like defects [171].

3.2 MBE

MBE (*Molecular Beam Epitaxy*) utilizes ultra-pure elements that are deposited onto the substrate in an ultra-high vacuum. $MoSe_2$ layers described in this work were grown in the MBE setup at the Faculty of Physics, University of Warsaw, in the group of Prof. Wojciech Pacuski, by him and MSc. Julia Kucharek. In this setup, two types of element sources are used. In the first one, known also as *Knudsen* or *effusion* cell, elements are stored in special conical crucibles that fit up to dozens of grams of a chosen material. A cylindrical heater is used to heat up the molecular source and control the flux of elements bombarding the substrate. Another element source is used in the case of metals that sublimate at high temperatures. A chosen metal is formed into a cylindrical rod and placed in the molecular source. Then it is bombarded with electrons accelerated by a high voltage applied to a metal rod and a tungsten coil. The bombarded rod heats up and effectively sublimates. The flux of the material can be controlled by applying different voltages. The growth chamber is kept in an ultra-high vacuum ($\sim 10^{-11}$ mbar) provided by a set of vacuum pumps. The setup is equipped with a loading and a preparation chamber to minimize the contamination in the growth chamber. Firstly, membrane and turbomolecular pumps decrease the pressure in the loading chamber down to $\sim 10^{-8}$ mbar, then an ionic pump is used to maintain the pressure of $\sim 10^{-9}$ mbar in the preparation chamber. Another ionic pump, aided by a cryogenic pump allows to obtain $\sim 10^{-11}$ mbar in the growth chamber. Such an ultra-high vacuum allows for molecule-free paths as long as a few kilometers. A custom-cut molybdenum holder can fit various shapes and sizes of growth substrates. MBE allows for a very precise, down to a single atomic layer control of the grown crystal thickness. Such a high accuracy is ensured by the RHEED (*Reflection High Energy Electron Diffraction*) technique. By observing the intensity of the electron beam directed at a small angle to the surface of the growing material, we obtain in-

formation about its structure (whether it is amorphous, polycrystalline, or crystalline).

[This page intentionally left blank]

4

Methods

In this work, the emphasis is set on the optical properties of the materials. The way light interacts with matter can reveal a lot of information about the structure and quality of studied solids. Spectroscopic results complemented by sample morphology imaging provide a powerful tool for studying novel ultrathin structures. In the next sections, we present an overview of characterization techniques used in this work.

4.1 Optical characterization

Scattering is one of the most widespread light-matter interactions. When illuminated by electromagnetic waves, a scattering medium (i.e. molecules, solids, etc.) can change the energy and/or direction of the incident light. Scattering can be separated into elastic (when the energy of the scattered photon is conserved) and non-elastic (when the energy of the scattered photon is not conserved) processes. An example of elastic scattering occurring for the particles (or other medium) of sizes much smaller than the scattered light is Rayleigh scattering, inversely proportional to the fourth power of the wavelength of the light. This process is responsible for example for the blue color of the sky. Usually, about 0.1%-0.01% of the incident photons is a subject to Rayleigh scattering [172].

4.1.1 Raman scattering

Even a smaller amount of incident photons, about 1 in a million is scattered inelastically [173]. A portion of photon energy can be transferred into (or taken from) the vibrational or rotational energy of a scattering medium. When the scattered photon energy is smaller than the incident photon energy, it is referred to as Stokes radiation, when scattered photon gains energy it is anti-Stokes radiation. The effect was predicted theoretically in 1923 by Adolf Smekal [174] and then confirmed experimentally in 1928 by Chandrasekhara Venkata Raman [175], named after him and awarded a Nobel prize in 1930.

In crystals, a photon can be scattered with the creation or annihilation of a phonon (collective excitation in a crystal lattice related to vibrations). First-order Raman scattering is conditioned by the following selection rules:

$$\omega = \omega' \pm \Omega;\ \mathbf{k} = \mathbf{k'} \pm \mathbf{K}, \tag{4.1}$$

where ω, **k** indicate the frequency and wavevector of the incident photon, ω', **k'** – scattered photon and Ω, **K** – phonon [111]. The rules come from the energy and momentum conservation laws and are schematically depicted in Fig. 4.1.

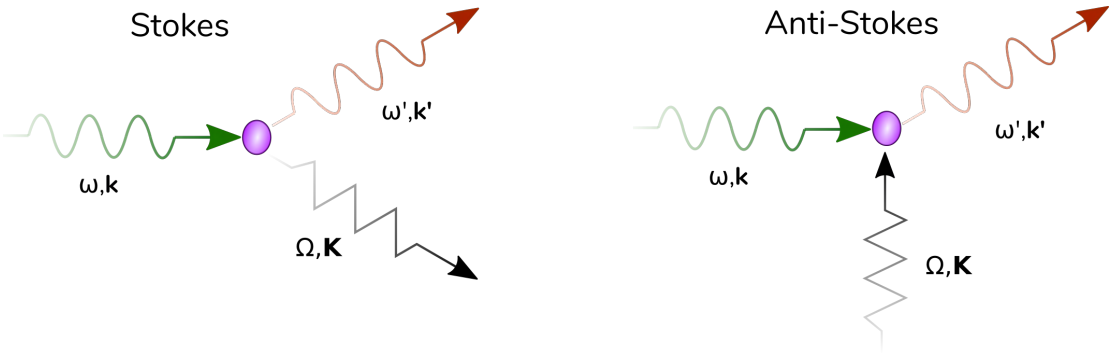

Figure 4.1: A schematic illustration of Raman scattering selection rules [111]. ω, **k** describe the frequency and wavevector of the incident photon, ω', **k'** – scattered photon and Ω, **K** – phonon.

The interaction between electromagnetic waves and matter can be described in terms of electronic polarizability – the tendency of a charge distribution, to be distorted by an external electric field. In the case of Raman scattering, light interacts with the valence band electrons and causes the displacement of the electron cloud in relation to the positively charged nucleus. As a result, a dipole moment **p** arises, and is proportional to the electric field **E** causing it:

$$\mathbf{p} = \alpha \mathbf{E}. \tag{4.2}$$

α denotes polarizability, a coefficient that describes how an electric field applied in one direction affects the charge distribution in a given direction in a material. For isotropic molecules, polarizability is a scalar. In general, however, the material can be anisotropic and interact with light differently, depending on its direction. Hence, polarizability can be described by

a tensor α that satisfies the following equation [176]:

$$\alpha_{ij} = \begin{bmatrix} \alpha_{xx} & \alpha_{xy} & \alpha_{xz} \\ \alpha_{yx} & \alpha_{yy} & \alpha_{yz} \\ \alpha_{zx} & \alpha_{zy} & \alpha_{zz} \end{bmatrix}, \tag{4.3}$$

where x, y, z components denote directions of the incident light (i) and the second (j) the direction in the material.

In solid-state, polarizability is usually defined as a dipole moment per unit volume. The intensity of the electric vector is time-dependent. Hence, the dipole moment is subjected to oscillations, which means that the polarizability is also changing. In a harmonic approximation, the polarizability can be denoted as:

$$\alpha_{ij} = (\alpha_{ij})_0 + \left(\frac{\partial \alpha_{ij}}{\partial Q}\right)_0 Q, \tag{4.4}$$

where Q describes the nuclei displacement from the equilibrium, and $(\alpha_{ij})_0$ describes the nuclei equilibrium position. Vibrations that cause the change of polarizability: $(\frac{\partial \alpha}{\partial Q})_0 \neq 0$ are Raman active [177, 178].

Raman scattering is highly dependent on the crystal symmetry, as well as the polarization of the incident light. Indeed, in order to theoretically determine which phonon modes are Raman-active, one must look into the symmetry group of a given material and find the irreducible representations. The group theory predicts which irreducible representations with basis functions corresponding to quadratic terms of *x,y,z* are Raman-active [179].

Additionally, polarizability depends on the frequency of the scattered light, therefore some Raman modes can be observed only for specific excitation wavelengths. Exciting the material with photons whose energy corresponds to the energy of so-called van Hove singu-

larity [180] (resonant Raman scattering) also provides information about electronic energy bands.

The Raman tensor ($\hat{R}$) is a mathematical representation that describes the change in polarizability of a material, and can be defined as a derivative of polarizability with respect to the displacement coordinate (Q) [181]:

$$\hat{R} = \frac{\partial \alpha}{\partial Q}. \tag{4.5}$$

Polarization-resolved measurements allow to designate parameters of the Raman tensor of a given material. While studying the samples' response to a linear polarization excitation, one can expect the intensity of scattered light to behave like:

$$I \cong |e_s \hat{R} e_i|^2, \tag{4.6}$$

where e_s – scattered light vector, e_i – incident light vector, $\hat{R}$ – Raman tensor corresponding to a specific mode symmetry. In the experiment, it is important to carefully define the laboratory setup orientation in relation to the crystal axes and light polarization direction.

Raman scattering is a powerful tool for quick and non-invasive study of various materials, including ultrathin crystals. It does not require specific sample preparation and can be used with micrometer precision. Such precise, micrometer-scale mapping allows for local studies of the properties of the material like local strain or defects. In the case of 2D materials, it can determine the number of layers of a crystal due to the smaller number of available phonon modes in the few-layer limit or can help to determine twisting of subsequent layers in the structure [179, 182–184].

4.1.2 Photoluminescence

When interacting with matter, light can be also absorbed, leading to the excitation of an electron to a higher energy state. In semiconductors, a photon with an energy higher than the band gap can excite an electron from the valence band to the conduction band. Then, by non-radiative processes, the electron can lose some energy and eventually come back into its ground state by emitting a photon. The described phenomenon is called photoluminescence and for example, can be used to study the bandgap of various materials [185, 186]. However, photoluminescence can also be observed when the energy of the excitation photon is lower than the material's bandgap. Such a behavior can be attributed to phenomena like excitons and defects, both of which are of interest to this work.

Excitons An electron can be excited to a higher energy state. Then, it interacts (Coulomb interaction) with a positively charged hole in the valence band. This bound state can be treated as a quasiparticle – exciton, characterized by a wavevector describing its propagation through the crystal lattice. The energy needed to separate the electron and hole is called the binding energy (schematically depicted in Fig. 4.2).

Traditionally, excitons are usually categorized into two limiting cases: localized and delocalized.

Tightly bound, Frenkel excitons are usually well localized around a specific atom or a unit cell. Such excitation can travel through the crystal by hopping between neighboring atoms. Frenkel excitons are usually found in alkali halides and molecular crystals and manifest binding energy in the 0.1-1.5 eV order of magnitude [111].

Delocalized excitons with big radii (also called Wannier-Mott excitons) are weakly bound. Their binding energy is in the range of a few to hundred meV. Such excitons usually appear

in materials with a high dielectric constant, which results in electric field screening and reduction of the electron-hole Coulomb interaction. In 3D, Wannier-Mott exciton binding energy can be described by a modified hydrogen Rydberg equation, including electron and hole effective masses [111].

Studies of excitonic behavior in 2D systems unveiled many interesting many-particle phenomena. In the few-layer limit, the dielectric screening is relatively weak. This, combined with large geometrical confinement leads to strong Coulomb interactions, allowing for the observation of various types of excitons, also at high temperatures [187–189].

In this work, we focused on studying the excitons in TMDC layers as indicators of the optical quality of the samples. TMDC, as one of the most intensively studied families of 2D materials, provided a plethora of excitonic processes, revealing information about the materials' properties and their potential applications.

In TMDC, we observe a different optical response, as a function of the number of layers. Due to the weaker interlayer interactions, recorded exciton energies differ. For some of TMDC, like MoS_2 or $MoSe_2$, the nature of the bandgap changes from an indirect to direct in their monolayer limit [83, 84, 190], making photoluminescence measurements a powerful tool for studying the thickness of these materials.

Additionally, TMDCs manifest a large spin-orbit coupling – an interaction of a particle's spin with its motion inside a potential. Such a coupling results in energy levels splitting in the valence and conduction band. In molybdenum and tungsten-based TMDC, band separation can reach as much as 200-400 meV, allowing observable optical transitions [191].

Circular dichroism – a phenomenon, where left-, or right-hand side circularly polarized light interacts differently with a material is also present in TMDC. The material excited by a circularly polarized light manifests optical transitions only in K+ or K- valley (extrema in the band structure), depending on the polarization direction [192–194]. Excitons can then form

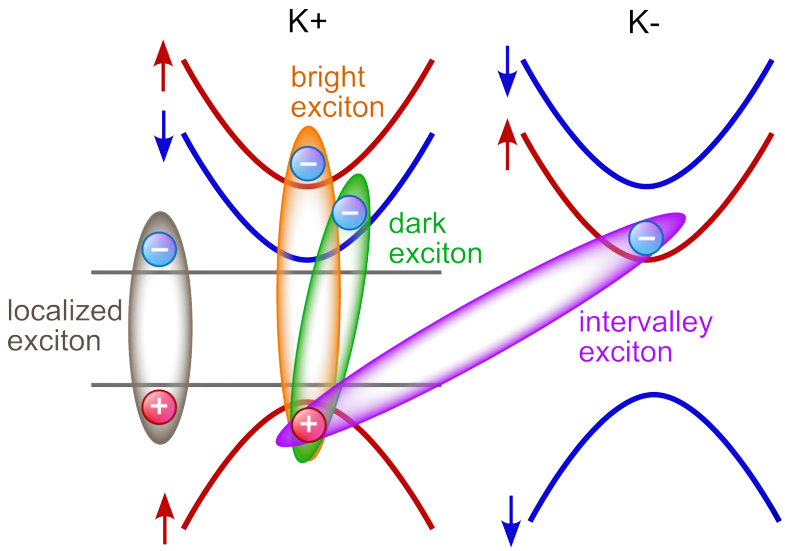

Figure 4.2: A schematic illustration of exciton types found in TMDC. Figure based on [188].

between different valleys, opening the door for *valleytronics* – a field utilizing valley degree of freedom to store and process information [195].

TRIONS Electron-hole complexes are not the only possible ones found in semiconductors. As first proposed by Murray A. Lampert in 1958, we can observe charged excitons, also called trions [196]. Trions can be either positively or negatively charged, consisting of two holes and one electron, or two electrons and one hole [197]. Charged excitons offer a great platform for investigating spin physics or electron-nuclei hyperfine structures in 3D confined systems [198]. In the field of 2D materials, trions are interesting for fundamental studies of many-body interactions as well as for valleytronic or optoelectronic applications [90, 199].

In high-quality, monolayer materials like $MoSe_2$, exciton charging can be electrostatically tuned. By fabricating a field effect transistor and applying a gate voltage, excitons within the sample can be converted from neutral to positively or negatively charged. Such a tuning is necessary for the development of optoelectronic devices like light sources, excitonic circuits, or photodetectors [200].

4.2.1 SEM

Scanning Electron Microscopy (SEM) is a powerful tool for studying the morphology of the samples on the nanoscale. In this method, the sample is scanned with a focused electron beam. The electrons' wavelengths are orders of magnitude shorter (in the range of several picometers) than that of visible light, which allows it to overcome the diffraction limit present in optical microscopy. The electron beam originates from the electron gun and can be altered by the accelerating voltage and current intensity. Electrons interact with the studied specimen on different depths. In the most common mode Secondary Electrons (SE) are detected. SE originate from the atoms excited with the primary electron beam. They possess relatively low energy ($\sim$50 eV) so they can only come from a few nanometers deep into the sample. SE are well localized and allows to image the topography of the sample with more than 1 nm resolution. Another SEM mode involves detecting Back-Scattered Electrons (BSE). These are the high-energy electrons elastically scattered from the sample from higher depths (>50 nm) and can provide information about the atomic number of the studied specimen. The electron beam focused on the sample can also stimulate the emission of characteristic X-rays. Such an analysis allows to learn about the chemical composition of the studied material [201, 202].

SEM images presented in this work were collected with a *Dual Beam HELIOS NanoLab 600* setup equipped with Energy dispersive X-ray add-on.

4.2.2 AFM

Atomic Force Microscopy (AFM) allows to determine the thickness of the samples with theoretical precision up to 0.01 nm. The principle of operation is based on measuring the in-

teraction between a mechanical probe and the sample. The probe is built out of a cantilever ended with a sharp tip. The laser light reflects from the cantilever and is detected by a photodiode, providing a signal about the position of the cantilever to the feedback loop. During the measurement, the probe is scanning over the sample. Due to the van der Waals interaction, the cantilever is either attracted or repelled from the sample. The probe can either touch the studied material (contact mode) or stay at some distance from it (non-contact mode). Each mode has its benefits and drawbacks and needs to be selected according to the properties of the specific sample.

AFM imaging of the samples studied in this work was performed on *Scienta Omicron VT XA* and *Bruker Dimension Icon Nanoscope VI* systems.

Figure 4.3 presents a comparison between the two described morphology imaging techniques: AFM and SEM.

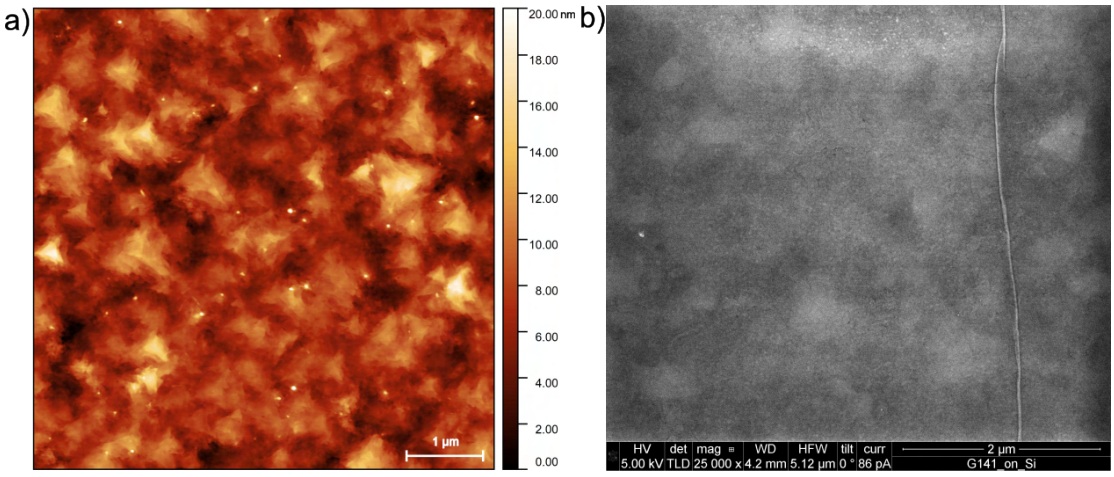

Figure 4.3: A comparison between the a) AFM and b) SEM image of the same hBN sample transferred onto a silicon/silicon dioxide substrate.

4.2.3 Optical microscopy

Optical imaging was an indispensable part of preparing samples studied in this work. This imaging technique is limited by the visible light wavelength used to illuminate the specimen. The resolution can be described by the following equation: $d = \frac{\lambda}{2NA}$, where d is the smallest visible object, λ – wavelength of the light used for illumination, NA – numerical aperture of the objective.

Optical microscopy is extremely useful when determining the thickness of flakes of the nanomaterials. Light reflects from different surfaces of the sample: for example: from the exfoliated flake, SiO_2 layer, and silicon substrate. Then, the reflected rays interfere with each other resulting in visible for an eye optical contrast and various colors for different thickness of the nanocrystals [203]. Comparison of AFM and optical images allows to calibrate which observed optical contrast corresponds to which number of layers, and provides an easy and quick method to precisely determine the thickness of the flakes (fig. 4.4).

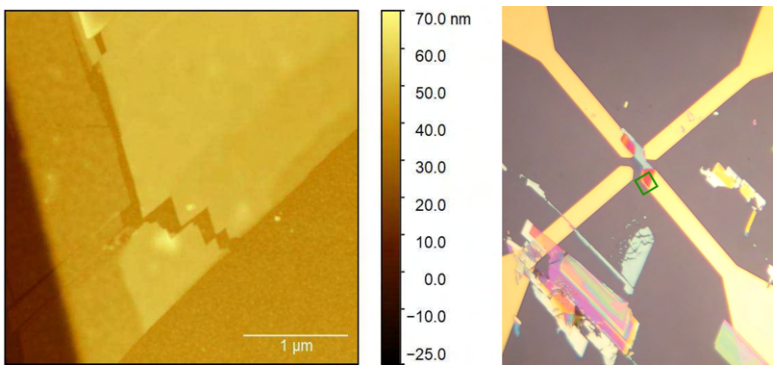

Figure 4.4: Left: AFM measurement of a $CrPS_4$ flake showing its thickness. Right: Optical image of the region measured by AFM. After calibration with AFM images, optical contrast can quickly provide information about the thickness of the layers.

[This page intentionally left blank]

5

Experimental

5.1 Measurement setups

5.1.1 Optical spectrometers

The optical spectrometer is an instrument that allows studying the intensity of light as a function of energy. In this work, the emphasis is put on the optical properties of chosen materials, hence spectrometers were the basic tools for most of the measurements. During the studies, two main setups were used: Renishaw inVia spectrometer with a relatively easy user inter-

face and just a few personalization functions, and a much more customizable spectrometer: HORIBA T64000. In the next paragraph, principles of operation are presented.

Horiba spectrometer

Figure 5.1 shows a photo of the used setup, as well as the Horiba T64000 spectrometer construction. The setup is equipped with 325 nm, 442 nm, 532 nm, 633 nm, 785 nm, and 1064 nm continuous wave laser sources. Light from the laser is directed to the microscope and focused on the sample. Then, after interacting with the sample, the light goes back through the objective and enters the spectrometer slit. Then the light is split by a diffraction grating and then detected by a CCD camera. The setup features a mode using three diffraction gratings for higher resolution. Such a setting involves more reflections and significantly reduces the intensity. Since measurements performed for this work required a cryostat (light had to pass through the glass window) and spatial mapping, while simultaneously not requiring the highest resolution, we used the spectrometer in single-grating mode.

The setup is equipped with mounts compatible with a constant-flow cryostat MicrostatHires Oxford Instruments, allowing measurements to be performed down to 4 K. Temperature control is ensured by an Oxford Instruments MercuryiTC controller. A motorized stage (Thorlabs) with 100 nm spatial resolution and in-house software allows spatial mapping of the samples. Additionally, samples can be electrically contacted, and voltage can be applied with an Agilent B2901 source measured unit.

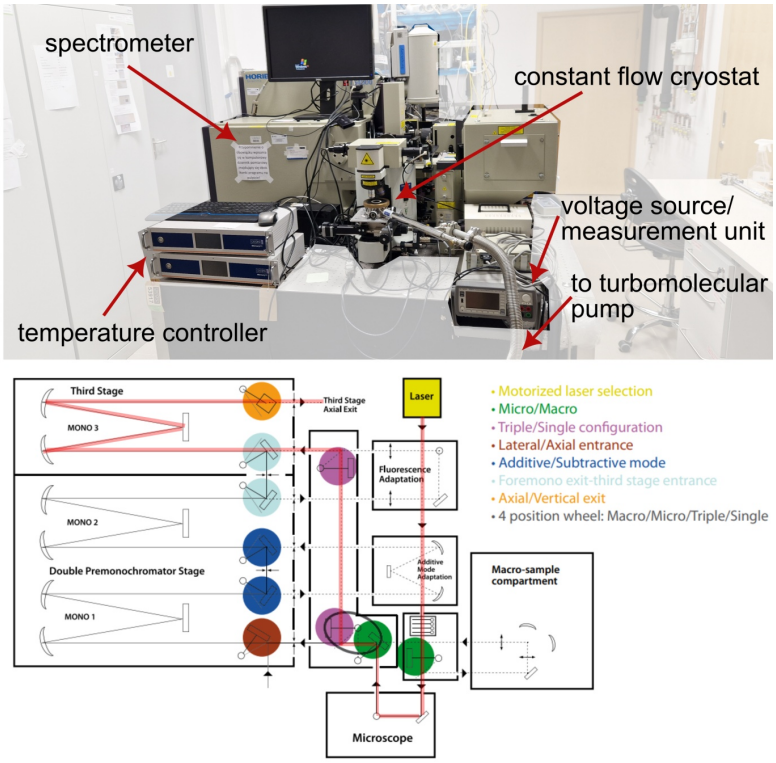

Figure 5.1: Top: a photo of a used Horiba spectrometer with additional equipment. Bottom: schematic illustration of the spectrometer setup (illustration comes from the official Horiba user manual).

Renishaw inVia spectrometers

Our group possesses two Renishaw inVia spectrometer setups with confocal microscopes and slightly different hardware and software specifications. One system is equipped with continuous wave laser sources of: 532 nm, and 785 nm, while the other one offers 633 nm, and 785 nm laser illumination. Setups contain XYZ motorized stages with a 100 nm step, that allows precise and automated mapping of the samples. One of the setups, presented in Fig. 5.2 offers measurements with different light polarizations as well as an automatic focus during mapping.

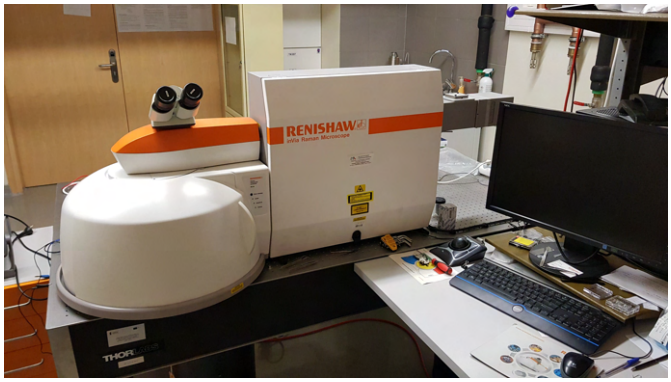

Figure 5.2: A photo of the Renishaw spectrometer setup used in this work.

Magneto-optical setup

Thanks to the courtesy of Prof. Maciej Molas and his group, a part of the measurements for this work was conducted in his laboratory equipped with the superconducting magnet *Cryogenic*, able to provide magnetic fields as high as 17 T (fig. 5.3). In this setup, the sample is mounted on a special probe equipped with precise piezoelectric *Attocube* positioners. Measurements are possible in a wide range of temperatures (6-300 K). The employed *Attocube* objective works in high magnetic fields and low temperatures and can focus the incident beam to an excitation spot of about 1 μm^2. The signal is detected by *Princeton Instruments SpectraPro HRS* spectrometer equipped with three diffraction gratings (300, 600, and 1800).

5.2 Sample preparation and manipulation of ultrathin layers

5.2.1 Mechanical exfoliation

Mechanical exfoliation is the most widespread technique of obtaining ultrathin layers from bulk van der Waals crystals. It is also called a ”scotch tape” method, as it utilizes special adhesive tapes [204]. To perform mechanical exfoliation, a bulk crystal is placed in the middle of a piece of tape, which is then repeatedly stuck and peeled off to uniformly spread the material

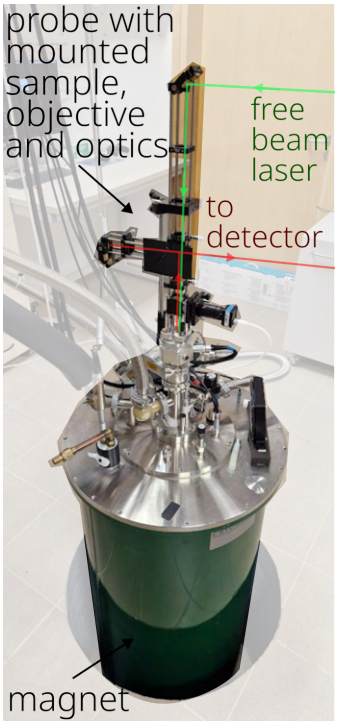

Figure 5.3: A photo of the used superconductive magnet.

over the entire tape. It is then glued to the chosen substrate, and very slowly removed after at least one hour. The process results in a random distribution of flakes with different sizes and thicknesses. The method is quick and simple, however small sizes of obtained flakes and their random properties prevent its use on a larger than laboratory scale.

In order to place flakes onto the desired areas on the sample (such as contacts or other flakes), a polydimethylsiloxane (PDMS) stamp can be used [205]. A schematic illustration of this process is depicted in fig. 5.4. In the used method a PDMS film (in our work also called gelfilm, from the company name) is placed on a microscope slide and secured with adhesive tape. Then, the tape with the exfoliated crystal is glued to the gelfilm. After some time (depending on the exfoliated material) the tape is quickly removed. Then, the microscope slide can be put upside down in a precision mount in order to embed flakes in a specific place.

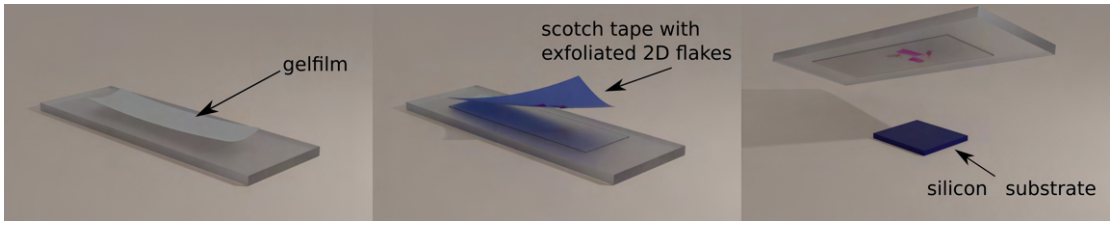

Figure 5.4: Schematic illustration of a mechanical exfoliation scheme using a PDMS film to transfer ultrathin flakes.

In this work we used a mask aligner – a device originally used to precisely position lithography masks, to create heterostructures of nanomaterials. The setup is shown in fig. 5.5.

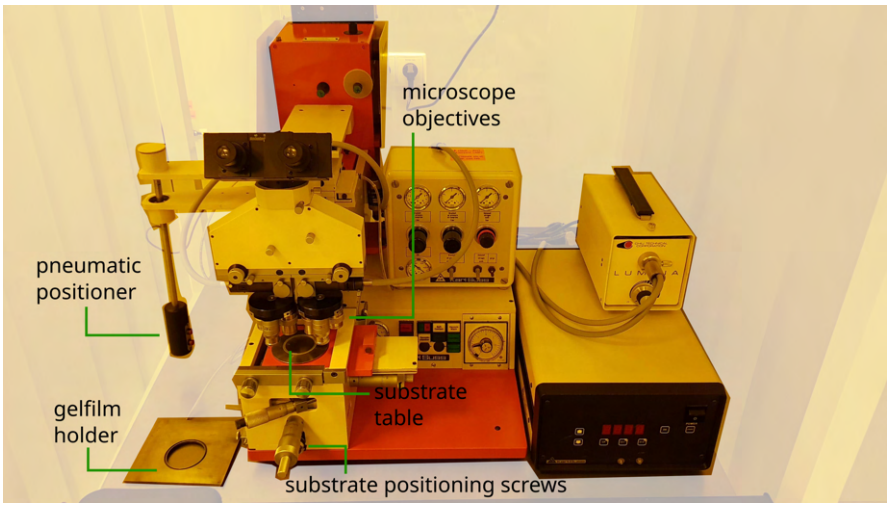

Figure 5.5: A photo of the mask aligner setup Karl Suess MJB 3. In this work, it was used to precisely transfer ultrathin flakes.

The microscope slide was mounted upside down in a non-moving holder. A new substrate is mounted with adhesive tape to a moving table equipped with micrometer screws. The gelfilm and substrate were very carefully and slowly put in contact. After some time (usually $\sim$30 min), layers were carefully moved away from each other.

5.2.2 Delamination and transfer of large-area layers

MOVPE growth of hBN layers is conducted at temperatures as high as 1300-1400°C. Such conditions require taking into account the thermal expansion coefficients of the substrate and grown material to understand their morphology and interface. In the case of hBN and sapphire, the difference is relatively large, as the thermal expansion coefficients are -2.83 $\times$ 10^{-6} K^{-1} for hBN [47] and 9 $\times$ 10^{-6} K^{-1} for sapphire [206]. During the growth, the hBN layer lies flat on the substrate. The situation changes when the sample is cooled down to room temperature. The hBN layer expands more than the sapphire substrate shrinks. If the material is continuous and of good crystallinity, it forms wrinkles on the entire surface, which house material separated from the substrate (fig. 5.6 g). Rather counterintuitive, the appearance of the wrinkles was found to actually relax the material [207–209]. If the adhesion of hBN layers to the sapphire wafer is weak, the material can "slide" on the substrate during the cool down [210].

We observed, that when the sample is immersed in a polar liquid (ex. water), the hBN layer delaminates and floats, allowing it to be transferred onto a different substrate. The occurrence and speed of delamination depend mostly on the thickness and growth mode of the sample. During the optimization, we noticed that in general, the thicker the hBN layer, the better it delaminates. More than $\sim$50 nm thick samples detached in the blink of an eye when put into the water. The process was so sudden, that sometimes it resulted in the segmentation of the layers. On the other hand, thinner samples needed more time to delaminate, and for some (thicknesses <8 nm) immersion did not initiate the detachment from the substrate.

We discovered that reducing the surface tension by adding isopropanol, significantly improves the delamination process of thin samples, while simultaneously making it less sudden. At the same time, too high contents of isopropanol in the solution with water resulted in too

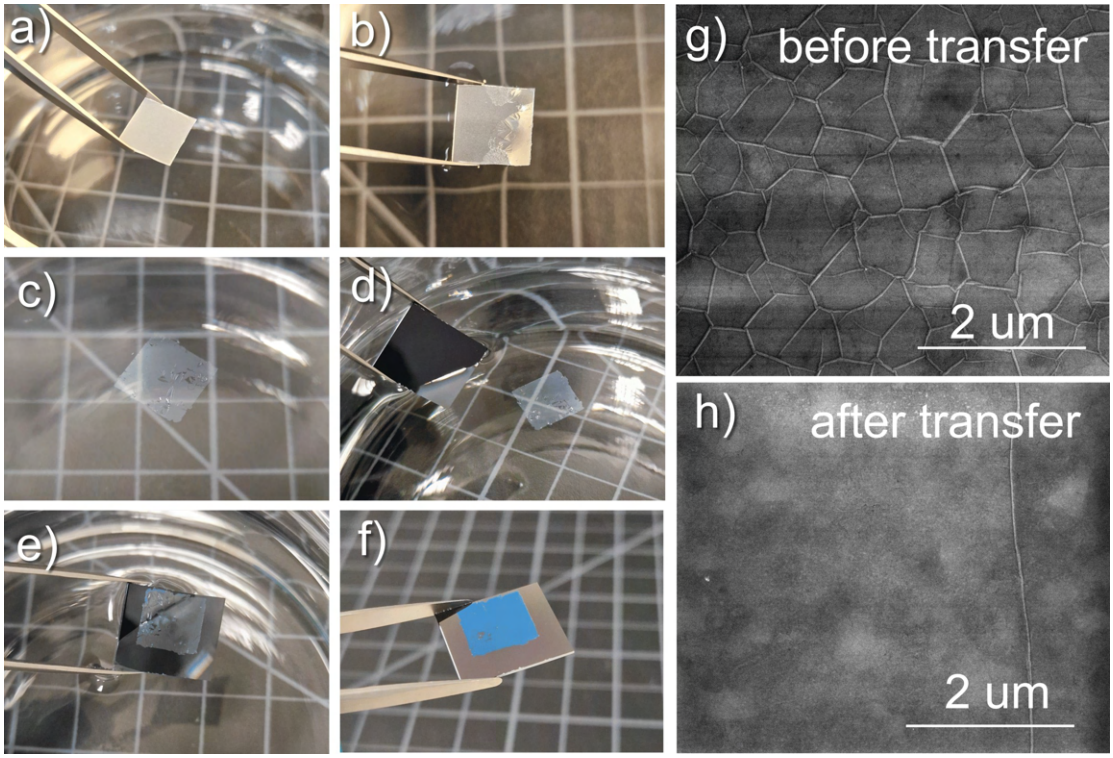

Figure 5.6: Schematic illustration of macroscopic hBN layer transfer. a) A photo of an as-grown 16 nm thick hBN layer on a sapphire substrate. b) When immersed in a water-isopropanol solution, the material gradually delaminates from the substrate. c) The delaminated ultrathin hBN floats on the liquid surface. d, e) The layer can be delicately transferred onto another substrate. f) An hBN layer transferred onto silicon/silicon dioxide substrate. After drying on a hot-plate 16 nm thick hBN layer appears bluish. g) SEM image of as-grown MOVPE hBN layer, shows a characteristic mesh of wrinkles. h) SEM image after the transfer shows that the wrinkles vanish after the delamination.

little surface tension and drowning of the whole sample without triggering the delamination. We have determined the optimal water-isopropanol solution to be ∼10:1.

We found a way to delaminate also thin samples (<8 nm), by sticking a PDMS frame onto them. The frame worked in two ways: it applied additional stress on the structure, allowing it to delaminate, or initiated the delamination by mechanically unsticking the ultrathin layer. By this method we managed to transfer hBN samples as thin as ∼1 nm.

Fig. 5.6 a-f) shows photos of a transfer of a ∼16 nm thick hBN sample. As described ear-

lier, the sample was carefully immersed in water-isopropanol solution to trigger the delamination. Parts of the hBN layer adhered better to the substrate, demanding careful handling and a low immersion speed. The $\sim 1 \times 1$ cm material was successfully moved to a silicon/silicon dioxide substrate without any significant ruptures. The sample was pulled out of the solution very slowly to dispose of excessive liquid residues. After the process, the sample was heated on a hot-plate at first at $\sim 80^{\circ}$C for 5 minutes to avoid boiling the remaining water, and then at $\sim 150^{\circ}$C for at least half an hour.

SEM images collected after the transfer show, that the hBN layer significantly flattens out (fig. 5.6 h). Indeed, floating layers without contact with the substrate straighten out and behave like a very thin plastic foil. During the pull-out, some parts of the layer stick to the new substrate quicker than the others which results in the formation of folds (fig. 5.6 h). Still, the transferred sample is much smoother allowing for better imaging for example by AFM.

The presented wet exfoliation and transfer method was used to prepare substrates for MBE growth of other materials presented in chapter 6 and heterostructures with 2D magnets described in chapter 7.

[This page intentionally left blank]

6

Heteroepitaxy

6.1 Introduction

The incorporation of atomically thin materials into real-world devices requires major advancements in their fabrication schemes. Mechanical exfoliation allows to produce high-quality samples and to realize proof-of-concept ideas. However, the scalability, homogeneity, and repeatability limitations still suppress the applications with 2D layers. The scalability constraint has been addressed for some time by the optimization of wafer-scale growth tech-

niques [211, 212]. One of the most popular approaches includes the development of CVD (chemical vapor deposition), PVD (physical vapor deposition), thermolysis and laser annealing methods [213–218]. The structural, electrical, and optical quality of such structures still remains inferior to their mechanically exfoliated counterparts. Some of the approaches involve post-processing of the samples: further transfer or encapsulation of the grown layer, which allows for improved quality of the material [219, 220].

Another promising approach is using epitaxial methods like MBE and MOVPE to produce large-area materials [221]. MBE offers the fabrication of high-purity material with atomic precision [222–227]. However, it is also a time-consuming technique, making it non-efficient for the growth of thicker samples. Therefore, the approach when MBE is used to create just a single layer of material on an appropriate substrate seems like a viable option.

As shown before by the group of Prof. Wojciech Pacuski, MBE can be used to fabricate high optical quality monolayer material on previously exfoliated hBN flakes on silicon/silicon dioxide substrate [228]. The optical quality of the samples was probed by photoluminescence studies and demonstrated by narrow and well-resolved excitonic lines at cryogenic temperatures. The proximity of atomically flat hBN layers without so-called out-of-plane dangling bonds helps to improve the dielectric surrounding and, as a result, optical properties of other materials like TMDC, in particular, $MoSe_2$. The size of hBN flakes limited the area of high-quality $MoSe_2$ layers. In this work, we show that the epitaxial growth of high-quality $MoSe_2$ can be extended using large-area hBN layers grown by MOVPE, making it a fully scalable solution.

MOVPE provides a reliable method to produce large-area materials layer by layer at a relatively high speed [171]. In this work, we followed two main fabrication schemes illustrated in figure 6.1. One approach was to grow MOVPE hBN on a 2” sapphire substrate and subsequently grow MBE $MoSe_2$ on the as-grown sample. The second approach included also

an additional step of large-area hBN transfer onto another substrate (silicon/silicon dioxide) and only then MBE growth of $MoSe_2$. Such an approach allowed us to clear out the wrinkles formed on hBN samples, thereby allowing better surface imaging. The transfer step made it also possible to electrically contact the sample and control its charge carrier populations.

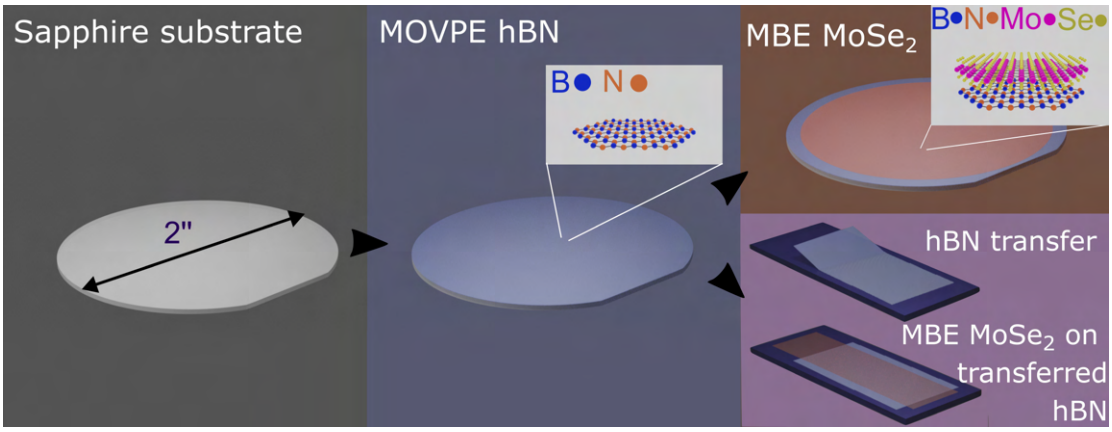

Figure 6.1: Schematic illustration of a heteroepitaxy sequence. Firstly, hBN is grown by MOVPE on a 2" sapphire substrate. Subsequently, MBE is used to grow a single layer of $MoSe_2$. Alternatively, after MOVPE growth, large-area hBN layers can be transferred onto other materials like silicon/silicon dioxide, and subsequently, $MoSe_2$ can be grown on top using MBE.

The next sections present the results of such heteroepitaxial growth of large-area hBN/$MoSe_2$ structures.

6.2 MBE growth on as-grown MOVPE hBN

The starting point of our study was using as-grown MOVPE hBN as a substrate for MBE growth of $MoSe_2$. During the studies we tested 11 hBN substrates, however, for clarity we present results for three representative hBN samples. On each of the hBN samples, we performed several MBE growths with varying growth times and number of annealing steps. Table 6.1 presents the growth parameters of the studied samples.

While choosing hBN substrates, we focused on the ones with high crystallinity, as they

Table 6.1: Growth parameters of the samples used in this study. hBN samples vary by their thickness. Each MBE process resulted in depositing ∼1 ML of $MoSe_2$, however, each was performed at a different rate and with a different number of annealing steps. Sample indices in the brackets correspond to the indices used internally by the group.

MOVPE		
sample	**thickness**	**growth mode**
hBN1 (G065)	13.6 nm	CGM
hBN2 (G037)	3.5 nm	CGM
hBN3 (G004, G081)	1.5 nm	CFG
MBE		
sample	**time of growth**	
$MoSe_2$A	15 h	
$MoSe_2$B	5 h	
$MoSe_2$C	5x1 h	

should provide the best environment for other 2D materials. On the other hand, the thickness of the hBN spacer also plays an important role, as the interaction with the substrate is present even with spacers ∼40 nm thick [229]. MOVPE allows to grow high-quality hBN layers by performing described in 3.1 section CFG (Continuous Flow Growth) mode, which manifests a self-limiting behavior [230]. In this work, apart from samples grown with CFG (Continuous Flow Growth) mode we studied also thicker samples obtained by the in-house developed CGM (Combined Growth Mode) technique described in 3.1 section [171].

Fig. 6.2 a-d) shows the morphology of the thickest (hBN1) and thinnest (hBN3) of the studied samples. SEM and AFM images provide information about the characteristic wrinkle mesh that appears in hBN layers as a result of the cool-down after the high-temperature growth. Apart from the wrinkles, three-dimensional precipitates also appear on the surface of the sample. Their presence is related to the formation of out-of-plane nucleation centers during the MOVPE growth process. Images show, that the thinner the hBN layers, the less visible and finer is the wrinkles mesh.

The employed hBN layers were further characterized by Fourier transform infrared spec-

troscopy (FTIR). Fig. 6.2 e) depicts spectra obtained for samples hBN1 and hBN3. Fits obtained by Dynamic Dielectric Function approximation allowed us to precisely determine the thickness of the layers [171]. The observed peak ∼1367 cm^{-1} corresponds to the IR active mode E_{1u}, confirming the formation of a sp^2 hybridized material [231].

The X-ray diffraction studies presented in fig. 6.2 f) provide information about the structural quality of the hBN layers. For sample hBN1, the peak is observed at 26.3°, which indicates a majority contribution of hBN with a small addition of tBN. For sample hBN3 the signal is much broader, less intense, and shifted to 24.7° suggesting mostly turbostratic (tBN) contribution [168].

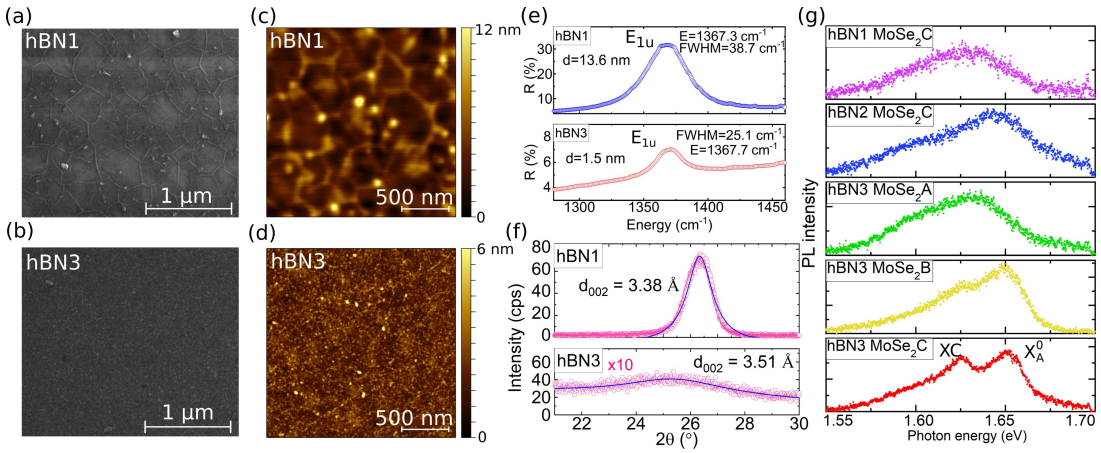

Figure 6.2: SEM images of samples a) hBN1 and b) hBN3. The thinner the sample, the smaller and less visible the post-growth wrinkles mesh is. AFM images of samples c) hBN 1 and d) hBN 3. e) FTIR spectra collected for samples hBN1 and hBN3 allow to precisely determine their thickness. f) X-ray diffraction provides information about the structural composition of the samples. Sample hBN1 contains mostly hBN with a small addition of tBN, while sample hBN3 consists mostly of tBN. g) Low-temperature PL spectra collected for different MBE growths ($MoSe_2$A-C) on different MOVPE hBN samples (hBN1-3).

Fig. 6.2 g) shows the low-temperature (5 K) PL spectra for $MoSe_2$ layers grown by various MBE processes on various hBN samples. The high optical quality of the $MoSe_2$ layer can be shown by separated excitonic lines corresponding to the A exciton (X_A^0) and charged exciton

(XC) also called trion. Such a separation was mostly observed for mechanically exfoliated material [200, 232–234] and for MBE grown $MoSe_2$ on mechanically exfoliated hBN [228].

The starting point of the optimization for heteroepitaxial growth was utilizing a long (15 hours) MBE process ($MoSe_2$A) which proved successful in the growth on exfoliated hBN flakes. This approach resulted in a broad PL spectrum, which could indicate the formation of more than one layer of the material. As a result, we shortened the MBE growth time (5 hours), which positively impacted the optical quality of the fabricated samples, by narrowing the low-temperature PL signal. The best outcomes were achieved after introducing several annealing steps into the MBE process (5 times 1-hour long growth). The comparison of PL spectra obtained for three hBN samples of different thicknesses which underwent the same MBE process ($MoSe_2$C), shows that the best separation of excitonic lines is achieved for the thinnest hBN layer.

To further confirm the formation of $MoSe_2$ layer in the samples, we performed TEM imaging of the cross-section of sample hBN3 $MoSe_2$C (fig. 6.3). At the bottom, a well-ordered sapphire substrate is visible. Then, a thin layer of aluminum nitride followed by a layer of amorphous BN (aBN) is visible. Such a structure is typical for high-temperature MOVPE hBN growth [171]. Around $\sim$1 nm thick hBN layer can be seen, which is in agreement with the FTIR measurements. We see, that the hBN layer is not perfectly continuous, but rather forms islands. Nevertheless, it appears in most areas of the sample. On top of the BN layer, a monolayer $MoSe_2$ is visible. The material reproduces the shape of BN layers, making it difficult to obtain an image of a long segment of monolayer $MoSe_2$. The sample had to be additionally covered by an Au cap, in order to eliminate the charging effects. The deposition of the cap could partially destroy the delicate $MoSe_2$ layer.

The blue area marked in fig. 6.3 b) was used to extract the intensity graph shown in fig. 6.3 c). The profile allows us to extract the interlayer spacing to be 0.34 nm which is slightly

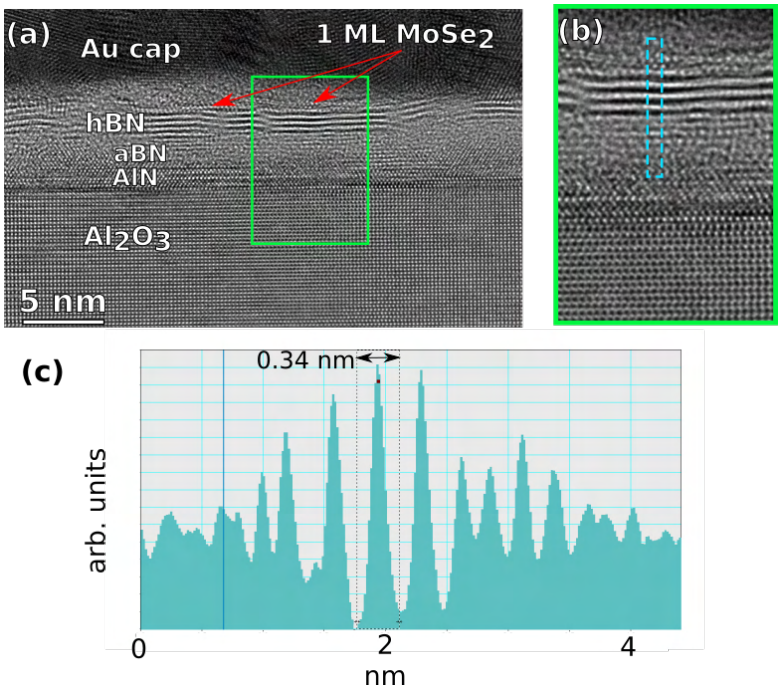

Figure 6.3: Transmission electron microscope (TEM) image of the sample hBN3 $MoSe_2$C. a) The cross section shows the sample's layers: a sapphire substrate, interface made out of AlN and amorphous BN, and ∼1 nm thick layer of hBN followed by a monolayer $MoSe_2$. The sample is covered by an Au cap, to prevent charging. b) Zoom-in of the area marked in green in panel a). c) Intensity profile showing 0.34 nm interlayer spacing between BN layers.

larger than the literature value of 0.33 nm for hBN [40]. This result corresponds with the XRD measurements suggesting a mostly turbostratic layer stacking for ultrathin BN layers [171, 210].

Figure 6.4 shows a comparison of low-temperature PL spectra collected for heteroepitaxial sample hBN3 $MoSe_2$C and $MoSe_2$ layer grown by MBE directly on a silicon/silicon dioxide substrate. Panel a) depicts two excitonic peaks typical for $MoSe_2$. Peaks correspond to the neutral A exciton at 1655 meV and trion at 1627 meV. The obtained values are in agreement with previous reports [200, 232, 235, 236]. The width of the peaks is 22 meV which is still an order of magnitude higher than the values obtained for the best points found in mechanically exfoliated samples [109]. However, our heteroepitaxial technique shows a

two-fold improvement in comparison to the material grown directly on the Si/SiO_2 (panel b in fig. 6.4). Additionally, the intensity of the recorded peaks is more than an order of magnitude higher than the one found in $MoSe_2$ on Si/SiO_2.

The inset in fig. 6.4 shows the PL spectrum of sample hBN3 $MoSe_2$ in a larger spectral range. Marked in pink features at $1.7 - 1.8$ eV correspond to the sapphire substrate, and the background emission originates from the defect states in the hBN layer [237].

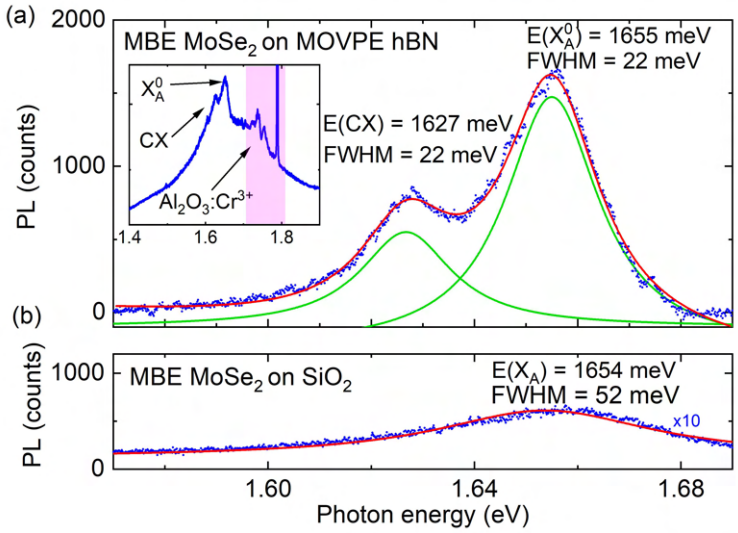

Figure 6.4: A comparison of low-temperature (5 K) PL spectra (532 nm CW laser excitation) gathered for a) heteroepitaxial sample hBN3 $MoSe_2$ and b) MBE growth of $MoSe_2$ directly on the Si/SiO_2 substrate. The excitonic peaks are well-resolved and relatively narrow for the heteroepitaxial sample. The inset shows the PL signal at a larger spectral range. Features originating from the sapphire substrate (pink area) as well as a high-intensity background originating from defect states in hBN are visible.

To further characterize the samples, we performed temperature-dependent PL measurements. The result of this experiment is depicted in fig. 6.5. We observe a red shift and widening of the excitonic peaks, as well as the disappearance of the XC signal with the increasing temperature. The red shift is a well-described phenomenon arising from the reduction of the band gap in $MoSe_2$ with rising temperature [200, 238]. Fig. 6.5 b) shows the extracted energies of the neutral and charged excitons with fits adapted from [200].

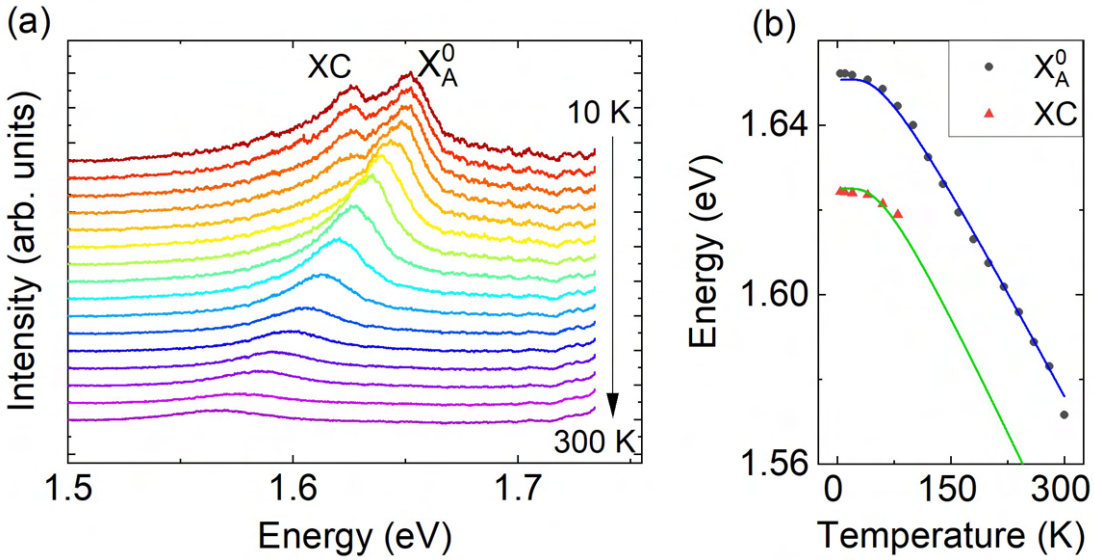

Figure 6.5: a) Temperature evolution of PL spectra collected for sample hBN3 $MoSe_2$C. b) Energy dependence for the neutral and charged exciton with fits adapted from [200]. The temperature evolution is typical for unstrained $MoSe_2$ layers.

The result indicates a typical band-gap energy dependence found in unstrained $MoSe_2$ layers, which suggests weak interaction with the hBN substrate [200]. The promising results obtained for small samples prompted us to perform growth on a large scale.

6.2.1 Wafer scale growth

We repeated the best MOVPE and MBE growth processes on a whole 2" sapphire wafer to prove that our approach is a fully scalable growth method. Fig. 6.6 a) shows a photo of the large-area sample. $MoSe_2$ layer can be seen with the naked eye in a slightly brownish color. The transparent outer ring is a result of using a frame to hold the substrate in the MBE chamber.

To check the uniformity of the $MoSe_2$ layer, we performed a large-area Raman mapping at room temperature. Spectra were measured with the Renishaw inVia spectrometer. The sample was excited by a λ=532 nm laser with a power of 320 μW and a 20x objective (NA 0.4).

For the analysis we chose the more intense out-of-plane A_{1g} peak. The map presented in fig. 6.6 b) indicates a uniform coverage of the wafer with the $MoSe_2$ layer. The energy of the Raman signal is also a powerful tool in determining the thickness of the material. According to previous reports, the out-of-plane mode redshifts while the in-plane mode blueshifts with a decreasing number of layers [108]. Fig. 6.6 c) shows a typical Raman spectrum collected in a random place of the sample. The observed Raman peak positions correspond to the appearance of a single layer of $MoSe_2$. Fig. 6.6 d) depicts the statistical analysis of the A_{1g} peak position on the whole wafer. The standard deviation from the mean value of the energy of the peak ($E_{A_{1g}}$=241.06 cm^{-1}) is small ($\sigma_{A_{1g}}$=0.85 cm^{-1}) confirming the formation of mostly $MoSe_2$ monolayer.

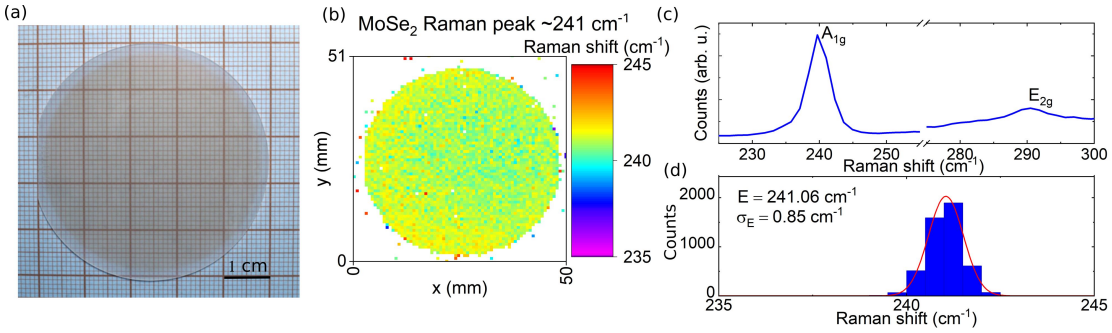

Figure 6.6: a) A photo of 2" sapphire wafer with MOVPE grown hBN and MBE grown $MoSe_2$. Due to the interference, the $MoSe_2$ layer is visible with the naked eye in a brownish color. b) The result of Raman mapping (peak A_{1g}) of the whole area of the sample. The material's coverage is uniform throughout the whole wafer. c) The recorded Raman signal shows characteristic $MoSe_2$ peaks: A_{1g} at $\sim$241 cm^{-1} and a less intense E_{2g} at $\sim$291 cm^{-1}. d) Statistical analysis of the Raman signal (peak A_{1g}) shows a small dispersion of the peak position, proving a good homogeneity of the sample and the formation of monolayer material.

Photoluminescence spectra can also serve as a precise indicator of the thickness of $MoSe_2$. In the monolayer limit, there are no longer any interlayer interactions, resulting in the change of the bandgap from indirect to direct [239]. At room temperature, the PL spectrum consists of one broad feature corresponding to the neutral exciton A. For a monolayer, the energy of

the peak is centered at ∼1.57 eV, while for a bilayer the peak is centered at ∼1.54 eV [108].

Fig. 6.7 shows the result of PL mapping of the whole wafer. Measurements were done using the Renishaw InVia spectrometer, and λ=633 nm laser illumination with 550 μW laser power and a 20x objective (NA 0.4). Three graphs present the parameters of the X_A^0 peak extracted from fitting a Lorentz profile to each of the gathered spectra.

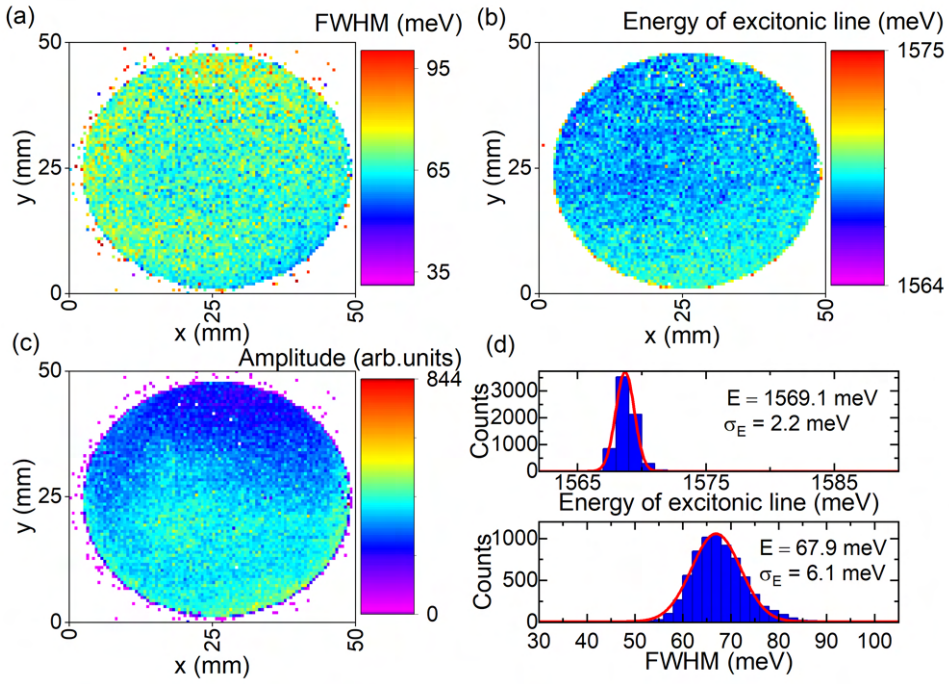

Figure 6.7: Results of the room-temperature PL mapping of the whole wafer. X_A^0 peak parameters are extracted from fitting a Lorentzian profile to the data: a) width, b) energy, c) amplitude of the excitonic peak. d) Histograms show a small standard deviation of the analyzed parameters.

All three plots show a small variation of the analyzed parameters. The peak width with a mean value of (68±6) meV is relatively low for the room-temperature spectra [200]. The mean energy of the excitonic line is (1569.1±2.2) meV, which corresponds to the previously observed value for a single-layer $MoSe_2$ [108]. Another important factor in determining the

thickness of TMD layers is the intensity of the observed excitonic peaks. For monolayers, the signal can be even more than 20 times more intense than for a bilayer [108]. PL mapping shows a rather uniform distribution of the excitonic peak intensity, indicating that the monolayer is present in all parts of the sample.

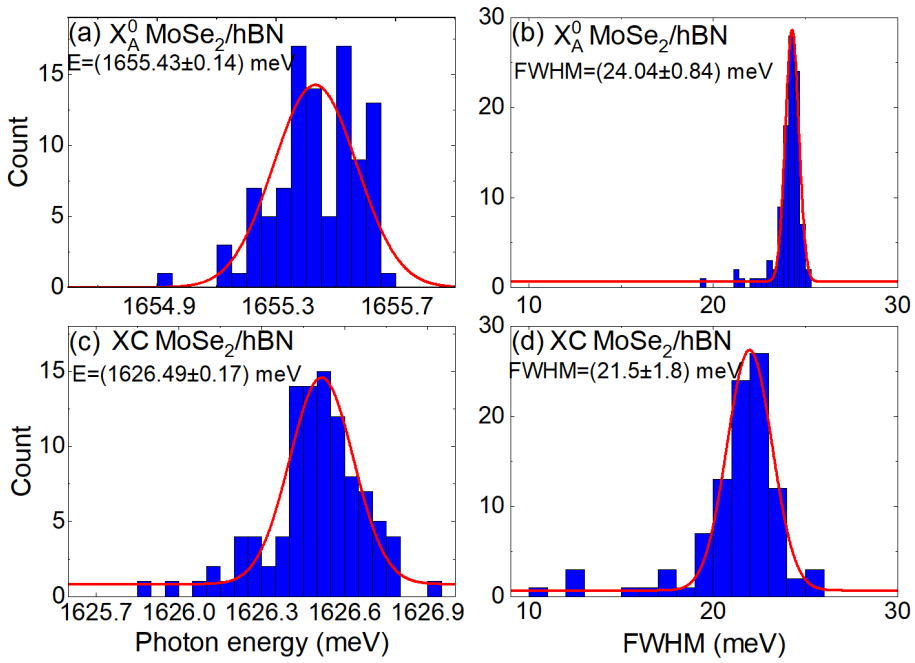

Figure 6.8: Statistical analysis for low-temperature (5 K) PL spectra measured along a 1 cm line. The histograms show the distribution of excitonic peak a,c) energies and b,d) widths extracted from fitting Lorentzian profiles to the signals originating from neutral (X_A^0) and charged exciton (XC) in $MoSe_2$.

This optical, large-scale observation considering a homogeneous intensity as well as a small spread of the exciton peak energy, together with nano-scale TEM characterization provides an insight into the structure of the fabricated structure, indicating the formation of mostly monolayer material on the whole wafer.

To further probe the optical quality and uniformity of the samples, we performed low-

temperature (5 K) PL mapping. Due to the limited size of the cryostat window, we measured 100 spectra equidistant along a straight, 1 cm long line. The spectra were gathered with the HORIBA T64000 system, with 532 nm cw laser excitation. A sum of two Lorentzian profiles was fitted to the collected spectra. A statistical analysis of parameters for X_A^0 and XC is presented in fig. 6.8.

The obtained results indicate a high homogeneity of the samples. For the neutral exciton, we extracted the mean energy of (1655.43 $\pm$ 0.14) meV with the mean FWHM of (24.04 $\pm$ 0.84) meV, while the mean energy for trion was (1626.49 $\pm$ 0.17) meV with FWHM of (21.5 $\pm$ 1.8) meV.

The performed optimization leads to the conclusion, that the best optical quality of the samples is obtained for the thinnest hBN as-grown layers. This observation leads to yet another consideration – is the thickness of the hBN layer a key parameter, or do wrinkles significantly influence the $MoSe_2$ growth? For the thinnest hBN samples, the wrinkles are the least visible, while for thicker hBN layers, the wrinkles protrude substantially. In the next section, we explore the $MoSe_2$ quality grown on the transferred wrinkle-free hBN layers.

6.3 MBE growth on transferred MOVPE hBN

6.3.1 Sample morphology

The heteroepitaxial growth presented in the last section constituted the starting point for further optimization of the process. Now, we wanted to assess whether the wet transfer described in the section 5.2.2 can improve the quality of the grown layers. Undoubtedly, this process removes the micro-wrinkle mesh, which should strongly influence the growth process. While in the last section, we focused on determining the influence of hBN spacer thickness on the quality of $MoSe_2$, in this part we put emphasis on the influence of hBN

morphology on the subsequent heteroepitaxial growth.

For this part of the work, we decided to compare our results with the $MoSe_2$ grown by MBE on the highest quality mechanically exfoliated flakes, obtained from the crystals from the laboratory of Takashi Taniguchi and Kenji Watanabe.

Thanks to the constant improvement of the MOVPE growth of hBN samples by dr Aleksandra Dąbrowska, we were able to use even better quality layers for this study. More optimized growth schemes resulted in improved interface quality and crystallinity. We have chosen three representative hBN layers for further heteroepitaxial growth. Encouraged by the previous promising outcomes with thin material, we selected samples hBN5 and hBN6 grown by a CFG mode, both around 2 nm thick. Sample hBN5 was additionally annealed at 1400°C in a nitrogen atmosphere. This procedure was proven useful in flattening the obtained layers [210].

Additionally, we have chosen one thicker sample hBN4 (thickness: ∼16 nm) fabricated by a combined growth mode (CGM), which possessed a well-ordered crystallographic structure. Table 6.2 shows aggregate MOVPE growth data for samples hBN4-6.

Table 6.2: MOVPE growth parameters of hBN samples used as a substrate for heteroepitaxial growth of $MoSe_2$, after the wet transfer to Si/SiO_2.

MOVPE		
sample	**thickness**	**growth mode**
hBN4 (G141, G142)	16 nm	CGM
hBN5 (G149)	2 nm	CFG + N_2 annealing
hBN6 (G153)	2 nm	CFG

Fig. 6.9 shows a comparison between the morphologies of samples hBN4 and hBN5 probed by SEM imaging. A well-pronounced wrinkle mesh is visible for the thicker hBN layer, while wrinkles are practically not visible in the case of a thin sample. The optimization of MOVPE growth allowed us to drastically reduce the number of 3-dimensional precipitates

appearing on the material surface.

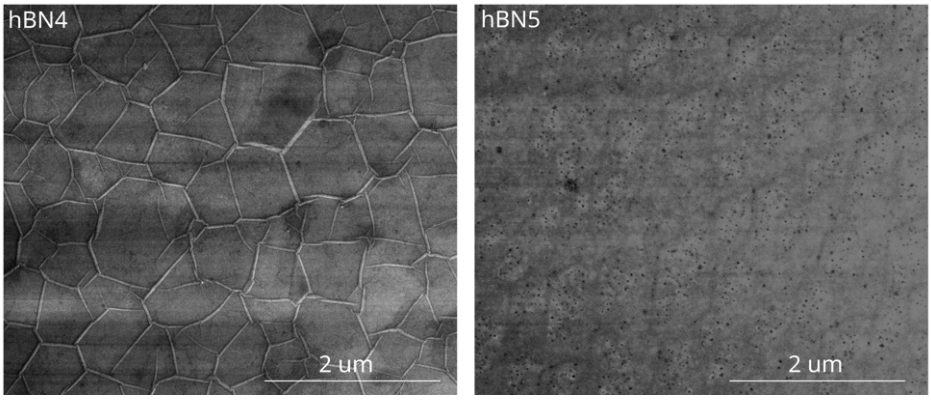

Figure 6.9: SEM images of as-grown samples hBN4 and hBN5. A micro-wrinkle mesh is well-visible for the thicker (∼16 nm) layer hBN4. The development of MOVPE growth parameters allowed to practically eliminate the out-of-plane precipitations.

hBN layers were transferred to a silicon/silicon dioxide substrate using the wet delamination scheme described in detail the section 5.2.2. The thicker sample hBN4 was very easy to transfer, as it detached without any cracks and did not form many wrinkles after the deposition on the new substrate. The transfer of this specific sample is shown in fig. 5.6.

Thinner hBN samples posed a bigger challenge to transfer since the delamination process did not initiate by immersion in water-IPA solution. To overcome this limitation, we attached PDMS frames to the samples [240]. This action allowed to delaminate significant parts of the hBN layers and place them onto the new substrate.

Samples hBN 4-6 were transferred to Si/SiO_2 substrates, and heated for at least 30 min at 150°C. Subsequently, each sample was cut into three pieces. Then, samples were used as substrates for further MBE growth of $MoSe_2$. For every MBE process (MBE D-F), a set of four substrates was used simultaneously to ensure the same growth conditions. The set of four substrates included: one piece of each MOVPE-grown sample (hBN 4-6), as well as a piece of Si/SiO_2 with small, mechanically exfoliated hBN flakes, serving as a reference.

Table 6.3: Growth parameters for MBE processes: D, E and F.

MBE			
Process	D	E	F
Pre-growth annealing temp.	780 °C	780 °C	780 °C
Pre-growth annealing time	To reach 780 °C	To reach 780 °C	2h in 780 °C
Growth temp.	300 °C	300 °C	300 °C
Growth time	2 h	1.5 h	40 min
Post-growth annealing temp.	780 °C	780 °C	780 °C
Post-growth annealing time	3 h	2 h	2 h

Overall, three different MBE processes were performed (MBE D-F) on three sets of samples (hBN 4-6 on Si/SiO_2, and exfoliated hBN on Si/SiO_2).

The starting point was the process MBE D optimized for the best $MoSe_2$ growth on hBN flakes. Then, the deposited amount of source elements was gradually reduced for processes MBE E and MBE F.

Each MBE process followed the same scheme: pre-growth annealing, growth, and post-growth annealing as summarized in the table 6.3.

For processes MBE D and E, the temperature of the substrate was raised to 780 °C and right away cooled to the growth temperature of 300 °C. During the process MBE F, substrates were annealed significantly longer, for 2 hours, to outgas them, and relax the hBN layer. For the subsequent processes, the time of growth was reduced from 2 hours, through 1.5 hours, to 40 minutes. The MBE growths were followed by yet another annealing at 780 °C.

Fig. 6.10 shows a comparison of AFM images of hBN samples as-grown, after the transfer and after MBE processes D-F. Thin as-grown hBN layers (6.10 f,k) manifest a much finer wrinkles mesh as compared to the thicker material (6.10 a). Images collected for hBN layers after the transfer allow to study the morphology of the material itself. The surface of the thick sample hBN4 reminds stacks of triangular terraces, mostly oriented in the same direction. Thinner samples hBN 5 and hBN 6 appear as a torn is some places, slightly uneven layer.

The wet transfer eliminated the micro wrinkles pattern but led to the formation of longer, bigger folds. This behavior, which occurs mainly in thinner samples, can be explained by the wet transfer process. Different parts of a floating layer stick to the new substrate unevenly: at slightly different times and not in a perfectly straightened position, causing the appearance of new wrinkles. Additionally, the direction of the wrinkling corresponds to the direction of pulling out the substrate from the solution. In the future, the process can be automated to ensure uniform substrate pulling at precisely set angle.

AFM images collected after the MBE growth (fig. 6.10 panels c-e, h-j, m-o) show that all hBN layers were covered with additional material. The morphology of the heterostructures is best visible for samples utilizing hBN 4, where $MoSe_2$ flakes overgrow triangular terraces. Images obtained for MBE process D, which used the largest amount of reagents, suggest a significant number of multilayer $MoSe_2$ areas. The reduction of growth time, and consequently the amount of elements used, resulted in a smoother sample morphology (MBE processes E and F), indicating mostly monolayer coverage.

Fig. 6.11 shows a comparison between MBE growth on epitaxial and exfoliated hBN.

Images collected for bulk exfoliated material indicate a smooth and atomically flat surface of the hBN flake, with overgrown $MoSe_2$ islands with sizes up to 70 nm in diameter (Fig. 6.11). As the MBE process D was optimized for the growth on exfoliated hBN, the coverage with $MoSe_2$ is the highest. The height of a single $MoSe_2$ layer calculated from structural models [241] is less than one nanometer, which corresponds well to the height of observed islands. Additionally, mostly in the vicinity of edges, the formation of a second and sometimes third layer of $MoSe_2$ can be seen.

For MBE processes E and F we see a gradual reduction of the $MoSe_2$ coverage of the hBN flake. However, despite the reduction of reagents, the inclusions of two, and more layers are still present. This observation suggests that the flat surface of an exfoliated hBN flake does not

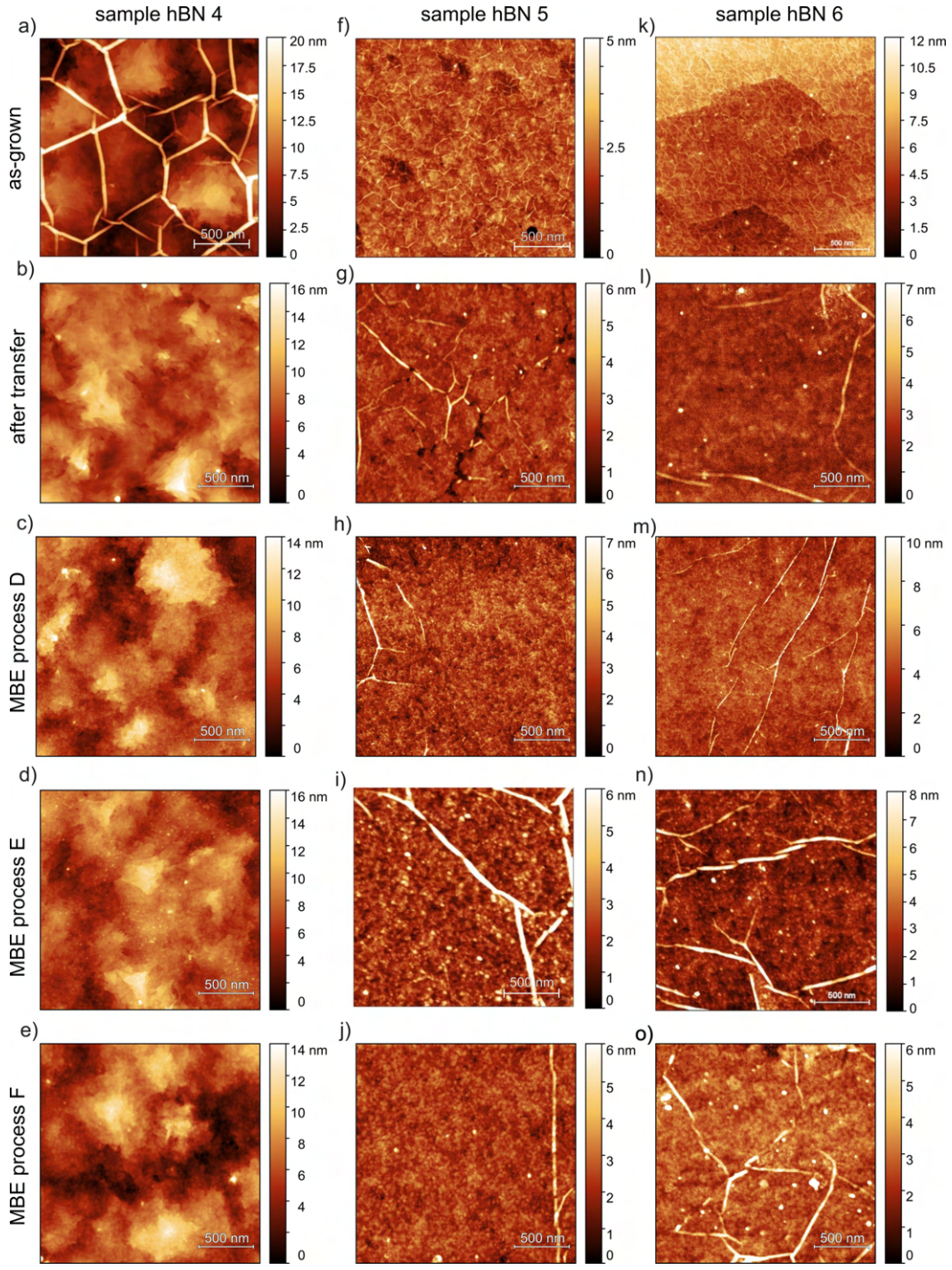

Figure 6.10: AFM images collected for the samples a-e) hBN 4, f-j) hBN 5, k-o) hBN 6, as-grown on the sapphire substrate, after the transfer to Si/SiO_2 substrate, and after MBE growth processes D-F.

provide enough nucleation centers for the initiation of $MoSe_2$ growth. The material starts to grow near the sharp edges, resulting in the unwanted formation of more than one layer, even for the process MBE F using the smallest number of reagents.

According to AFM measurements epitaxial hBN 4 sample has a roughness of ∼2.5 nm, and is made of numerous triangular terraces. Such a morphology creates many nucleation centers for the further growth of other materials. The increased growth on the wrinkles and at the point defects found near the substrate surface was previously observed and documented [242–245]. Our epitaxial hBN provides uniformly spread irregularities, allowing homogeneous growth on the whole area of the sample. AFM images corresponding to subsequent MBE processes (fig. 6.11) indicate that more $MoSe_2$ was deposited than in the case of the growth on exfoliated flakes. Process MBE D using the largest amount of source elements resulted in epitaxial hBN terraces completely covered with material suggesting the appearance of more than one layer. Process MBE F which used the smallest amount of reagents resulted in seemingly uniform coverage with almost touching $MoSe_2$ flakes without any significant contribution of multilayers.

A large number of edges and irregularities found in the epitaxial hBN samples promote the uniform growth of other materials. Additionally, it uses a smaller amount of resources, making it beneficial for any scalable real-world applications.

6.3.2 Optical properties of the $MoSe_2$/hBN heterostructures

We performed low-temperature (5 K) spectroscopy studies to determine the optical quality of fabricated heterostructures. Fig. 6.12 presents the PL spectra collected for epitaxial hBN samples 4-6 and exfoliated flakes, after MBE growth processes D-F.

As described in the previous section 6.2, for high-quality $MoSe_2$ excitonic peaks are narrow and well-resolved at cryogenic temperatures. In monolayers the lower energy peak ∼1.63 eV

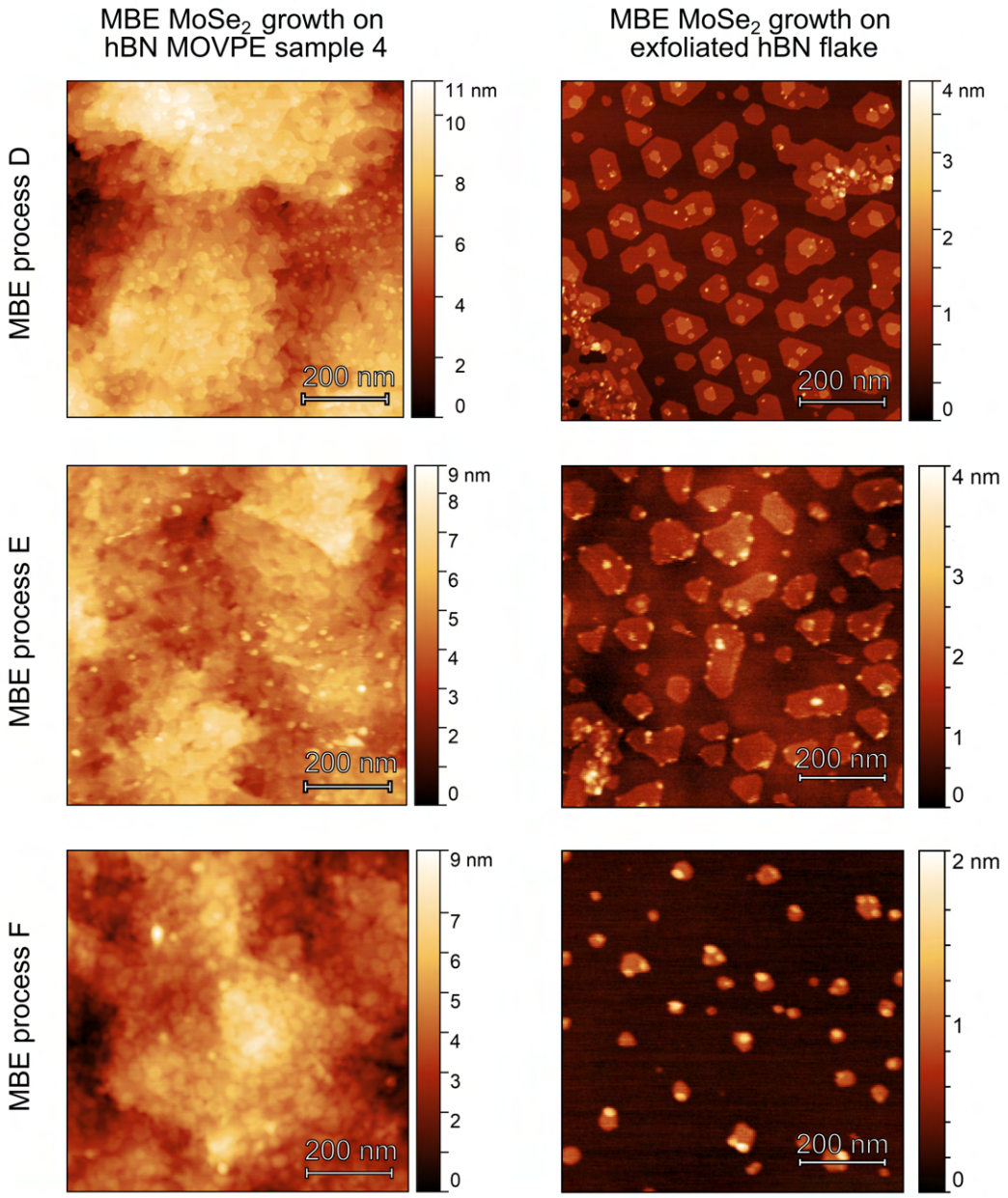

Figure 6.11: AFM images comparing the effect of different MBE processes (D-E) on the morphology of samples: epitaxial hBN 4 and exfoliated hBN flakes. Many sharp edges and terraces found in epitaxial hBN provide nucleation centers for easy and uniform growth of $MoSe_2$. On the contrary, atomically flat mechanically exfoliated hBN flakes do not promote the growth resulting in smaller $MoSe_2$ coverage with many multilayer inclusions.

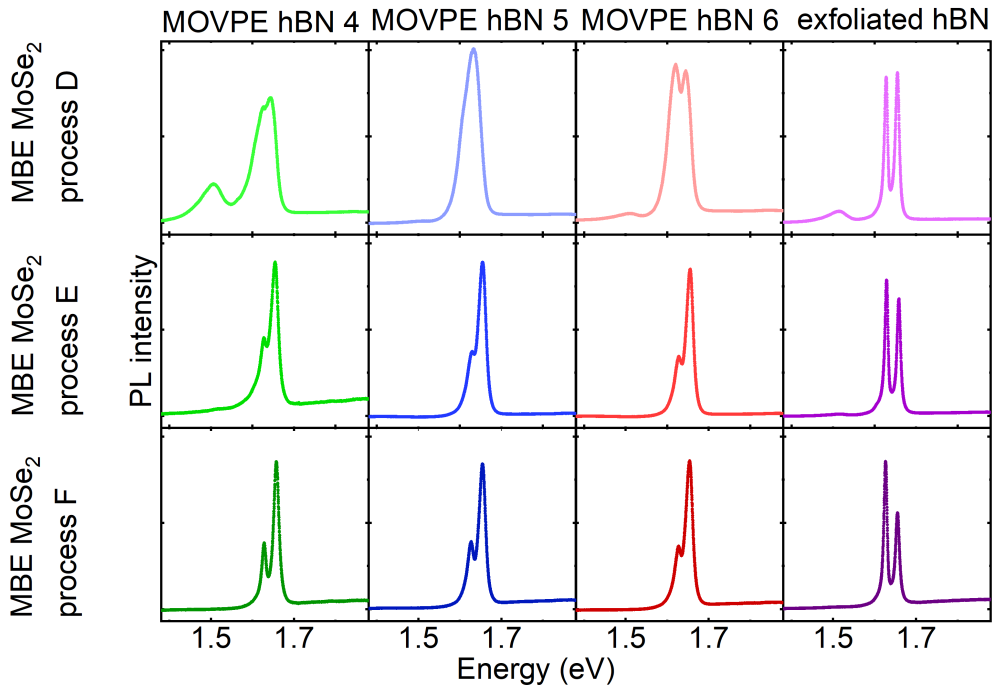

Figure 6.12: A comparison between PL spectra gathered at 5 K, for samples using hBN samples 4-6, as well as exfoliated hBN flakes as substrates for further MBE growth of $MoSe_2$. Subsequent MBE processes (D-F) use gradually smaller amount of source elements.

corresponds to the charged exciton, while the higher energy peak ∼1.66 eV corresponds to a neutral exciton [200] (section 4.1.2). Additionally, the intensity ratio between the excitonic peaks depends on the carrier concentration in the material [109].

Unsurprisingly, MBE process D optimized for and performed on exfoliated hBN flakes, results in narrow and resolved excitonic peaks with slightly dominating neutral exciton contribution. For processes MBE E and F using a smaller amount of reagents, the intensity ratio between a trion and exciton A shifts, resulting in a higher charged exciton intensity. The energy and width of the excitonic lines do not change significantly, suggesting a high quality of the obtained monolayers. Additionally, we observe a broad feature at ∼1.5 eV which

corresponds to the appearance of a bilayer material [108].

MBE process D performed in epitaxial hBN results in broader excitonic features. A slight separation of the lines is observed only for samples hBN 4 and hBN 6. Furthermore, a broad peak indicating the occurrence of a bilayer $MoSe_2$ is visible for all of the epitaxial samples. The optical quality of the studied heterostructures significantly improves with lowering the amount of used source materials. The best results are obtained for the process MBE F. All epitaxial samples manifest the separation and narrowing of the excitonic lines. For all of the epitaxial heterostructures the contribution of the neutral exciton dominates over the trion.

According to the literature, mechanically exfoliated $MoSe_2$ monolayers usually manifest n-type doping [246] resulting in a higher intensity of a trion-related feature [200, 234, 246]. Our results for epitaxial hBN samples and MBE process D on exfoliated flakes indicate an inverse relationship. Other works point to several possible explanations for this phenomenon. The $MoSe_2$ charge state can be influenced by point defects or charge transfer from the substrate [229, 238, 246, 247]. Apart from that, applying voltage and changing the laser excitation power [200, 246] can be used to influence the neutral to charged exciton intensity ratio.

Reports show [229], that the thickness of the hBN spacer greatly influences the properties of $MoSe_2$. Thin hBN barrier allows charge to tunnel from the impurities of Si/SiO_2 substrate influencing the carrier concentration of the monolayer. In our experiment, we employed both thick (hBN 4) and thin (hBN 5 and 6) epitaxial samples and did not observe changes in charged to neutral exciton intensity ratio between them. However, looking at the morphology images of epitaxial hBN samples, as well as observing rich defect-related light emission (further described in chapter 7), we anticipate MOVPE hBN to have the biggest influence on the charge state of the $MoSe_2$ layer grown on top of it. Since epitaxial hBN possesses many edges, irregularities, and structure defects, we suspect that such features in hBN can lead to changes in the doping of the $MoSe_2$ monolayer.

Fig. 6.13 shows a comparison between low-temperature PL spectra collected for samples grown in MBE process F on epitaxial hBN 4 and on exfoliated flakes.

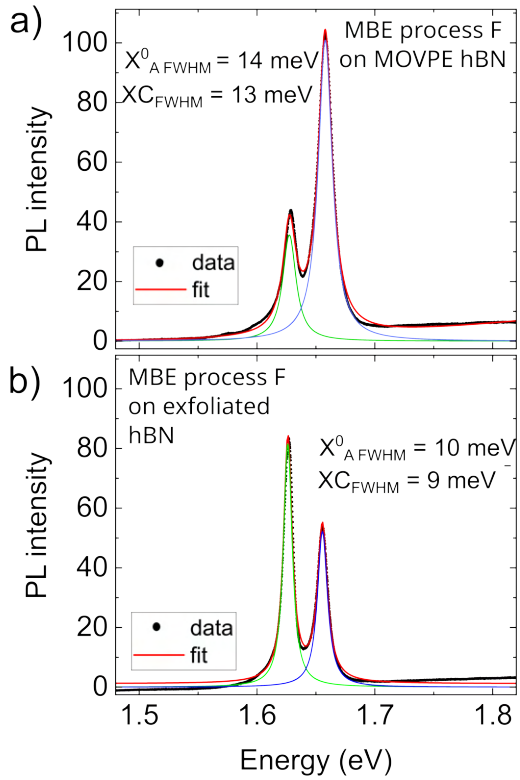

Figure 6.13: PL spectra collected for MBE process F performed on a) epitaxial sample hBN 4, b) mechanically exfoliated hBN flake.

Similar to the previous section, we fitted a sum of two Lorentzian profiles to the data to extract the exact peak energies and widths. We obtained widths as narrow as 14 meV and 13 meV for X_A^0 and XC, respectively, in the case of MBE growth on epitaxial hBN, and 10 meV and 9 meV for X_A^0 and XC, respectively, in the case of MBE growth on exfoliated hBN. The results are comparable, yet still inferior to the best points found in fully exfoliated samples or best MBE growths on exfoliated hBN flakes [228].

In AFM imaging (fig. 6.10 and fig. 6.11) we identified some parts of the $MoSe_2$ flakes

as multilayer inclusions. Optical spectroscopy results agree with this observation. Fig. 6.14 shows a zoom into the PL spectra at the energy range corresponding to the $MoSe_2$ bilayer signal (∼1.5 eV) with fitted peak areas A (arb. units).

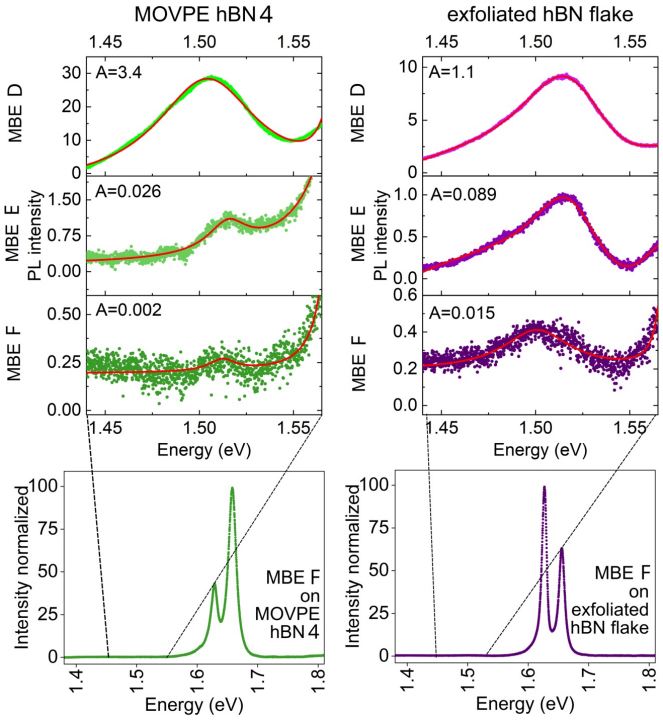

Figure 6.14: Low-temperature PL spectra collected for MBE processes D-F performed on samples hBN 4 and on exfoliated hBN flakes. Zoom-ins show the spectral region where the feature corresponding to the $MoSe_2$ bilayer appears. The contribution of the bilayer decreases with the decreasing amount of source elements used in the MBE growth.

For MBE process D we observe a significant contribution of a bilayer related peak. This contribution is ∼3 times larger in the case of growth on epitaxial hBN, suggesting a large amount of overgrown $MoSe_2$. The reduction of source elements for the MBE processes E and F significantly lowers the bilayer contribution. A much larger share of bilayer $MoSe_2$ is formed in the case of growth on exfoliated hBN flakes, which agrees with the morphology imaging. Flat surfaces of hBN flakes do not promote the MBE growth. Mostly rough edges of already fabricated $MoSe_2$ layers serve as new nucleation centers.

In the case of growth on 'rough' epitaxial hBN layers, the morphology irregularities are uniformly spread across the sample, constituting many nucleation centers. The bilayer-related peak area recorded for the MBE growth F is almost negligible, suggesting mainly $MoSe_2$ monolayer coverage.

To further characterize the quality of the samples, we performed low-temperature photoluminescence mapping of samples using epitaxial hBN 4 and exfoliated hBN flakes as a substrate for further MBE growth. The samples were mapped using a 532 nm laser in 50x50 μm areas. We fitted the sum of Lorentzian profiles to extract excitonic positions and linewidths presented in fig. 6.15 (columns 1 and 2).

Histograms presented in the third column in fig. 6.15 and table 6.4 show the results of the performed statistical analysis.

	$MoSe_2$ growth on MOVPE hBN	$MoSe_2$ growth on exfoliated hBN
X_A^0 peak position (meV)	1655.94 ± 0.13	1657.18 ± 0.74
XC peak position (meV)	1627.17 ± 0.24	1630.59 ± 0.75
X_A^0 peak width (meV)	15.0 ± 0.4	10.8 ± 1.2
XC peak width (meV)	11.2 ± 0.7	7.0 ± 0.5

Table 6.4: A summary of statistical analysis of the excitonic peaks properties extracted from the PL mapping of $MoSe_2$ grown on MOVPE and exfoliated hBN.

Mean linewidths obtained for the growth on exfoliated flakes are as expected smaller than in the case of growth on epitaxial layers. However, the spread of the excitonic peaks positions and widths is significantly smaller for the $MoSe_2$ grown on epitaxial hBN.

Literature reports point at the mechanical exfoliation process as a reason for the large variance in $MoSe_2$ properties. The deterministic encapsulation in hBN flakes can lead to strain distribution resulting in the excitonic peaks' variations of $\sim$1.5 meV [236], agreeing with our findings. Additionally, the use of tapes during the exfoliation can result in the polymer

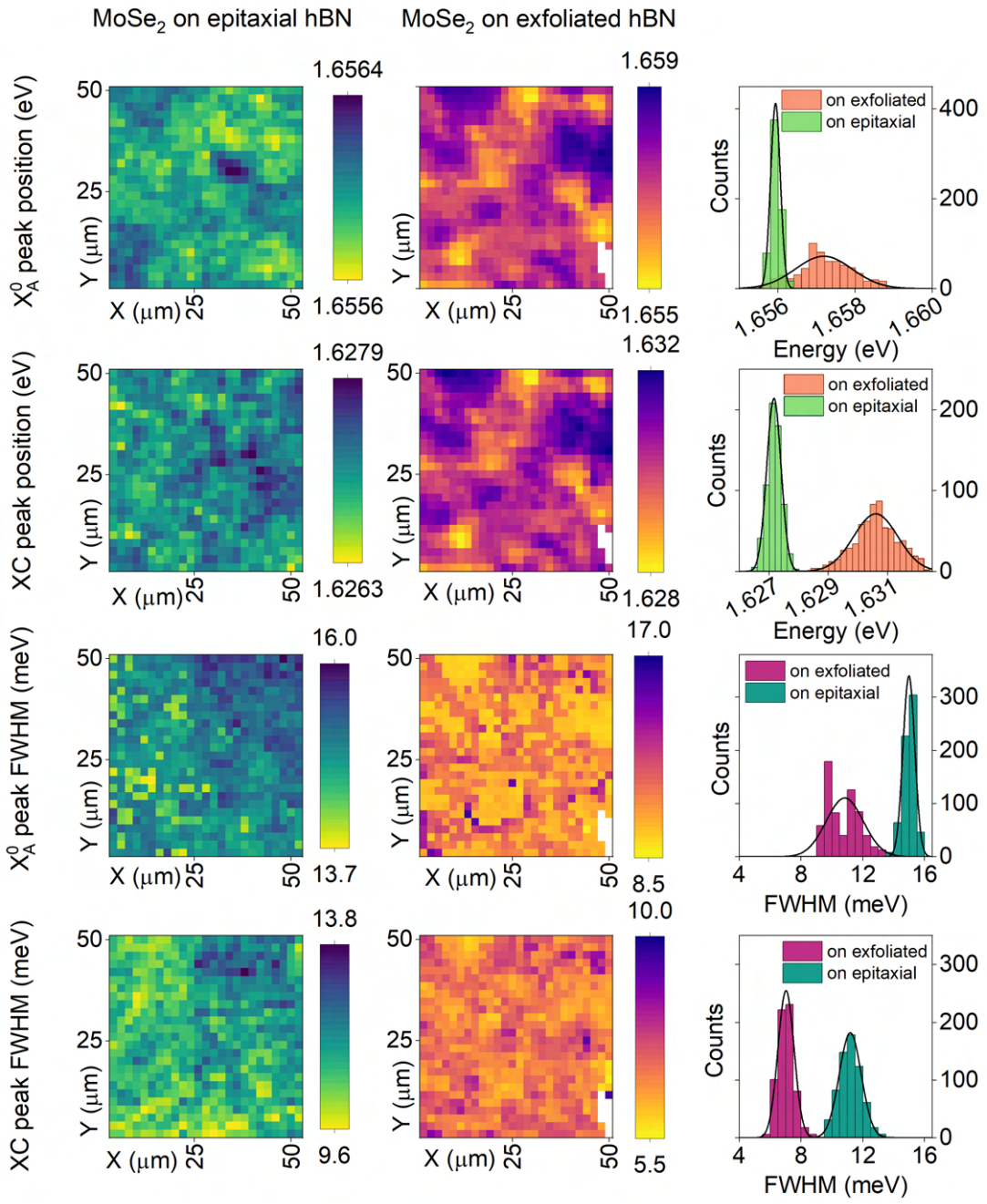

Figure 6.15: PL maps showing the spatial distribution of exciton-related peaks for $MoSe_2$ grown on epitaxial hBN (1st column) and exfoliated hBN (2nd column). The 3rd column depicts histograms presenting the spread of the position and widths of the excitonic lines.

residues on the flakes, locally influencing the properties of the grown $MoSe_2$ layer [248].

Our heteroepitaxial approach excludes the use of any polymer, leaving a clean interface to perform further growths. Our results showing a great uniformity of the fabricated $MoSe_2$ also suggest, that the large-area hBN layers are relaxed, even after the wet transfer.

On exfoliated flakes, researchers typically report spectra only for the best spots, which are much narrower (down to ∼2-3 meV for $MoSe_2$ monolayers) [232]. However, such spectra are not representative of the whole flake, mostly because of the strain and fabrication residues like bubbles or small polymer pieces [236]. $MoSe_2$ samples grown by our heteroepitaxial method are characterized by broader excitonic lines (∼11-15 meV), however, manifest much better homogeneity. Photoluminescence mapping on a micro, as well as macro scale, shows that the optical properties are uniform in our epitaxial samples. Such high homogeneity, as well as the possibility of performing growths repetitively in the same conditions, renders our approach as a viable solution for optoelectronic applications.

Electrical characterization As shown in the previous reports [200], applying a voltage to the $MoSe_2$ layer allows to electrically control the charge state of the structure. The tunability from positive through neutral to negative exciton charge state is manifested in the gate voltage-dependent photoluminescence measurement. While changing the applied electric field, the intensity ratio between charged and neutral excitons changes, indicating electrostatic doping in the $MoSe_2$ layer [200]. The described electrical control is important for the optoelectronic applications, as well as from a fundamental research perspective [249, 250]. However, the electrostatic tunability was demonstrated only for high-quality, micro-scale devices. In this work, we present the electrical control of the exciton charge state on our large-area material, further proving its quality and usability in future applications.

The electrical control of the charge state is usually demonstrated in the field effect tran-

sistor structures [200]. In such devices, the back gating is achieved by applying the voltage to a conductive substrate (like Si) separated by a thin layer of dielectric (like SiO_2) from the active $MoSe_2$ layer. Additionally, electrical contacts are fabricated lithographically on top of the structure.

In our case, gating of the as-grown hBN/$MoSe_2$ layers was experimentally not feasible, due to 430 μm thick sapphire wafers used as a substrate, efficiently screening any back-gate. However, $MoSe_2$ samples grown on epitaxial hBN layers transferred to Si/SiO_2 allowed us to back-gate the structure and perform electrical characterization.

We tested a simplistic approach for our samples and used silver paste to create top and back contacts, as schematically presented in fig. 6.16 a). The conductive p-doped silicon served as a gate, while a 90 nm thick SiO_2 layer was used as a dielectric. The sample was glued using silver paste to the non-conductive sapphire and then glued on the cold finger of the cryostat to avoid a short circuit. We performed low-temperature PL studies by illuminating the sample with a lateral distance of $\sim$100 μm from the top contact. Applied gate voltages ranged from -30 V to +30 V. We avoided applying higher voltages to prevent the dielectric layer breakdown of the SiO_2 layer.

Fig. 6.16 b) shows photoluminescence spectra collected at the same spot on the sample, but with three different gate voltages applied. For 30 V, the neutral exciton contribution is only slightly higher than the charged exciton contribution (the intensity ratio equals: $I_{X_A^0}/I_{XC} = 1.42$). The situation changes with decreasing gate voltage. At -30 V, we observe a significant dominance of the neutral exciton intensity (the intensity ratio equals: $I_{X_A^0}/I_{XC} = 2.81$).

Fig. 6.16 c) presents the photoluminescence intensity map for data collected at -2 V – 30 V gate voltage range. We observe a gradual change of the neutral to charged exciton intensity ratio, further proving the electric tunability of the charge states in our samples. Fig. 6.16 d)

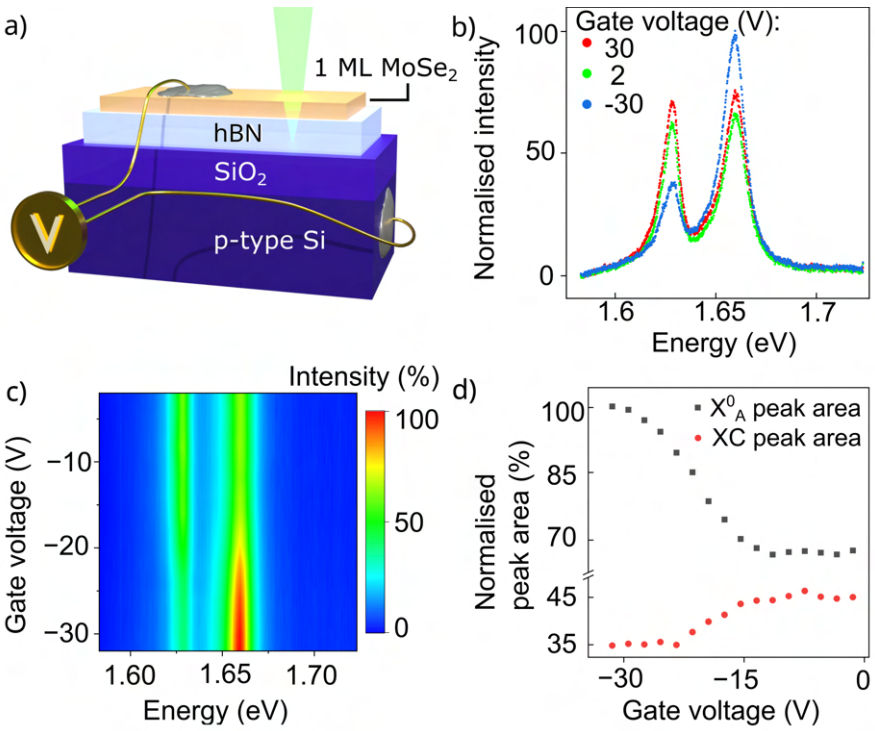

Figure 6.16: a) Schematic illustration of our large-area hBN/$MoSe_2$ heterostructure used for the electro-optical characterization. b) A comparison between low-temperature PL spectra recorded for various gate voltages. c) PL map as a function of applied voltage (spectra were normalized to the maximum value obtained for -30 V). d) Peak areas extracted for the charged and neutral excitons at different voltages. The highest variability is observed for negative voltages.

shows the neutral and charged exciton peak areas extracted from fitting Lorentzian profiles to the data, as a function of the gate voltage. The difference between peak intensities is the biggest for the highest applied gate voltage, and decreases as it approaches zero.

The results show, that the excitonic species in large-area epitaxial samples can be electrically controlled. Additionally, a simplistic electrical contacts fabrication scheme using easily available silver paste, was enough to demonstrate the tunability in the structure. No need to use photolithography to gate the samples is beneficial, as it shortens the time needed for each structure characterization, and is a cleaner fabrication method, not leaving any resist residues on the material.

While other works [200, 251, 252] present such electrical control on a microscale with exfoliated material, our approach allows to gate large-area, centimeter-sized samples. Tuning of the optoelectrical properties of various TMDs is crucial for their future use in real-world devices.

6.3.3 Conclusions

In this chapter, we presented a combined epitaxial growth method to fabricate high-quality monolayers of molybdenum diselenide. We have taken two main approaches: MBE growth on as-grown and transferred MOVPE hBN. We optimized epitaxial growth processes to obtain high-optical-quality samples, as manifested by narrow and resolved excitonic lines in PL measurements at low-temperatures.

In the case of $MoSe_2$ growth on as-grown hBN layers, the key parameter was the thickness of the hBN spacer. Utilizing thinner ($\sim$1.5 nm) samples allowed to obtain the best results. Such an approach is well-suited to a scalable production, as it does not require additional transfer steps: the wafer can be transported directly between MOVPE and MBE systems.

However, even better optical properties of the samples were achieved for the $MoSe_2$ growth on transferred hBN layers. In this scheme, the crystalline quality of the hBN layer became a key factor that affected the quality of the entire structure. The transfer step allowed us to remove the micro wrinkles that form during a cool-down after the growth process of the hBN layers. The lack of wrinkles resulted in better morphology and positively influenced subsequent MBE growth. The irregularities and edges that are characteristic of the epitaxial hBN samples promoted $MoSe_2$ nucleation and ensured uniform coverage. Additionally, transferring the hBN layer onto a Si/SiO_2 substrate enabled the electrical gating of the structure. By probing gate-voltage-dependent photoluminescence spectra, we demonstrate the electrical control of the charge carrier concentration in $MoSe_2$ grown on large-area hBN.

We observed a significant improvement in the optical quality of the $MoSe_2$ layers grown on epitaxial hBN samples as large as 2". The optimization of such structures is a complicated problem dependent on various parameters like MOVPE and MBE growth schemes, and substrate treatment between the epitaxial processes. Thanks to the systematic characterization of the samples and feedback provided, we managed to optimize the epitaxial processes towards the fabrication of high-optical-quality samples. While many parameters can be further improved, the proposed heteroepitaxial method brings us closer to developing reproducible and scalable fabrication schemes that are necessary for industrial applications.

It is worth highlighting that the presented combined growth scheme can also be implemented to other 2D materials, not only $MoSe_2$, but also other TMDs and other classes of van der Waals crystals, like 2D magnets. Further improvement of the large-area hBN growth control, resulting in higher layer quality, gives hope that epitaxial hBN can become a universal template for future 2D materials production. Overcoming the scalability limitation is crucial for developing new generations of devices such as light sources, photodetectors, sensors, or building blocks for quantum technologies.

Some of the presented results were published in two articles in high-impact scientific journals [253, 254].

[This page intentionally left blank]

7

hBN/2D magnet heterostructures

7.1 Introduction

In this chapter, we undertake the topic of hBN properties and applications on the nanoscale. As shown in the previous chapter, our epitaxial material can significantly improve the optical quality of other 2D crystals and can be integrated into large-area heterostructures. However, hBN being a wide bandgap semiconductor is itself an interesting platform for studying basic physical phenomena. Color centers in hBN are an intensively developing research direction

aimed at creating two-dimensional quantum platforms like single photon emitters and nanosensors. In this work, we decided to study the interaction between optically active defects in hBN and an intriguing class of 2D materials – nanomagnets.

In the beginning, we used chromium trihalides received thanks to the courtesy of Prof. Jacek Jasiński from the University of Louisville to build our structures. Crystals of CrI_3, $CrBr_3$, and $CrCl_3$ seemed like a perfect fit for our experiments as each of them offered different magnetic ordering and spin arrangements in a few-layer limit. Unfortunately, the crystals were not stable enough for our long-term experimental needs and were not compatible with our wet exfoliation technique. Hence, we switched to another 2D magnet: chromium thiophosphate. We performed optical characterization of the structures in different conditions: with varying temperature, applied voltage, and in external magnetic field.

Apart from confirming the structural properties predicted in the literature, we obtained two intriguing results indicating the presence of interaction between a defect in hBN and the magnetic state of $CrPS_4$. In temperature-dependent experiments, we found a correlation between the color center emission energy and an antiferromagnetic-paramagnetic phase transition in the underlying nanomagnet. In the external magnetic field-dependent measurements, we found that the defect emission energy and intensity drastically change upon the spin-flop transition in $CrPS_4$.

7.2 Sample preparation

For this study, we fabricated three main types of samples consisting of:

- mechanically exfoliated, commercially available hBN and CrX_3 – for initial characterization;
- epitaxial hBN and CrX_3;

- epitaxial hBN and $CrPS_4$.

For the first type of samples, we performed a standard mechanical exfoliation as described in chapter 5.2.1.

For the samples containing epitaxial hBN, we used the wet delamination technique described in chapter 5.2.2 to transfer chosen hBN layers onto the silicon/silicon dioxide substrate. After this step, we heated the samples on a hotplate at $\sim$150°C for at least 30 min to evaporate the remaining water. Substrates prepared in this manner could be stored in a protective atmosphere for a few weeks and reheated for the next fabrication steps. Fig. 7.1 a,b) shows SEM images of a $\sim$16 nm thick epitaxial hBN layer before and after the transfer. Such a step helps to eliminate the wrinkle mesh present on the sample after the MOVPE growth process.

During this study, we optimized the exfoliation process of nanomagnets. The crystals were stored in a protective atmosphere and taken out into the air only for exfoliation. Four exfoliation tapes with different viscosities were tested. The *Microworld F07* tape with a medium viscosity (70/135 g/25 mm) proved to be the best for obtaining thin flakes of regular shapes. During transfer onto SiO_2/hBN substrates, a problem was encountered: transfer directly from the exfoliation tape turned out to be ineffective because the tape also peeled off the hBN layer from the substrate. In order to solve the problem, we used the flake transfer method using a gel film made of PDMS. In this case, three types of gel films from *GelPack* were tested, the best of which was *X4*, which provided the transfer of the largest number of flakes while avoiding the peeling off of the hBN layer. The best quality of transferred flakes was achieved for the samples for which we left the applied PDMS film overnight before removing it.

Quickly after removing the PDMS, we again heated the samples, this time however at a

lower temperature of <100°C to ensure the safety of the 2D magnets flakes. As the last step, we performed the wet exfoliation and transfer of hBN onto the prepared samples followed by yet another heating treatment. Fig. 7.1 c) depicts the schematic structure of a heterostructure containing epitaxial hBN and a 2D magnet, while fig. 7.1 d-f) shows the optical images of the subsequent steps of sample fabrication.

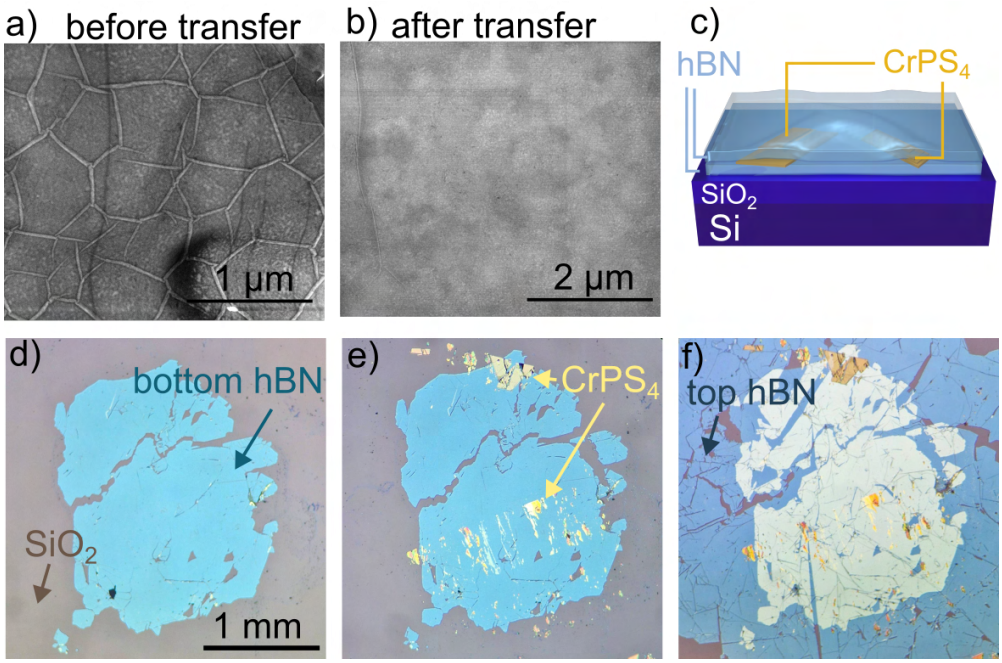

Figure 7.1: a) SEM image of ∼16 nm thick hBN sample on a sapphire substrate. b) SEM image of ∼16 nm thick hBN sample after wet delamination and transfer onto Si/SiO_2 substrate. After this process, the characteristic post-growth wrinkles are smoothed out. c) Schematic illustration of a cross-section of samples. d-f) Optical images showing the step-by-step assembly process of a large-area hBN/$CrPS_4$/hBN heterostructure.

Interestingly, we did not observe significant differences in the adhesion of flakes of 2D magnets to the Si/SiO_2 substrate and epitaxial hBN layer, so we could cover a large area of the sample with flakes of different thicknesses and sizes. Such samples provide a great platform for studying various material arrangements at once. Measurements are not limited to a single specific flake like in the case of mechanically exfoliated structures.

The presented sample fabrication method required putting the structure with exfoliated 2D magnets into the deionized water. Even though immersion in liquid did not detach magnetic flakes from the substrate, and did not dissolve them, it was not beneficial for their durability. After a few tries, we decided to proceed only with chromium bromide from the chromium trihalides family, as other compounds visibly degraded right after the fabrication. Unfortunately, after performing a series of low-temperature measurements, samples consisting of $CrBr_3$ were also destroyed and unusable, leading us to switch to $CrPS_4$, which proved to be much more stable.

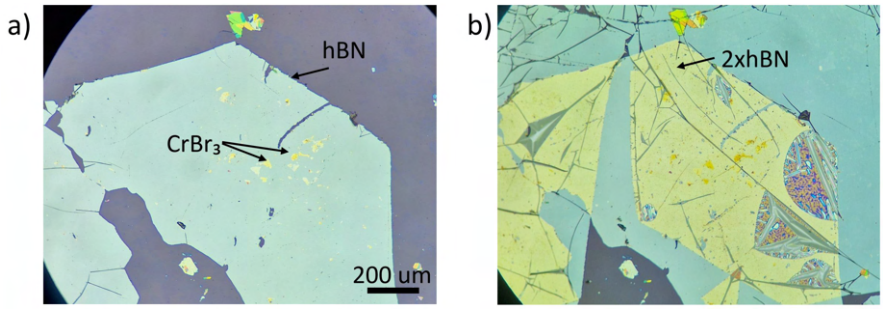

Figure 7.2: a) Optical image of a delaminated hBN layer deposited on a Si/SiO_2 substrate with exfoliated flakes of magnetic $CrBr_3$, b) image of the same fragment of the sample after covering the structure with another hBN layer.

As presented in fig.7.2 applying another hBN layer generates wrinkles and bubbles up to 400 μm in diameter, filled most probably with residual water used for delamination. When activated, for example by laser irradiation, the residual water could interact with a 2D magnet and dissolve it. As shown in the fig. 7.3, even weak irradiation lead to irreversible damage to the magnetic flake. According to literature, $CrBr_3$ is soluble in hot water and forms $CrBr_3(H_2O)_3$ [255].

Keeping the samples in the desiccator between the measurements greatly improved their lifetimes. Fig.7.4 shows a comparison between the appearance of $CrBr_3$ flakes right after exfoliation (panel a), and after two months from the fabrication, while being kept in a desiccator

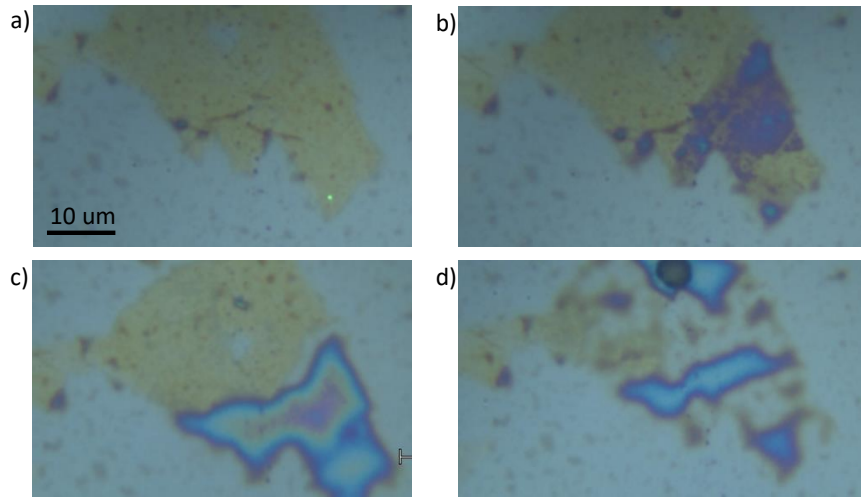

Figure 7.3: Optical microscope photograph of a $CrBr_3$ flake encapsulated in hBN, a) just after sample preparation, b) just after irradiation with a green laser (wavelength 532 nm), c) 5 minutes after irradiation, d) 12 hours after irradiation.

(panel b). At first glance the flake looks similar, but a closer look reveals slowly progressing deterioration of the material at the edges, wrinkles, and around small bubbles. In these regions is the largest accumulation of water residues responsible for the destruction of flakes.

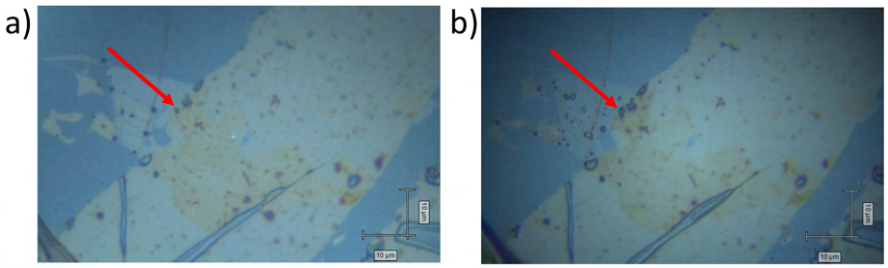

Figure 7.4: Optical microscope photo of the encapsulated $CrBr_3$ flake a) just after encapsulation b) after two months in a desiccator. Even though the damages are not prominent, it is visible that small bubbles, likely filled with residual water act as precursors of deterioration. The red arrow points to the area of the flake which deteriorated over time.

DEGRADATION DUE TO FLATTENING Deterioration of the magnetic flakes was not the only reason behind changes in the samples. After long-term studies of the structures, we

found that numerous pumping cycles and keeping the samples in vacuum for a prolonged period of time drastically change their mechanical properties. The change is best visible in the areas with hBN wrinkles. After several measurement sessions, folds would flatten, most likely due to sudden changes of pressure (fig. 7.5). Unfortunately, this process was sometimes responsible for the deactivation of the emitters in hBN layers.

After revealing this effect, we made efforts to flatten out the samples right after their fabrication to work only with stable systems. We achieved that by prolonged heating in a vacuum furnace and performing several pumping cycles. Despite these efforts, some samples still exhibited changes after long measurement periods.

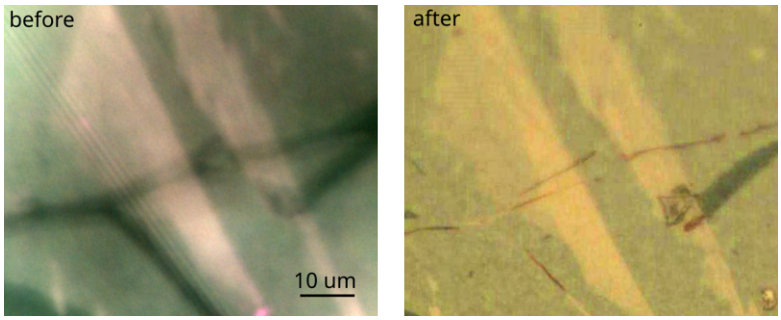

Figure 7.5: Optical microscope photo of the encapsulated $CrPS_4$ flake during low-temperature measurements (before), and after more than a dozen pumping cycles and keeping the sample in the desiccator for two months. Well-pronounced hBN wrinkles collapse, dramatically changing the stress distribution on the sample.

7.2.1 Samples with electrical contacts

Recent studies show, that the magnetic state of 2D magnets can be electrically controlled. By applying a voltage to the flakes, they can undergo transitions like the previously described spin flop (change of the spin direction from out-of-plane to in-plane) and spin-flip (change from spin-up, spin-down state for alternating layers to perpendicular out-of-plane arrangement in all layers). By measuring magnetoresistance in Pt/CrI_3 heterostructures, it was shown, that

spin-flop transition can be induced by spin currents injected from Pt via the spin Hall effect [256]. For very thin, bilayer CrI_3 flakes, it was possible to electrically induce a transition from an antiferromagnetic to a ferromagnetic ground state in the absence of a magnetic field [257, 258]. So far in $CrPS_4$, the application of gate voltage was proven to influence the external field needed to induce a spin-flip transition [159, 160]. This behavior was shown for relatively thick, 10 nm samples [160]. In light of recent discoveries, electrical tuning of ultrathin magnets, especially in their few-layer limit, seems like a promising method to alter their magnetic properties.

In order to explore this route, we prepared 6 nanodevices consisting of electrically contacted $CrPS_4$/hBN heterostructures.

To ensure the highest purity of the samples, we decided to prepare metallic contacts on Si/SiO_2 substrate, and subsequently exfoliate ultrathin magnets on top of them. To precisely manufacture micrometer-sized features, we were using the maskless photolithography system *POLOS uPrinter*. The system allows the illumination of designed features on the sample covered with a photoactivated resist with UV light. There are two types of available resists: positive and negative, reacting differently to the illumination, as depicted schematically in Fig. 7.6. Light illumination makes a positive resist more (around an order of magnitude) soluble in the developer, while a negative resist will be hardened. Usually, positive resists allow for higher resolution of the patterns and maintain their size better, hence are more often used in laboratories. However, their adhesion to the silicon substrates is worse than for negative resists, and the creation of straight, rectangular edges is also more difficult (Fig. 7.6) [259, 260]. Light penetrates resists better near the surface: these areas are softened (hardened) more than the lower parts. Therefore, after the development process (removal of softened (not-hardened) parts of a resist), the remaining resists take the shape of a trapezoid. This undercut

is very beneficial for the lift-off process. Then, in the sputtering process, the whole sample is covered with a metal layer. The remaining resist is removed in the lift-off process. Due to the shape of resist slopes, the resulting metallic contacts may have different edge morphologies. For the positive resist, contacts tend to have sharp edges, which is not ideal for exfoliating ultrathin, sensitive flakes of 2D materials.

A double-layer resist approach was utilized to achieve a smooth, rectangular contact shape. First, substrates were covered with three layers: a primer (heksametylodisilazane: HMDS), to secure good adhesion, and two layers of different positive resists: photoactivated by different light wavelengths (bottom resist supporting the lift-off process: *LOR 3A*, top, imaging resist: ma-P 1215). Every layer was spin-coated and heated on a hot plate. Then, structures were patterned by light, which activated only the imaging layer of the resist. On one substrate, a light-dose test was made, to define the adequate illumination time, long enough to ensure good penetration through the whole resist layer thickness, but also short enough to maintain high pattern resolution.

Subsequently, structures were immersed in developer (*Microposit MF-CD-26*), and rinsed in deionised water. To cover the samples with a metallic layer, *Precision Etching Coating System (PECS) GATAN model 682* setup equipped with argon ion guns was used. In this setup, argon ions are electrically accelerated to hit a target made of a single element like carbon, gold, or chromium. For making the contacts, two elements were evaporated: firstly 5 nm of titanium to ensure good adhesion to Si/SiO_2 substrate, and then 50 nm of gold. In the last step, samples were put in 80° C hot acetone for 1.5 h to lift off the remaining resist, then rinsed in deionized water and dried in clean nitrogen flow.

We used the PDMS transfer technique to precisely transfer exfoliated flakes of $CrPS_4$ onto the pre-patterned substrates. Flakes manifested good adhesion. After this step, we cov-

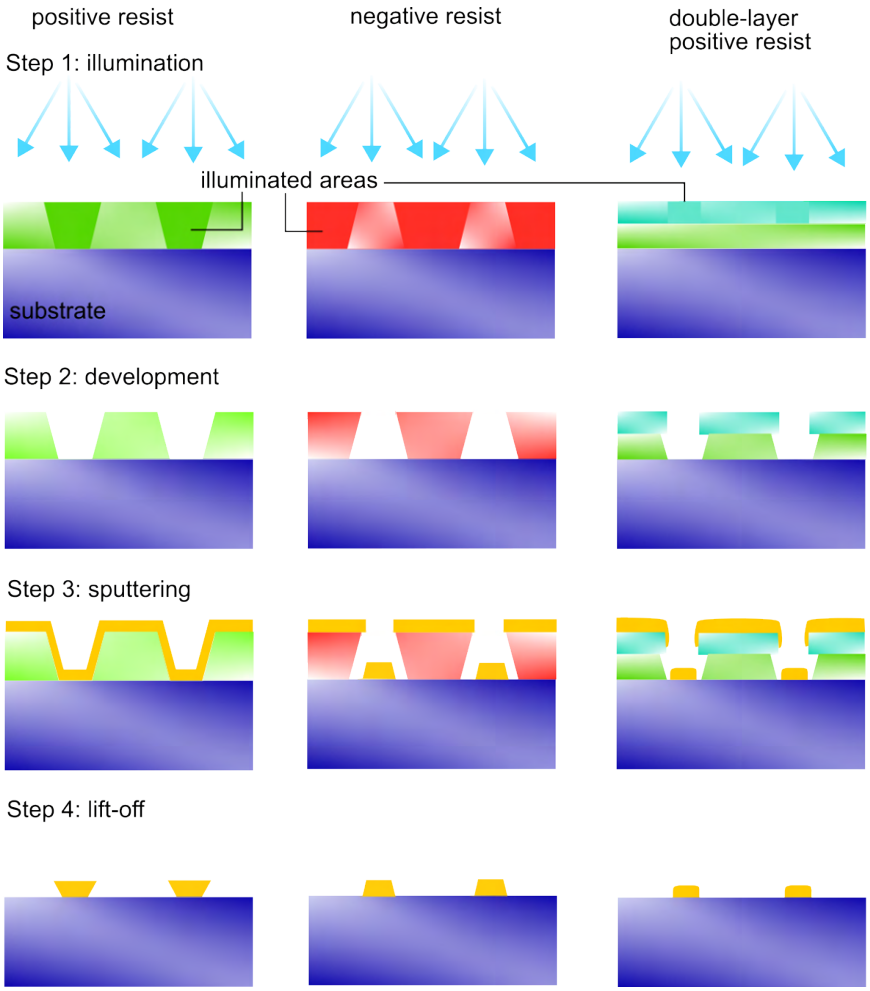

Figure 7.6: Schematic illustration of maskless photolithography process steps using positive, negative, and double-layer resists. Firstly, samples are illuminated with UV light to soften the positive and harden the negative resist. After the development in a solvent, the remaining resist forms trapezoid structures, allowing sputtering of a chosen metal in exposed areas. The lift-off process allows the removal of the resist, leaving precisely positioned contacts. Sputtered metal takes the shape of holes in the resist, which, in the case of positive resist, results in the formation of sharp edges. To prevent this situation, a double-layer resist method can be utilized. Then, only the top resist layer is photoactivated. In the development step, however, also the bottom resist is removed, leaving a slightly underetched structure, allowing the formation of smooth, rectangular contacts.

ered the samples with various MOVPE hBN layers using the wet-transfer technique. Flakes did not detach from the substrate even after immersing them in a water-isopropanol solution.

Step-by-step photos of the devices fabrication are presented in Fig. 7.7. The four yel-

low, symmetric features are the fabricated contacts. On top of them, mechanically exfoliated $CrPS_4$ flakes were carefully positioned. Chosen ultrathin flakes cover the spaces between the contacts, allowing in-plane electrical measurements. Subsequently, the samples were covered with large-area hBN layers (blueish color).

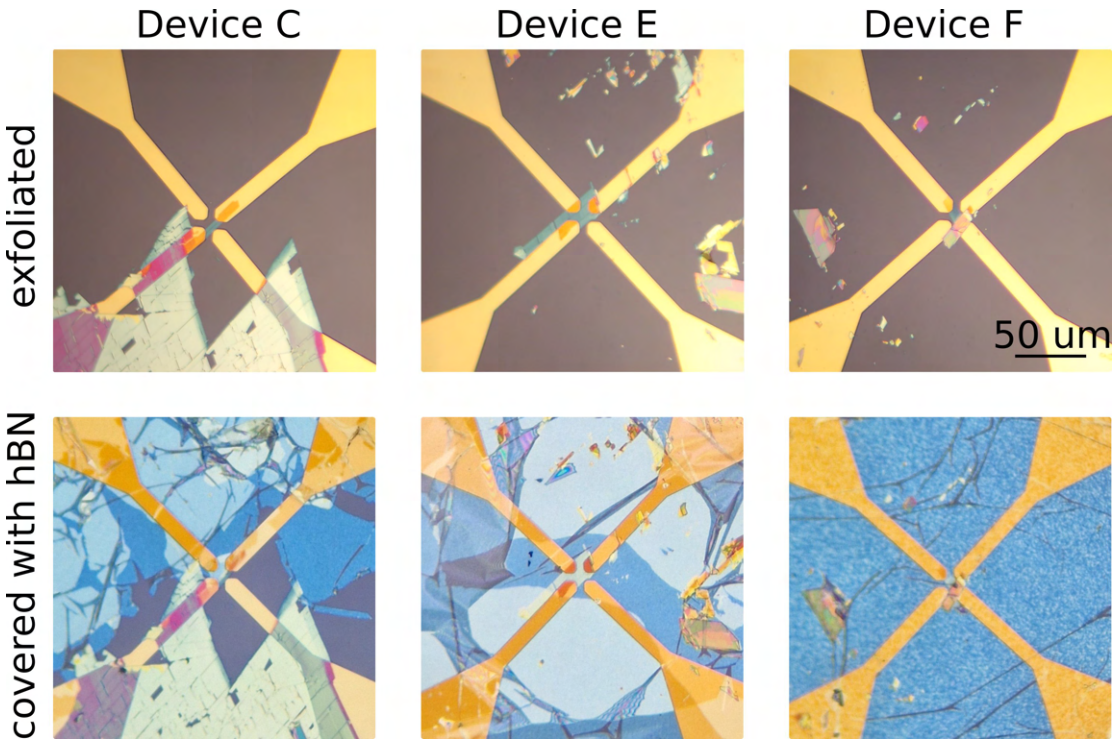

Figure 7.7: Optical image of fabricated $CrPS_4$/epitaxial hBN heterostructures. The top panels show three devices with electrical contacts with exfoliated $CrPS_4$ flakes. The bottom panels show the same devices after covering them with large-area epitaxial hBN layers. Yellow, regular structures are metallic contacts, colorful, irregular features are exfoliated $CrPS_4$ flakes, while bluish areas are epitaxial hBN layers.

7.3 Defects in epitaxial hBN layers: an overview

The search for optically active defects in epitaxial hBN started with determining potentially interesting samples from the MOVPE growth processes. In this work, we focused on un-

treated hBN layers, because typically used defect activation methods (like plasma treatment and neutron or electron beam irradiation) could easily destroy delicate heterostructures.

We chose promising hBN samples, each of them characterized by good crystalline quality, easy delamination, and the potential to host mostly carbon-related defects. In the first round of examination, we performed PL mapping at room temperature to determine the overall positions of the light-emitting centers. We mostly illuminated hBN/$CrBr_3$/hBN samples with a 532 nm and 633 nm continuous wave laser. With this method we found defects characterized by a relatively broad spectrum (FWHM ∼18 meV), with energies close to the excitation laser (fig. 7.8).

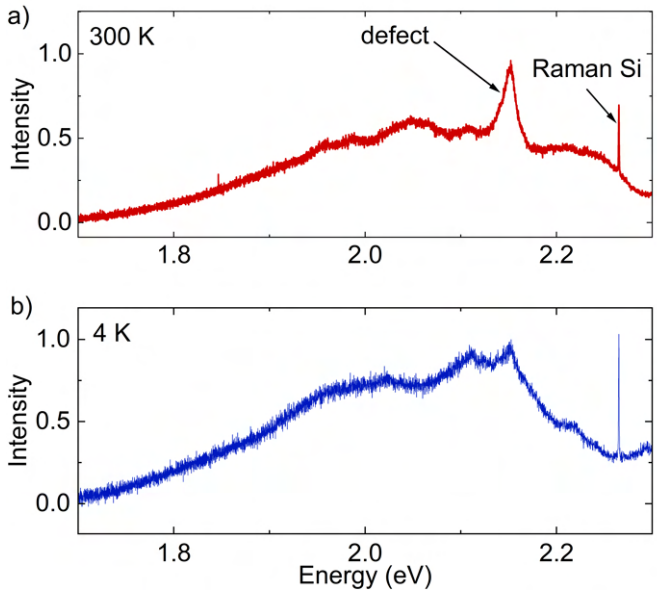

Figure 7.8: A comparison between defect emission at a) 300 K and b) 4 K. The defect emission observed at room temperature is broad (FWHM ∼18 meV) and not very bright compared to a broad background signal. The spectrum recorded on the same spot on the sample at cryogenic temperature is similar, but with a much less pronounced emission peak.

However, when samples were cooled down to ∼4 K, color centers observed at the room temperature were either fading or completely disappearing, while others appeared at different positions or spectral ranges (fig.7.8). Given that the used 2D magnets undergo their corre-

sponding paramagnetic-magnetic phase transitions around 20-40 K, we decided to focus on low-temperature studies.

Fig.7.9 shows exemplary PL mapping results obtained for hBN/$CrPS_4$/hBN samples, at ∼4 K, with a 633 nm exciting laser. An optical image with a red dashed rectangle indicates the map area consisting of either encapsulated $CrPS_4$ flakes or covered by a single or double layer of ∼16 nm thick hBN layer. The integrated emission intensity allows to designate the spatial distribution of light-emitting points in a 1.76-1.95 eV spectral range. Bright color centers are mostly positioned at various irregularities of the sample: at the edges of $CrPS_4$ flakes or at the hBN wrinkles. This observation corresponds well to reports stating that emitters in hBN can be activated by strain [261]. The analysis of the Raman signal originating from silicon and $CrPS_4$ (fig.7.9 c,d) allows to precisely determine the position of the magnetic flakes, as well as thinner areas of hBN layers. The observed signal corresponds well to the optical image of the studied area.

In the search for defects worth further characterization (and by that, we mean stable over time, bright emitters), we performed PL mapping of various areas on many samples. Fig. 7.10 shows the distribution of the light emitted by defects found in the combined area of 12 125 μm^2, while excited with a 633 nm laser. The analysis showed the presence of 296 defects, which averages to ~2.4 defects per 100 μm^2. It is worth noting that in the presented statistics all of the color centers were taken into consideration: also those with small intensity and poor time stability. Such 'poor-quality' emitters constituted the vast majority of the found centers. Defects featuring the desired properties were found less often, approximately 2-3 per 2500 μm^2. The data for the presented statistics were collected in the 1.7-1.95 eV spectral range. The histogram shows two maxima in the distribution of emitters' energy. One maximum is situated close to the energy of the exciting laser, around 1.95 eV. Another maximum is detuned from the first one by around 150 meV. This value corresponds with the previously

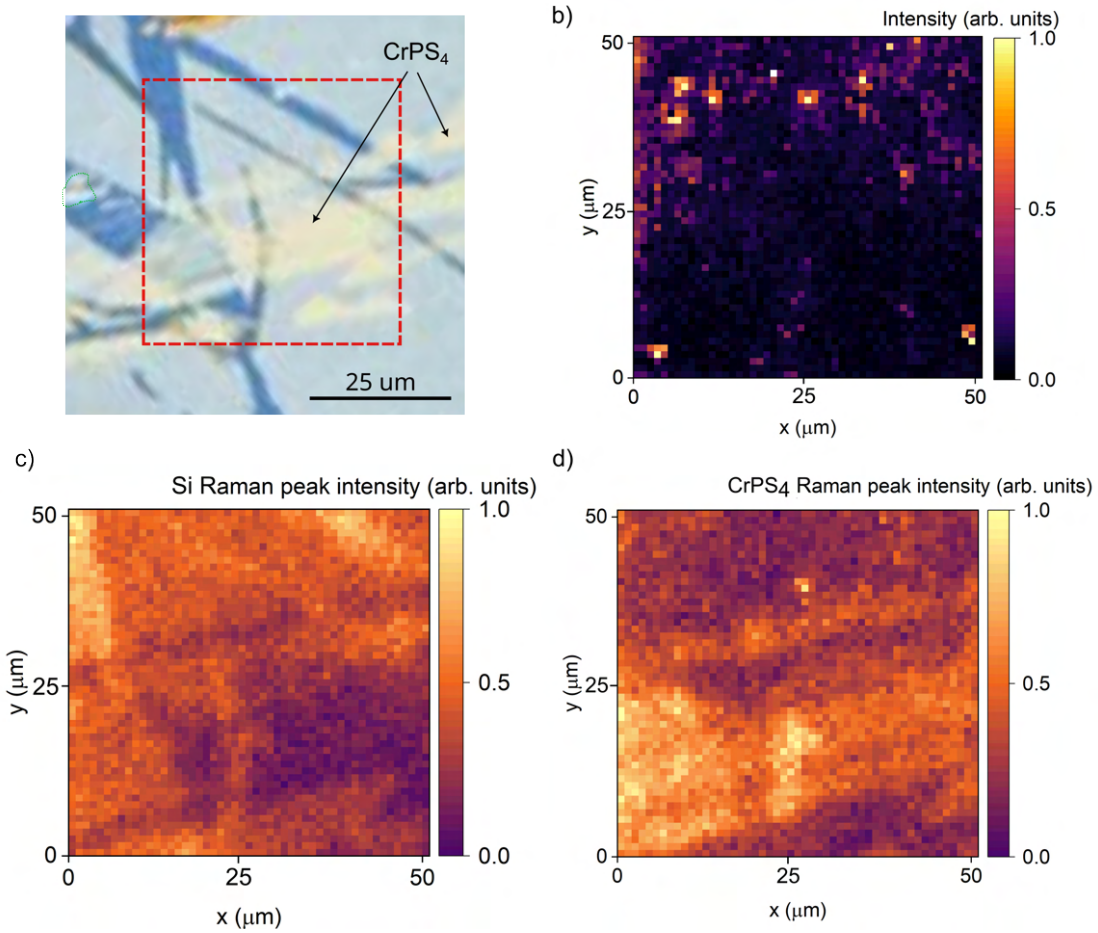

Figure 7.9: a) An optical image of an exemplary PL mapped area of the hBN/$CrPS_4$/hBN sample. The red dashed rectangle specifies the mapped region. b) Map showing the integrated intensity of optically active color centers (in 1.76-1.95 eV spectral range). Defects are usually present at the irregularities and edges of the $CrPS_4$ flakes or hBN layers. Extracted Raman peak intensity originating from c) silicon, d) $CrPS_4$ aligns well with the optical picture.

reported energy of the LO (longitudinal optical) phonon at the K point of the Brillouin zone in hBN [262, 263]. The observed color centers can be also excited resonantly (zero phonon line with the energy close to the laser) and followed by a phonon side band separated by 170 meV, which is a typical value for carbon-based defects, and correlates to the LO phonon at the Γ point of the Brillouin zone in hBN [262, 264].

Fig. 7.11 a) depicts the time dependence of a PL signal originating from a 'poor-quality'

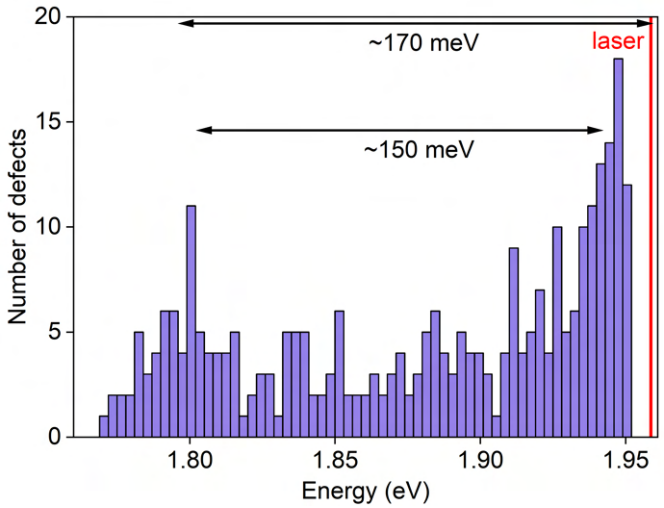

Figure 7.10: A histogram showing the energy distribution of hBN defect-related peaks in 1.76-1.95 eV spectral range, under the 633 nm laser illumination at ∼5 K. Arrows indicate typical zero phonon line (ZPL) - phonon sidebands (PSB) energy separation typically recorded for the defects in hBN.

defect. Its emission energy (initially around 1.943 eV) randomly and rapidly changes over time (spectral diffusion), while its intensity randomly drops or strengthens (blinking), or even completely disappears (photo-bleaching) [265, 266]. Such blinking behavior was frequently observed in hBN color centers and is usually assigned to the presence of dangling bonds and charge traps in the material, which generate and lead to random electric fields and Fermi level modifications. However, the exact mechanisms explaining this unstable PL behavior still remain elusive [58, 267]. Although such 'poor-quality' color centers constitute the majority of found defects, it was not uncommon to uncover stable emitters, as demonstrated by the time dependence in fig. 7.11 b).

In the low-temperature mapping, we could distinguish mostly two types of bright defects (fig. 7.11 c). Type I is characterized by a very narrow spectrum with FWHM ∼0.3 meV and a slightly asymmetric profile, characteristic of acoustic phonons at the lower energetic shoulder of the zero phonon line [263, 268]. Type II is characterized by a broader spectrum, where many different maxima are spread out over a spectral range of ∼30 meV. Even though

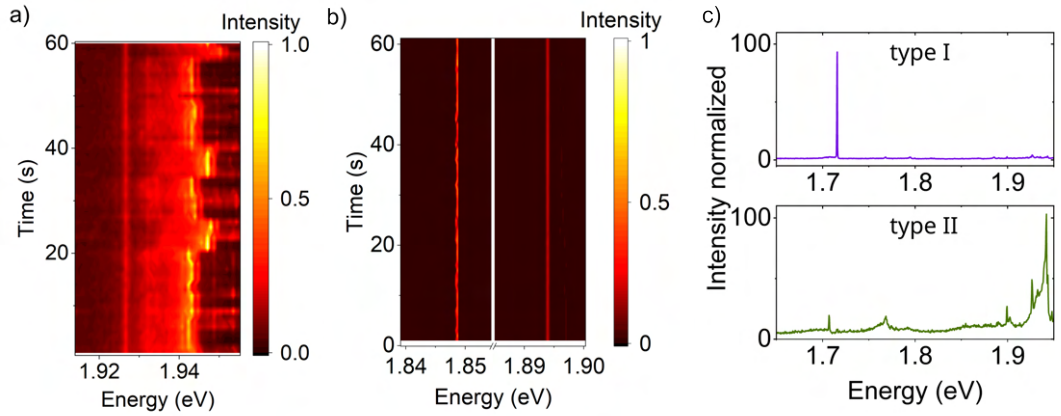

Figure 7.11: PL intensity time dependence for a) 'poor-quality' defect, characterized by many blinking events and spectral diffusion, b) 'good-quality' defect steadily emitting light upon illumination. c) A comparison between the spectra of the two main types of defects recorded on the sample. Type I: the defect is characterized by a single, bright, and narrow PL peak, type II: the emission spectrum is broad, with many maxima.

the exact structural origin of this kind of emission is still being discussed, it was previously observed for hBN color centers [53].

7.4 Initial results obtained for hBN/CrX_3 samples

7.4.1 Structures with exfoliated hBN flakes

As a starting point to study the interaction between defects in hBN and 2D magnets, we prepared heterostructures containing one of the chromium trihalides - chromium tribromide ($CrBr_3$) and commercially available hBN (purchased from *HQ graphene*). We encapsulated a few-layered $CrBr_3$ flake between two hBN layers using described in 5.2.1 section, mechanical exfoliation and deterministic transfer (fig. 7.13 a). Low-temperature PL measurements showed that an additional peak appears in the spectrum at around 720 nm (fig. 7.12). The peak is observed only below the temperature of the $CrBr_3$ magnetic phase transition. The PL signal originating from $CrBr_3$ is centered around 900 nm, so at lower energies than the

observed peak [269, 270].

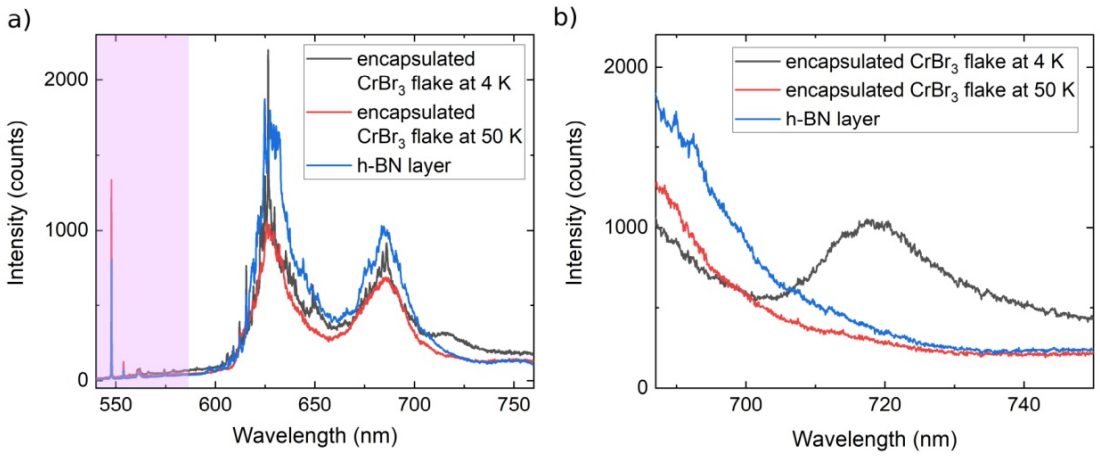

Figure 7.12: Photoluminescence signal of $CrBr_3$/hBN heterostructure in a) a wide spectral range (peaks in the violet area of the graph correspond to Raman spectra of a silicon substrate and hBN) b) focused on the $CrBr_3$ induced PL peak.

Fig. 7.13 shows the optical image of the studied flake and the 720 nm peak intensity map. The results indicate that the signal comes only from the area of the encapsulated flake. The appearance of an additional emission peak can be a manifestation of the interaction between the defect state in hBN and a 2D magnet. The energy of the observed emission peak corresponds to previously reported defect-related emission from hBN in a magnetic field [271]. On the other hand, demonstrations found in the literature usually point to the necessity to artificially activate the defects, hence, it is unlikely that an untreated, commercially available hBN layer would give rise to uniformly spaced, light-emitting centers.

After the low-temperature measurements, the $CrBr_3$ flake was significantly damaged. Promising initial results obtained for samples fabricated of only mechanically exfoliated flakes allowed us to move further and focus on studying the interaction between epitaxial hBN and 2D magnets.

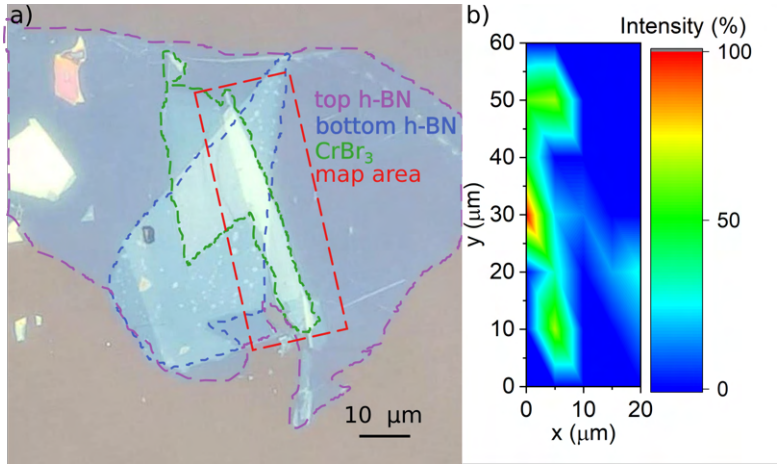

Figure 7.13: a) Optical image of the prepared $CrBr_3$/hBN heterostructure. b) 720 nm peak intensity map shows that the signal appears only in the area of the flake.

7.4.2 Structures with MOVPE grown hBN

For this study, we used a sample with randomly exfoliated $CrBr_3$ flakes of various sizes and thicknesses, encapsulated between two ∼16 nm thick hBN layers. Interestingly, it was the same sample hBN 4 (MOVPE processes G141, G142), which was found to be the best substrate for further growth of $MoSe_2$ in chapter 6. During the experiment, we mostly focused on gathering PL data at temperatures close to the Curie temperature of $CrBr_3$ (estimated to be ∼ 25 K for monolayers [272], up to around 37 K for bulk [273]). The general methodology was to map the chosen region of the sample at 5 K to find bright and stable emitters and then proceed to check whether the signal changes close to the phase transition temperature. In this section, we present the most interesting results obtained for heterostructures utilizing $CrBr_3$, which has initiated further studies on different structures.

Fig. 7.14 a) presents a broad PL spectrum measured on a small hBN wrinkle positioned on a thick (∼60 nm) $CrBr_3$ flake (inset). The spectrum consists of a broad signal centered around 1.35 eV originating from $CrBr_3$ photoluminescence, as well as a series of narrow,

high-energy peaks originating from the Raman signal of silicon and $CrBr_3$ [274]. Apart from these, two narrow, bright peaks at energies 1.797 eV and 1.776 eV are also visible. We ascribe them to the presence of optically active defects in the hBN layer, as they only appear on a special localisation. Fig. 7.14 b) shows a close-up of the observed signal. Defect-related peaks are asymmetric, sharp at higher energy, and slowly declining at lower energies, which constitutes a typical zero-phonon line of the defects found in hBN. When we zoom in the spectrum exactly 150 meV below the defect-related emission energy, we discover two low-intensity broader features, corresponding to the phonon side bands (fig. 7.14 c).

The two ZPLs were correlated: if one slightly darkened or changed its energy, the other one mimicked it, which leads to the conclusion that both peaks could originate from the same defect center.

The temperature-dependent studies unveiled an interesting evolution of the studied peak energy. While Raman signals originating from the silicon substrate and an underlying $CrBr_3$ flake have not experienced a significant shift (fig. 7.15 a), the defect-related emission energy changes at different temperatures (fig. 7.15 b). To further investigate this phenomenon, we recorded PL spectra at more temperatures during both: the cool down and heat up process. The temperature was stabilized for at least 5 min before every measurement, which was found to be sufficient to reach the stable temperature of the sample. The defect-related signal was maximized every time by carefully adjusting the position of the sample. For clarity, in the following analysis, we focus only on the most intense defect emission, as the other one showed the same characteristic. Fig. 7.15 c) depicts the temperature-dependent changes of defect-related emission energy during the cool down (blue) and heating up (red) of the sample. Contrary to the stable Raman signal, both dependencies show a pronounced cut-off around 35-37 K. This temperature corresponds well to the previously reported Curie temperature for $CrBr_3$ [273].

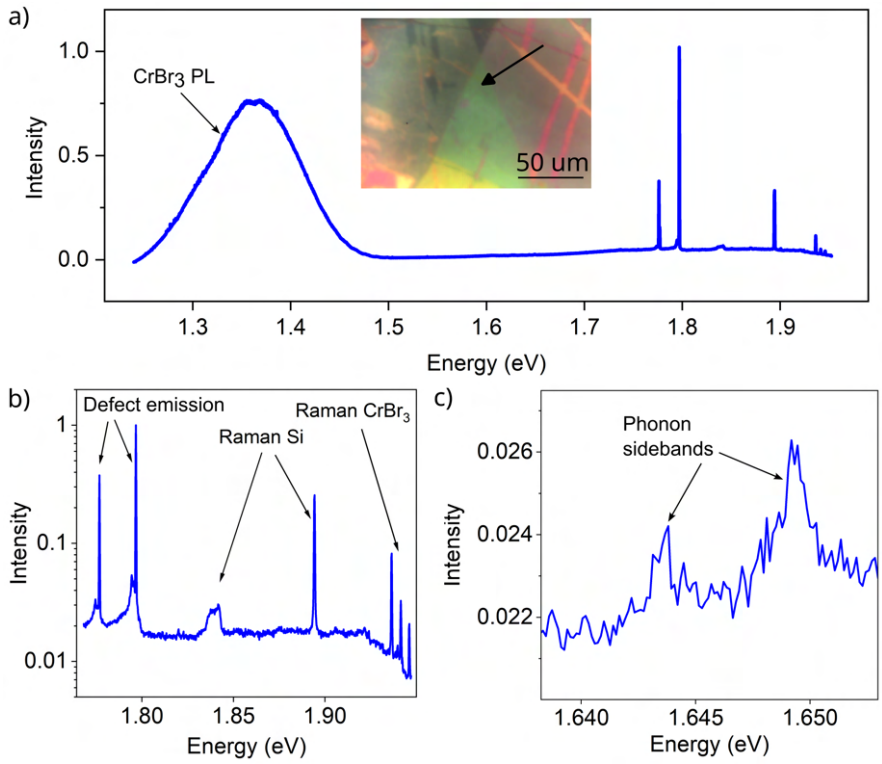

Figure 7.14: a) Wide spectral PL of the $CrBr_3$/hBN sample using a 633 nm laser illumination. The inset shows the exact point of data collection: on an hBN wrinkle on top of a thick 2D magnet flake. A broad feature in the spectrum centered around 1.35 eV originates from $CrBr_3$ photoluminescence. b) Narrow peaks observed in the higher energy range correspond to the Raman signal from silicon and $CrBr_3$, while two asymmetric peaks centered at 1.797 and 1.776 eV originate from the defect states in hBN layer. c) At energies $\sim$150 meV below the defect-related peaks, low-intensity, broad features can be seen, which we ascribe to the observation of phonon sidebands (phonon modes observed at the K point of the Brillouin zone).

Measurements were performed in the following manner: the sample was first cooled down to cryogenic temperatures, stabilized, and then the PL spectra dependency for heating up was recorded. The cooldown dependency measurements followed quickly after that. One can see, that the low temperature readings do not overlap. Since color centers in hBN can be sensitive to their surroundings [275, 276], a slightly different strain, magnetic ordering, or electric charge distribution can lead to different final states during temperature change cycles.

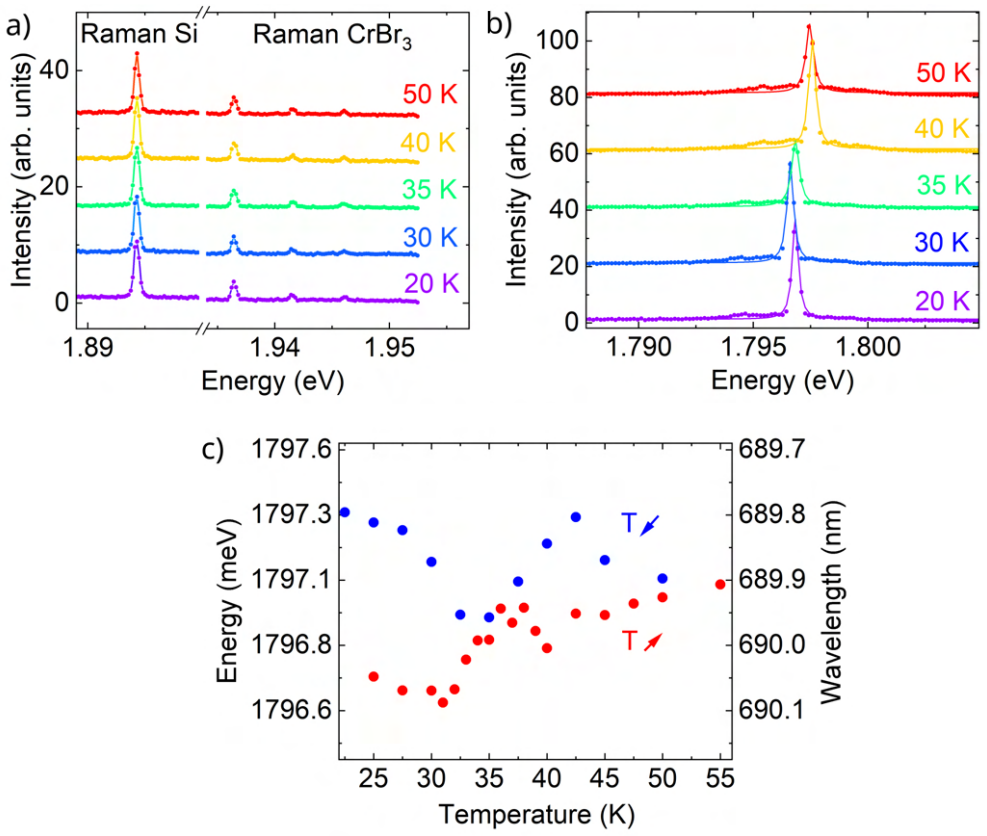

Figure 7.15: a) The Raman signals originating from the silicon substrate and thick $CrBr_3$ flake do not significantly change their positions and intensity at various temperatures. b) Defect-related peak emission displays a slight shift in temperature-dependent measurements. Solid lines show Lorentzian profile fits to the most intense PL feature. c) hBN defect-related emission energy temperature dependencies extracted during cooldown (blue) and heating (red) cycle. Around 35-37 K, a discontinuity can be spotted for both dependencies, corresponding with the Curie temperature of an underlying 2D magnetic material.

The observed discontinuities showed a change of around 0.5 meV to the ZPL energy during the transition. The shift is rather small and comparable to small shifts resulting from minor changes in the measurement location. In order to check whether the observed effect is not due to the micro shifts of the sample, we extracted the emission energy from PL maps measured at various temperatures (fig. 7.16). Fig. 7.16 b) shows the intensity map of the defect-related peak at 20 K. The spatial intensity distribution forms a Gaussian profile, as ex-

pected for a point defect illuminated by a laser beam also characterized by a Gaussian intensity distribution.

A Lorentzian profile was fitted to the defect-related peak for all of the points of the maps. Fig. 7.16 c) shows the spatial distribution of the peak energy at 20 K, resembling a linear gradient. White areas on the map indicate points where the defect-related peak could no longer be observed, and the fitting did not converge. We averaged the emission energy values from each map and obtained a result confirming our previous observations (fig. 7.16) a). This time, the energy shift during a magnetic-paramagnetic transition was even bigger $\sim$1 meV.

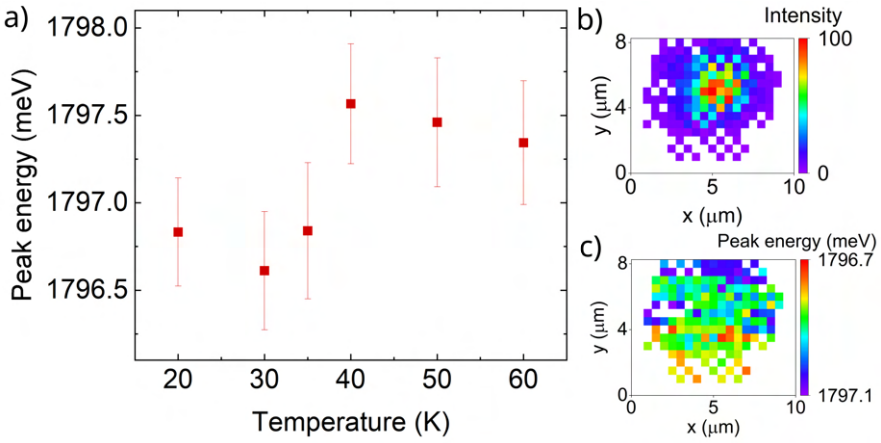

Figure 7.16: a) Temperature dependence of defect-related emission energy extracted from averaged PL maps. b) A typical Gaussian intensity profile of the defect emission at 20 K. c) Spatial distribution of the studied peak energy showing a linear gradient.

We acknowledge that the observed energy shift lies within the margin of error, and the phenomenon needs more study. The described result was a motivation for further measurements with another 2D magnet to confirm that such effects can occur. On account of continuity, we describe our initial predictions here, while the following sections present results for a different 2D magnet.

The obtained result shows that the emission from the defects in hBN correlates with the ferromagnetic-paramagnetic phase transition temperature. This observation leads to the con-

clusion that the already used in the heterostructures hBN can be used as a sensor of the state of the underlying material. However what it the exact mechanism behind this interaction?

The emission energy of the defects in hBN can be modulated in many different ways. Some color centers in hBN, like boron vacancies, are spin-dependent and can interact with neighboring materials magnetically [56, 63]. It is also possible to use an electric field to activate and tune the emitters exhibiting the Stark effect [66, 67, 70]. Another method utilizes mechanical strain to tune the emission up to 12 nm [60, 72–74, 277].

To connect it with the state of an underlying 2D magnet, we must look at the temperature-dependent structural properties of $CrBr_3$. The material exhibits an anomalous thermal expansion coefficient evolution. Under the Curie temperature, the coefficient for the a (in-plane) lattice parameter is negative, while over this temperature, as well as for c (out-of-plane) lattice parameter, it is positive, as shown by the neutron and X-ray diffraction studies [278, 279]. Below the Curie temperature, the interatomic distances drastically change, which affect the exchange interaction responsible for the magnetic properties of the material. Additionally, structural changes can be tracked by Raman spectroscopy of different phonon modes [270, 279]. In the literature, an anomalous rise in the phonon frequency is observed below the Curie temperature, as opposed to the expected thermal behavior originating from the anharmonic approach [279, 280]. Such a behavior indicates a strong spin–phonon coupling in $CrBr_3$ layers and is believed to modify the magnetic exchange interactions in the material [279].

We wanted to assess if a similar characteristic is visible in our studied sample. Fig. 7.17 shows the temperature evolution of two $CrBr_3$ phonon energies with A_{1g} (blue) and E_{2g} (red) symmetries [272]. Raman spectra were measured at the same point where the defect-related emission appeared. A typical temperature dependence can be described by the following an-

harmonic model presented in [280]:

$$\nu(T) = \nu_0 + A\left(1 + \frac{2}{e^{\hbar\nu_0/2k_BT}}\right) + B\left(1 + \frac{3}{e^{\hbar\nu_0/3k_BT}} + \frac{3}{e^{\hbar\nu_0/3k_BT}}\right), \tag{7.1}$$

where ν_0, A, B are fitted parameters.

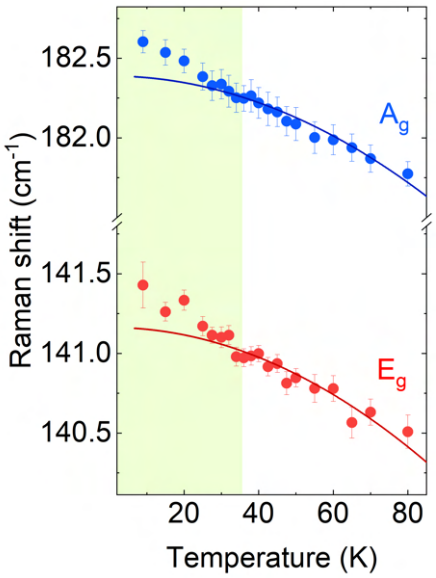

Figure 7.17: Temperature evolution of two Raman modes originating from $CrBr_3$, with fitted curves derived from an anharmonic approach of phonon temperature dependence. Green coloring indicates the ferromagnetic region.

Our results presented in Fig. 7.17 are consistent with literature reports. Below the Curie temperature, the phonon energy for both studied modes anomalously increases, deviating from the anharmonic model. This behavior indicates a strong spin-phonon coupling in the material. A Curie temperature of ∼37 K extracted from our Raman spectroscopy studies of $CrBr_3$ aligns with the value predicted from the hBN color center characteristic.

7.5 Properties of hBN/$CrPS_4$ structures

Promising results obtained for $CrBr_3$/hBN samples prompted us to conduct further studies, this time on heterostructures containing a different, more resistant to environmental conditions chromium thiophosphate [157]. The samples were prepared in the previously described wet transfer scheme (fig. 7.1). Unless written otherwise, the hBN used for the structures was sample hBN 4. We wanted to study whether the temperature-dependent effect can be observed in heterostructures containing another 2D magnet, as well as to study the hBN/2D magnet interactions in external electric and magnetic fields.

7.5.1 Temperature-dependent measurements

Similar to before, we mapped photoluminescence at various areas of the sample in order to find bright and stable defects. Fig. 7.18 depicts an exemplary defect that manifests an interesting temperature evolution. The color center is found right on the edge of a $\sim$12 nm thick $CrPS_4$ flake, on a fork-like hBN wrinkle. Again, the emitters' spatial intensity corresponds to a Gaussian profile. Fig. 7.18 b) shows the PL spectrum of the studied emitter. A broad and rich low-energy feature corresponds to excitonic emissions from $CrPS_4$. Bifurcated characteristics of this signal can be altered by temperature, number of layers, and density of defects in the 2D magnet structure [281, 282]. Raman signals from the magnetic flake and the substrate can be seen at high energies. Finally, a narrow and bright asymmetric feature at $\sim$1.87 eV corresponds to the defect emission.

Further optical studies performed in the region allow us to precisely determine the position of $CrPS_4$ flakes (fig. 7.19 a-c). Interestingly, one can observe a slight enhancement of the Raman signal of $CrPS_4$ at the hBN wrinkles position. A possible explanation for this phenomenon is that hBN layers form micro-membranes at the flakes' edges. Our recent studies

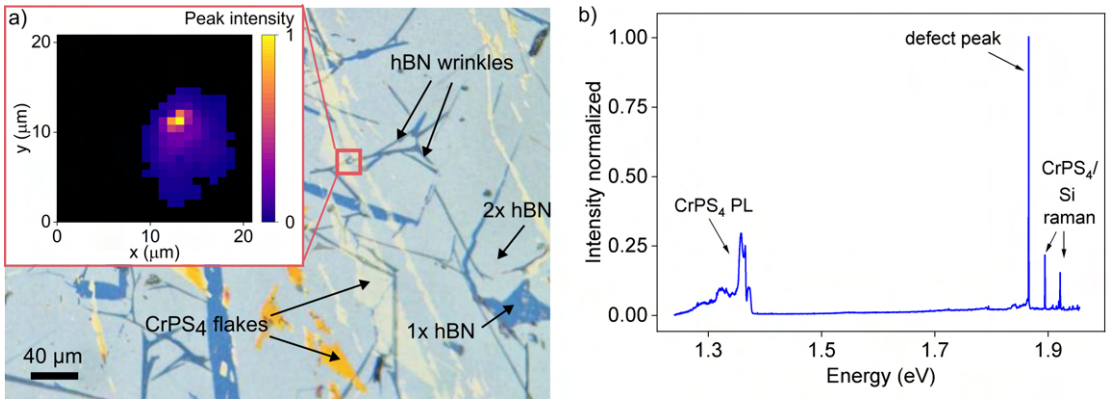

Figure 7.18: a) Optical image of a hBN/$CrPS_4$/hBN sample. The heterostructure consists of 2D magnet flakes of various shapes and thicknesses, as well as many hBN layer wrinkles. The inset shows a spatial intensity distribution of a defect-related light emission. b) A broad spectrum of the studied emitter illuminated by a 633 nm CW laser. Broad low-energy peaks originate from the photoluminescence signal from $CrPS_4$. Narrow, high-energy peaks correspond to the Raman signal of silicon and $CrPS_4$. The defect-related peak around 1.87 eV is bright and narrow.

show that such suspended structures are capable of amplifying Raman signals due to interference [283].

Similar to the previously observed dependencies for hBN/$CrBr_3$ samples, the spatial profile of the mapped emitter energy is a linear gradient (Fig. 7.19 d). Time-dependent studies (fig. 7.19 e) depict a great stability of the studied defect, showing no bleaching or blinking. Although very narrow (<1 meV) at low temperature (<60 K), the emission from the defect exponentially broadens with an increase in temperature (fig. 7.19 f). The observed exponential dependency of the broadening parameter ($\Gamma(T)$) suggests that it can be described with the following formula [284]:

$$\Gamma(T) = \Gamma_0 + \gamma T + \frac{\Gamma_{LO}}{\exp(h\nu/kT) - 1}, \tag{7.2}$$

where: Γ_0 – zero temperature broadening parameter, γ, Γ_{LO} – parameters describing interactions of excitons with acoustic and optical phonons accordingly, and $h\nu$ – phonon energy.

The extracted phonon energy is (54±12) meV, which corresponds to the energies of acoustic phonons from the M and K Brillouin zone [285]. This observation suggests a strong localization of the center and the coupling with phonons from the Brillouin zone boundary.

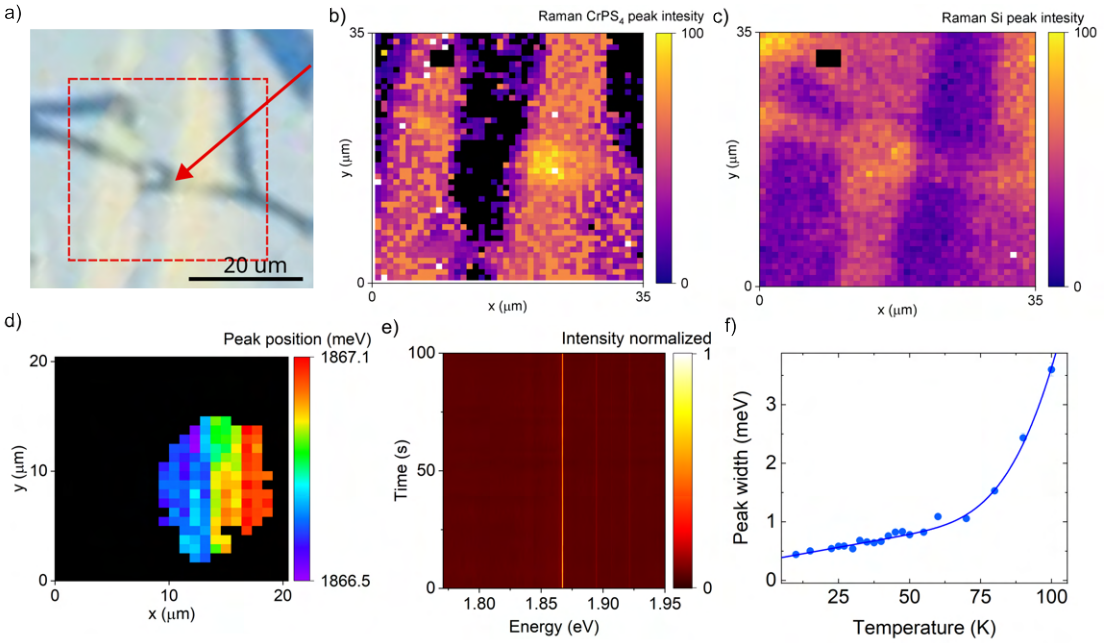

Figure 7.19: a) An optical image of the sample with a red dashed rectangle indicating the mapped region, and a red arrow pointing to the emitter position. Raman signals from b) $CrPS_4$ and c) silicon correspond to the optical picture and show a slight enhancement near the hBN wrinkles. d) A spatial distribution of the defect's peak position. e) Time-dependent PL measurements of the studied color center show excellent stability. f) Temperature evolution of the defect-related peak width shows exponential broadening (fitted formula based on [284]).

To precisely determine the emitter's energy temperature evolution, we again used the method of averaging the values obtained from PL maps. The result of our approach is presented in fig. 7.20 a). Below the Neel temperature of $CrPS_4$, the emitter's energy increases linearly by ∼1.5 meV. At the temperature of ∼35 K, we see a clear cut-off, the dependency reverses, and the peak energy slowly decreases. The dependence is clearly observed for both: heating up and cooling of the sample. The outcome could be reproduced even 4 days after the initial experiment, after a few more cooling and pumping cycles. Our result is consistent

with other literature reports, determining the phase of the 2D magnet by Magneto-optic Kerr effect microscopy [157] or magnetic susceptibility measurements [286].

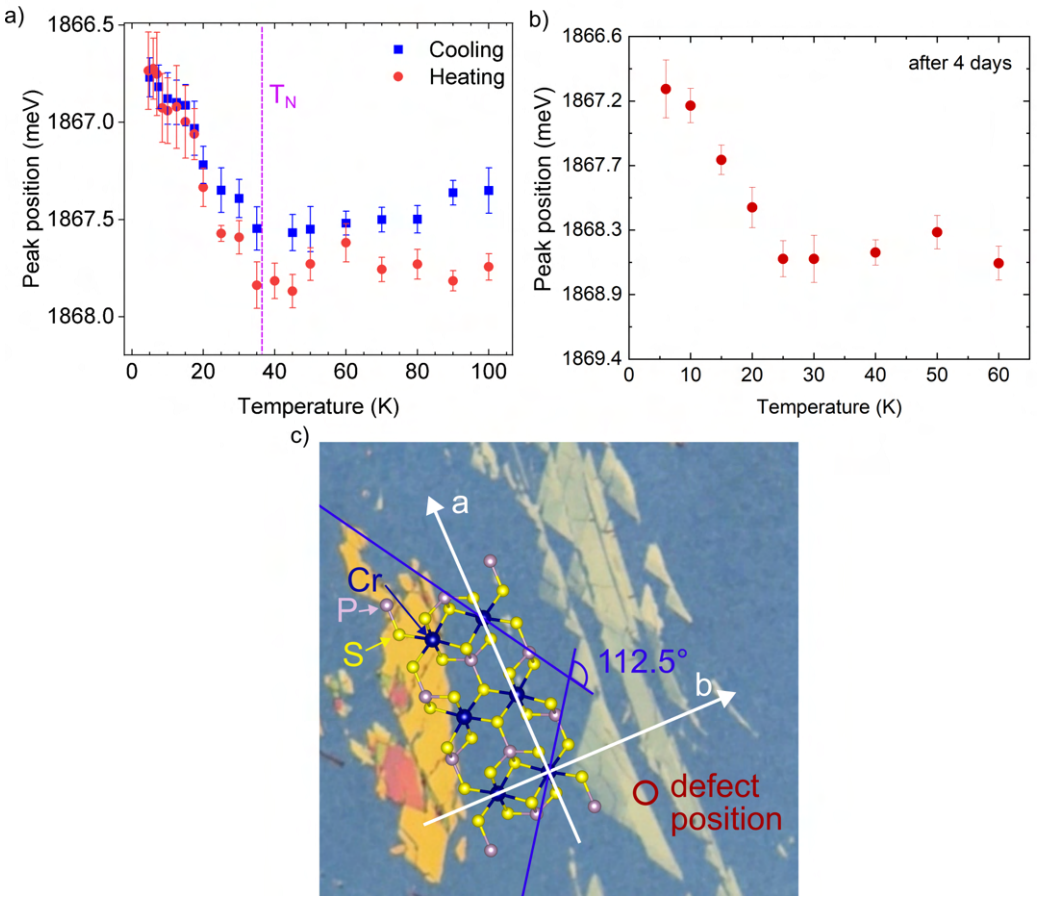

Figure 7.20: a) Temperature dependence of an emitter energy. Each value is extracted from averaged PL maps measured at each temperature. b) The result is reproduced after 4 days. c) An optical image of the studied sample with an overlayed atomic structure and crystallographic orientations (for clarity image shows $CrPS_4$ flake before covering with a top hBN layer).

To understand the observed phenomena, we look into the structural properties of the studied 2D magnet. Fig. 7.20 c) shows an optical image of the studied region before covering it with a top hBN layer to better depict the crystallographic orientation of the flakes. Mechanical exfoliation leaves the flakes with preferentially cleaved edges with characteristic angles of 112.5° and 67.5°, which allows us to determine their relative orientation [150, 287].

The studied emitter is placed at the edge of the flake, perpendicular to the $CrPS_4$ b axis.

We performed an analysis of $CrPS_4$ Raman spectra measured at the same position as the emitter to determine whether the temperature evolution of phonon modes can be also useful in tracking the phase transition. Fig. 7.21 shows the studied peaks, marked after [150].

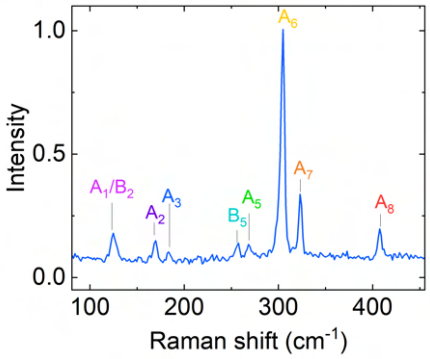

Figure 7.21: Analyzed $CrPS_4$ Raman peaks. Spectrum is measured at 25 K, under a 633 nm laser illumination.

Unfortunately, due to a relatively strong background originating from an hBN layer, we could take into consideration only eight phonons. Two peaks (A_1: 117.9 cm^{-1}, B_2: 115.2 cm^{-1}) are spectrally close, and even though the used diffraction grating (600 grooves/mm) should be able in principle to resolve them, we observed only one peak. A possible explanation is that according to [288] B_2 peak intensity is significantly lower than A_1, hence we most likely observe only the A_1 contribution. The measurement was made in an unpolarized setup, meaning that the incoming and detected light did not pass through any polarization optics for higher signal excitation intensity. Still, in such a setup, light coming from the laser is mostly linearly polarized.

Fig. 7.22 shows the Raman shifts of the studied phonon modes. All of the peaks show a general behaviour of decreasing energy with rising temperature. Peak A_8 manifests characteristics similar to those observed in hBN/$CrBr_3$ samples: the phonon energy rapidly rises below the Neel temperature of $CrPS_4$. The Raman shift A_1/B_2 also has an interesting char-

acteristic, with a pronounced maximum between 35-55 K which was not observed in other works [163, 288]. This phonon mode additionally shows the greatest range of variability. According to the literature, peak A_3 should manifest the biggest energy changes upon approaching Neel temperature, with a sudden intensity drop over this temperature [163, 288]. Indeed, we observed A_3 signal decline, with a complete extinction over 80 K, however these changes did not show a clear cut-off. Such a behaviour can be due to the far off-resonant excitation of the flakes discussed in [288]. The excitation energy dependence in the material is explained by a resonance with the bandgap transition observed at ~2.4 eV [152]. Additionally, the temperature and magnetic transitions can alter band structure and resonance conditions, particularly when excitation energy approaches the bandgap [288]. In our case, the excitation is far off-resonant (1.96 eV), which does not give as pronounced correlation with the phase transition temperature.

When we look closer at the structural properties of $CrPS_4$, we learn that it is a highly anisotropic system. X-ray diffraction and nanoresonator frequency analysis show, that the material has a different mechanical response in different directions [162, 163]. While a and c lattice parameters manifest a typically observed, slightly positive thermal expansion, the b axis shows an anomalous characteristic. The chromium-chromium distances decrease along the b axis when heated, resulting in a negative temperature expansion coefficient and a pronounced feature near the Neel temperature. Looking back at the position of the studied defect on the sample (fig. 7.20 c), the emitter lies directly on the edge of the flake perpendicular to the crystallographic b axis. Therefore, this point should experience the highest strain from an underlying 2D magnet.

To further check whether the defect ZPL tuning could originate from a direct effect of the temperature sweep, we performed additional studies on other emitters, either found on hBN layer only (fig. 7.23 a) or on a flat region in the middle of $CrPS_4$ flake (fig. 7.23 b). Again,

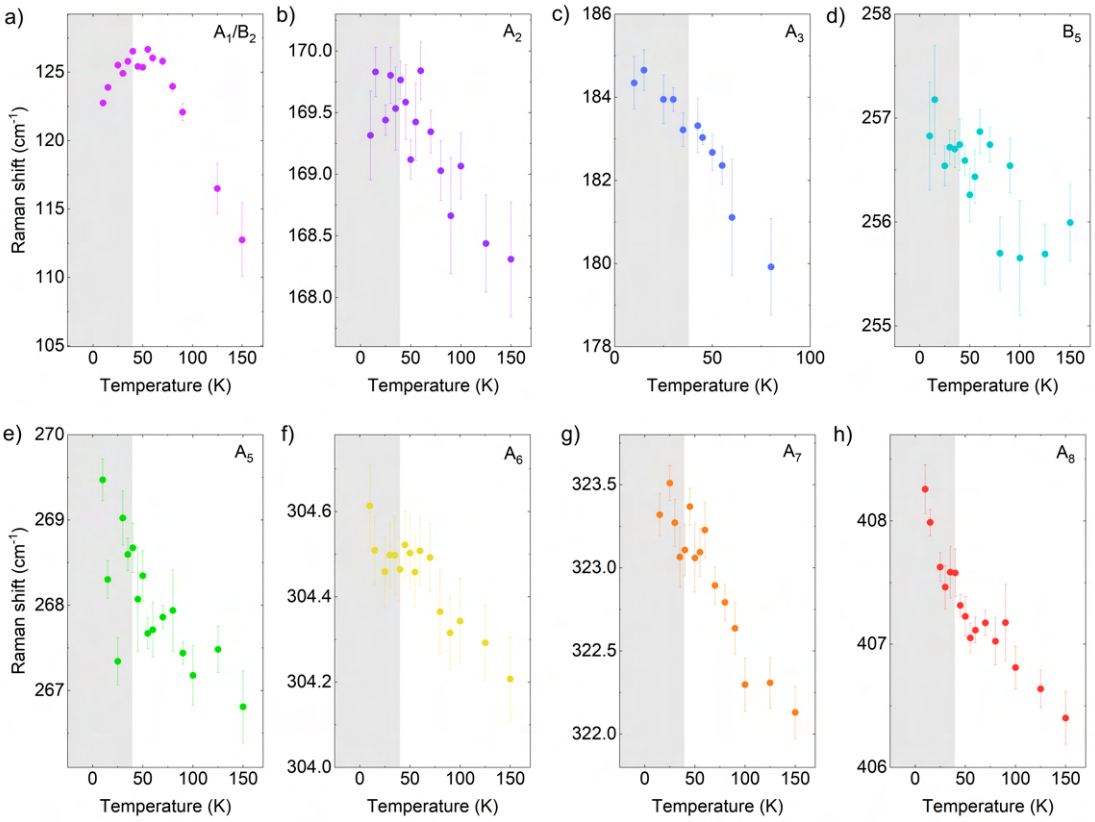

Figure 7.22: Temperature dependence of Raman shifts of 8 studied $CrPS_4$ phonon modes. Gray areas indicate the antiferromagnetic state of the nanomagnet.

we measured PL maps to average the peak's energy at each temperature. The obtained results indicate, that the temperature itself does not significantly influence the optical response from color centers and does not result in a cut-off characteristic like the one shown in Fig. 7.20. In the case of a point positioned on the flat $CrPS_4$ flake, a small maximum can be observed around the Neel temperature (fig. 7.23 b). It is not unusual, as the underlying flake still undergoes mechanical changes, just not as pronounced as in the case of the point positioned at the edge. However, with our setup, we can not unequivocally determine whether this effect is dependent on the 2D magnet phase transition: the difference between the defect's ZPL energy in the low-temperature state and near the phase transition is small (<0.5 meV),

comparable to the measurement resolution.

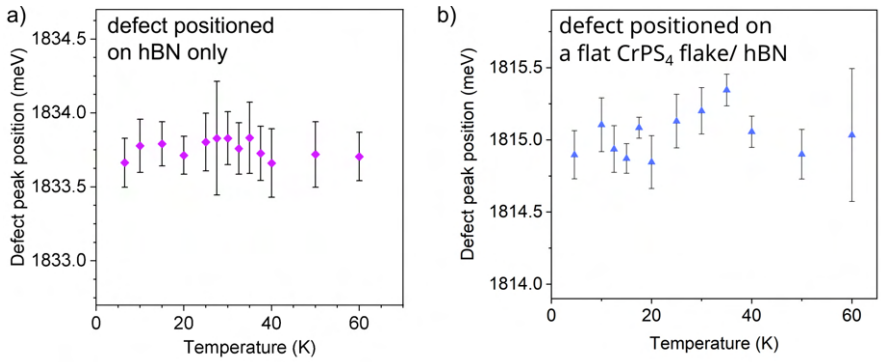

Figure 7.23: Temperature dependence of ZPL energy of color centers found on a) hBN layer, b) flat $CrPS_4$ flake, extracted from PL maps gathered at each temperature. Both dependencies do not show significant changes.

In this section, we presented unusual temperature dependencies of emitters in hBN layers positioned at $CrPS_4$ flakes. There are different possible explanations of the observed behavior, including mechanical strain, local charging, or direct magnetic interaction. To further explore processes occurring in the hBN/$CrPS_4$ system, we performed optical measurements in an external magnetic field.

7.5.2 External magnetic field measurements

All of the measurements presented in this section were performed using the setup described in section 5.1.1. The applied magnetic field was directed perpendicularly to the sample surface.

We utilized sample hBN 4, and the measurements were performed at 10 K with a 633 nm laser excitation unless otherwise noted. We performed PL mapping to determine the positions of the defects, and measured time-dependencies to check their stability. We probed the optical response of 39 stable emitters in a high external magnetic field. Below we present the most interesting findings.

Fig. 7.24 a) presents a PL spectrum of the studied emitter. The defect was positioned

at the edge of a thick (∼100 nm) $CrPS_4$ flake. The PL signal is extremely rich: it bifurcates into many different peaks and maxima. A closer analysis allows us to notice the patterns appearing in the spectrum. Parts of the signal are reproduced at energies ∼170 meV lower than the original corresponding to the phonons from Γ point of the Brillouin zone found in hBN. This observation allowed us to separate the spectrum into five features, marked with numbers 0-4 and different colors in the picture 7.24 a). ZPLs occupy the high-energy part of the spectrum (also marked with a dark violet rectangle with the Roman number I). The shape of the highest-energy maximum centered around the laser energy indicates, that the color center was excited resonantly. At lower energies (part of the spectrum marked with the Roman number II and a violet rectangle), we observe phonon sidebands reconstructing the trends of the ZPL region. One can see, that some narrow features present in ZPL 1, around 1.9 eV, are not repeated in the phonon sideband (PSB). It is due to the fact, that these peaks correspond to the Raman signal of silicon and $CrPS_4$.

At low energies (<1.62 eV) we were able to observe yet another PSB (marked with a light violet rectangle and the Roman number III). The observed maxima (0-4) possess a spectral width in the range of 30-45 meV, corresponding to the reported energy region of phonon states with high-density states in the M and K directions of the Brillouin zone [289]. All of them manifest a similar characteristic: the feature starts at high energy with a narrow peak, and then the intensity rapidly rises to a narrow maximum. At lower energies, the slope slowly decreases with a set of smaller, narrow peaks. Such a spectral shape is not unusual for emitters in hBN and was reported previously [53, 263]. All ZPLs are separated from their corresponding PSBs by a very similar spectral distance ranging between 171-175 meV. This value perfectly matches the reported LO phonon energy for hBN [262, 263]. Fig. 7.25 further visualizes the similarity between specific features and shows a zoom into the maxima marked with number 4 (pink background color in Fig. 7.24 a), where the blue spectrum is the ZPL

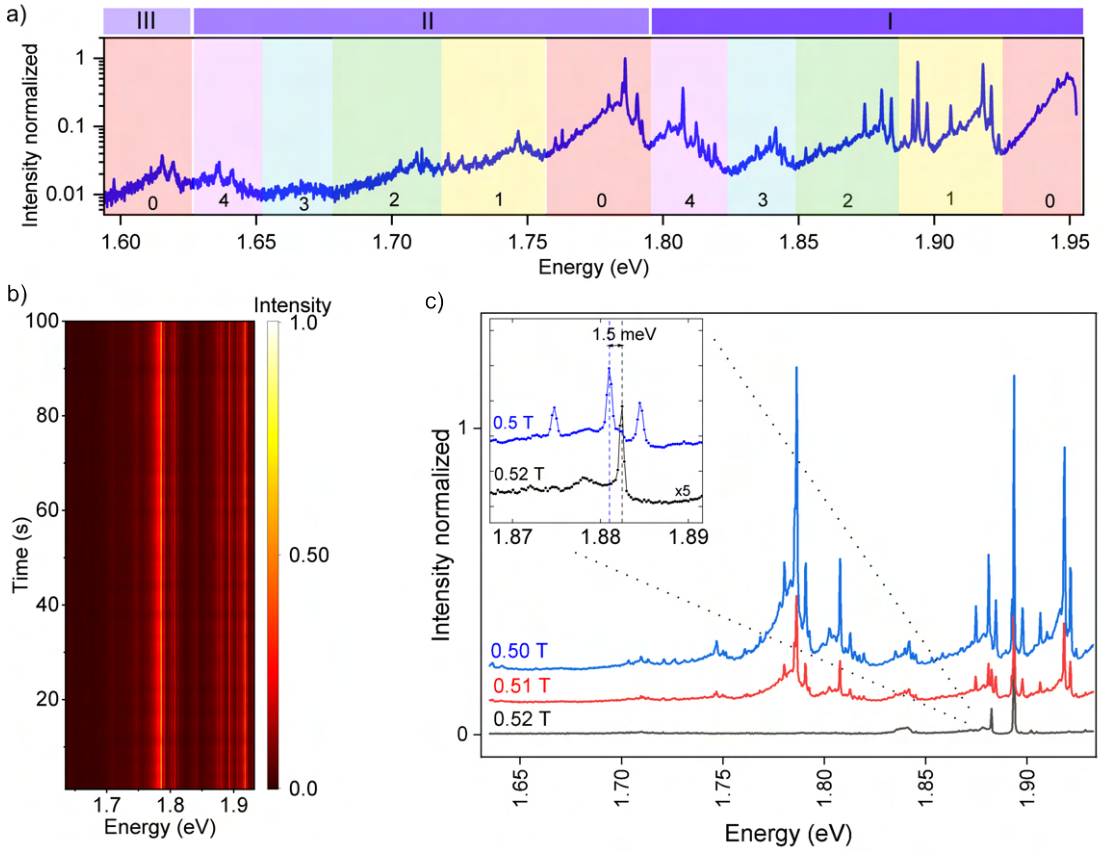

Figure 7.24: a) The PL spectrum of the studied emitter, excited by a 633 nm laser. The spectrum consists of five ZPLs (numbers 0-4, region I), followed by corresponding phonon side bands (numbers 0-4, regions II and III). b) PL time dependence shows good stability of the color center. c) Spectra measured before (blue), during (red), and after (black) the spin-flop transition of $CrPS_4$. A signal from the hBN emitter drastically decreases and shifts $\sim$ 1.5 meV, while the silicon Raman signal remains the same.

(markings I, 4), and the red spectrum shows the corresponding phonon sideband (markings II, 4). We see that the overall shape and specific peaks are reproduced at lower energy.

We suspect that the observed signal originates from a cluster of defects of the same type positioned very close to each other. Maxima (0-4) possess similar spectral shapes. As we will show later, their behavior in the external magnetic field is also identical, apart from the feature centered around 1.88 eV (marked with number 2 and green color in fig. 7.24 a).

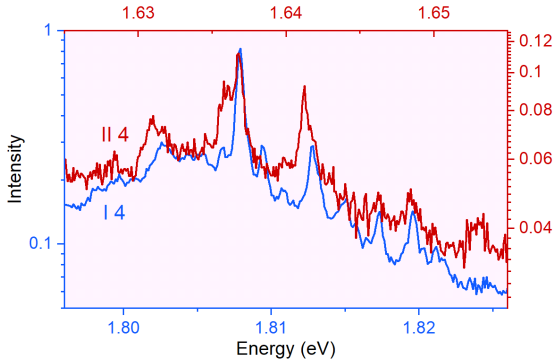

Figure 7.25: Overlaid spectra show ZPL number 4 (blue) and its corresponding phonon side band (red) number 4, region II. ZPL spectral features are reproduced at lower-energy PSB. This figure follows the markings from Fig. 7.24 a).

The stability of the signal is good, as confirmed by the time-dependent PL measurement (7.24 b). The emitter energy does not diffuse and experiences very little blinking events. The emission was stable throughout the whole experiment period (several days) and after a few external magnetic field sweeps.

Measurements performed in an external magnetic field (Faraday configuration) unveil an anomalous behavior of the color center emission. While slowly sweeping the magnetic field up, at a rate of ∼0.5 mT/s, the signal suddenly drops almost to zero at 0.72 T (fig. 7.26 a). While sweeping the magnetic field back down, the signal appears again at 0.51 T (fig. 7.26 b). By spatially mapping the area we confirmed that the effect is not caused by a spatial shift of the sample. Additionally, the Raman signal from the substrate (∼1893 meV) stays the same with the changing magnetic field. As presented in fig. 7.24 c), apart from the switching behavior, the defect-related emission experiences a spectral shift of ∼1.5 meV.

The external magnetic field at which we observe the switching of the emitter coincides with the magnetic field needed to trigger the spin flop transition in $CrPS_4$. There is no clear consensus as to what is the exact value, as it also depends on the pressure, layer thickness, and temperature. Various reports provide different magnitudes of the external magnetic field

needed for the spin flop transition to occur, varying from ∼0.6 T [160], 0.9 T [157, 161, 290] up to ∼1.2 T [163].

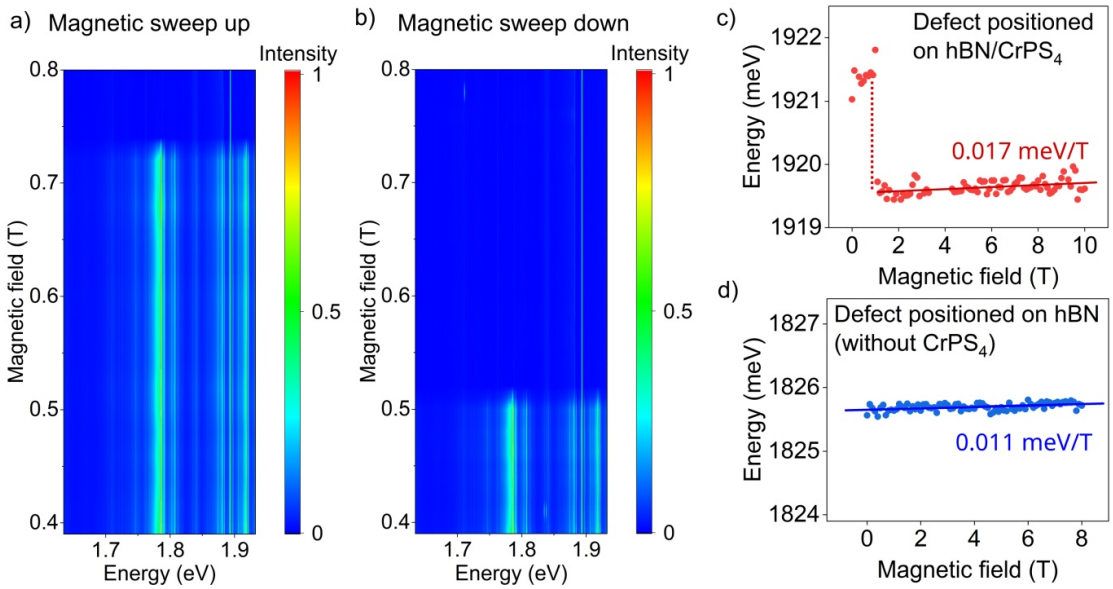

Figure 7.26: PL intensity evolution during a slow (∼0.5 mT/s) magnetic sweep a) up, b) down. c) The anomalous magnetic field dependency of the emitter energy shows a drastic shift at ∼1.1 T during a fast magnetic field sweep. d) A color center positioned at the hBN layer does not show a sharp transition feature.

Results obtained for slow magnetic field sweeps indicate the presence of a hysteresis for a spin flop phase transition in $CrPS_4$. The external magnetic field at which we observed switching off the signal was ∼0.2 T smaller than the one at which we observed switching off of the emitter.

To further characterize the observed effect, we also performed fast sweeps (∼5 mT/s) at a larger range of magnetic fields (0-10 T). Fig. 7.26 c) depicts the energy of the emitter (ZPL ∼1.92 eV) extracted from fitting a lorentzian profile to the PL spectra collected at each external magnetic field. The dependency shows a sudden change of ∼1.5 meV at 1.1 T. At higher magnetic fields, the dependency shows a slight, linear slope of (0.017±0.04) meV/T. We can compare this result to the behavior of an emitter placed in an hBN layer only, presented in fig.

7.26 d). The dependency does not show any sudden changes and cutoffs. However, similarily to the emitter in an hBN/$CrPS_4$ structure, we observe a small slope of (0.011±0.02) meV/T. This result may indicate that some color centers in MOVPE hBN do possess a spin degree of freedom and can interact with the environment purely magnetically. So far, only boron vacancies in hBN (V_B^-) possess well understood optically addressable spin properties [56]. Such defects do not appear in the MOVPE samples spontaneously but need to be artificially created, for instance by neutron irradiation. However, theoretical predictions and initial studies show that other types of defects (ex. carbon-related) can also possess magnetic properties [63, 64]. We can not observe any evident splitting of the emission peaks in our PL results, typically expected for the Zeeman effect. We see a small linear shift at the accuracy limit of the experimental system. We also can not rule out the possibility of micro-mechanical shifts during the wide magnetic sweep, resulting in the emitter energy shifts. Nevertheless, the big switching off and on effect can not be explained as simple sample position changes.

Fig. 7.27 a-b) shows PL intensity maps of the studied emitter for fast, wide-range external magnetic field sweeps. Results confirm the previously observed switching behavior of the defect emission at magnetic fields corresponding to the spin flop phase transition in $CrPS_4$. During these measurements, the switching happened at a slightly higher magnetic field of 1.2 T for sweeping up and 1.1 T for sweeping down. We ascribe this change to much faster magnetic field changes, which is followed by slower switching of magnetic domains in the $CrPS_4$ flake.

One can see, that apart from switching behavior, the signal intensity from the emitter manifests a minimum at ∼4 T (fig. 7.27 a,b). The intensity of the emission possesses a sine-like characteristic, as opposed to the non-changing Raman signal originating from the silicon substrate. Later performed polarization-dependent studies allowed us to fully understand the origin of this effect. Here we present conclusions, while the full explanation is presented in

the next section.

In the used experiment setup, the laser light is directed to the sample without passing additional polarization optics. Hence, the beam going into the superconductive magnet is mostly linearly polarized. A microscope objective focusing the light on the sample is placed right next to it, inside the magnet. The polarization of light passing through a glass in the objective in the external magnetic field is therefore rotated according to the Faraday effect.

Since most hBN defects are usually acting like electric dipoles, the rotation of the polarization of the incident laser light influences their emission intensity. Fig. 7.27c) depicts the intensity profile extracted for the studied defect emission. The dependence shows a rapid cut-off at 1.1 T (spin flop in $CrPS_4$), and then a sine-like behavior consistent with the postulated Faraday effect. To quantitatively determine the observed effect, we studied the laser line reflected from the gold deposited on the sample (inset in fig. 7.27 c). The sine-like characteristic allowed us to determine the magnitude of the Faraday effect occurring in the objective. An external magnetic field of 3.74 T results in the 90° difference between the linear polarization of incoming and detected light.

When we take a look at the intensity maps (fig. 7.27 a,b) and individual spectra collected at various magnetic fields (fig. 7.27 c), we can see an anomalous behavior of ZPL 2, centered around 1.88 eV. At an external magnetic field over the spin flop transition, its intensity is reduced much less than in the case of other ZPLs. In addition, the corresponding excitation becomes destabilized showing signs of blinking and spectral diffusion. In contrast, signals ascribed to other ZPLs and their phonon sidebands (PSB) show a much more stable behavior with little blinking events. This observation leads us to the conclusion, that we observe a cluster of similar defects spatially placed close to each other, but slightly differently reacting to the proximity of $CrPS_4$ flake and its changing magnetic phases.

The exact description of the anomalous effects observed at high magnetic fields remains

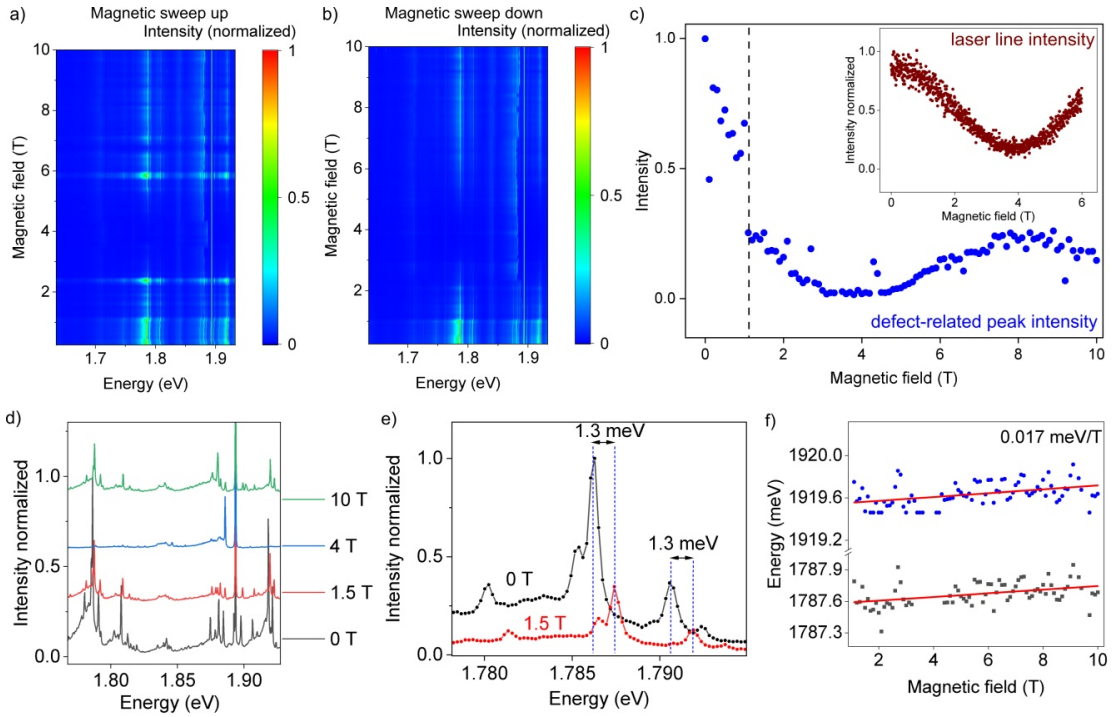

Figure 7.27: Intensity of the PL signal of a studied emitter during a fast (∼5 mT/s) magnetic field sweep in the 0-10 T range for sweeping a) up and b) down. Faraday effect occurring in the glass objective is responsible for the appearance a distinct PL signal minimum around 4 T. c) The hBN emitter intensity (blue) shows a clear cutoff at the external magnetic field corresponding to the spin flop transition in $CrPS_4$. Apart from this feature, the intensity manifests a sine-like behavior originating from the laser polarization rotation by a Faraday effect in the experimental setup. Inset shows the intensity profile of a laser line reflected from a mirror on the sample, showing a sine-like characteristic with a period of 3.74 T. d) Individual PL spectra measured at different magnetic fields below the spin flop transition (black) and over the transition (other colors). e) An energy shift of 1.3 meV is observed between the PL spectra measured at 0 T and 1.5 T f) hBN emitter energy evolution in an external magnetic field extracted from fits to ZPL 1 and PSB 0 (notation form fig. 7.24) shows the same evolution with a slight shift of 0.017 meV/T.

elusive, yet the presented results allow us to formulate possible explanations. We see a drastic decrease in the signal intensity and an energy shift of ∼1.3-1.5 meV for the observed ZPLs (fig. 7.27 e). Additionally, a small linear change ∼0.017 meV/T of emission energy is detected (fig. 7.27) for all (except the anomalous ZPL 2) emitters. If we extrapolate these changes to the values of ∼1.3-1.5 meV observed during the spin flop transition, we obtain

effective fields as large as 80-90 T necessary to trigger such changes. Although hard to obtain in a large-scale laboratory setting, such magnetic field magnitudes are not extraordinary in the world of 2D magnets, on a nanoscale. For example, such fields were predicted for the proximity effect in $CrBr_3/MoS_2$ heterostructures [291]. On the other hand, changes of the local electric field are known to cause switching off and darkening of the emitters in hBN [66, 69–71, 276, 292]. These effects are usually explained as photo-doping [263] or charging (saturation) happening in the charge trap sites [69]. Such a mechanism is well described in graphene/hBN heterostructures [69, 70]. The Fermi level of graphene is tuned by applying the voltage, which changes the charge state of a defect, and eventually causes its darkening or deactivation. Undoubtedly, our structure consisting of a $CrPS_4$ flake and an hBN layer with an embedded color center strongly interacts via strain, mechanical shifts, and/or changes of local magnetic and electric fields. In the next section, we further explore the possibility of electrically tuning the defect-related light emission.

Impact of electric field

We studied whether the emission from the color centers found in our samples can be tuned by applying a voltage. In order to do so, we glued samples described in 7.2.1 section using silver paste to a sapphire substrate, and then glued the sapphire to the cold finger of the cryostat (fig. 7.28). Such a configuration allowed us to backgate the sample, without contacting it to the grounded cold finger. A piece of sapphire provided electrical insulation while offering good thermal conductivity. We cooled the samples to 5 K and performed PL mapping (633 nm laser excitation) in the areas between contacts to find light emitters. We tested 6 devices and found only 4 stable emitters close to the contacts. Then, we measured photoluminescence as a function of the voltage applied parallel and perpendicularly to the sample. The results for one of the studied defects (perpendicular configuration) are shown in fig. 7.28b).

None of the points manifested any relationship between the applied voltage and the optical response. Either the found defects were not sensitive to the electric field, the applied voltage was too small, or the created heterostructures did not have a good electrical contact. ∼90 nm thick layer of SiO_2 prevented us from applying higher voltage in the backgate configuration to avoid a short circuit. The fabrication process of the heterostructures should also be better optimized to ensure good electrical contacts. It can be achieved for example by adding graphene layers to the structure to serve as back and top gates.

Nevertheless, metallic contacts unexpectedly turned out to be very useful during measurements in the magnet. In the used configuration, a sample preview can be done only with the defocused laser light (fig. 7.28 c). Then, only the edges of the flakes can be seen, and finding the desired spot on the sample is extremely challenging. In our measurements well-reflecting electrical contacts served as markers of the position on the sample, which, combined with previously collected optical images made finding the specific position on the sample relatively easy.

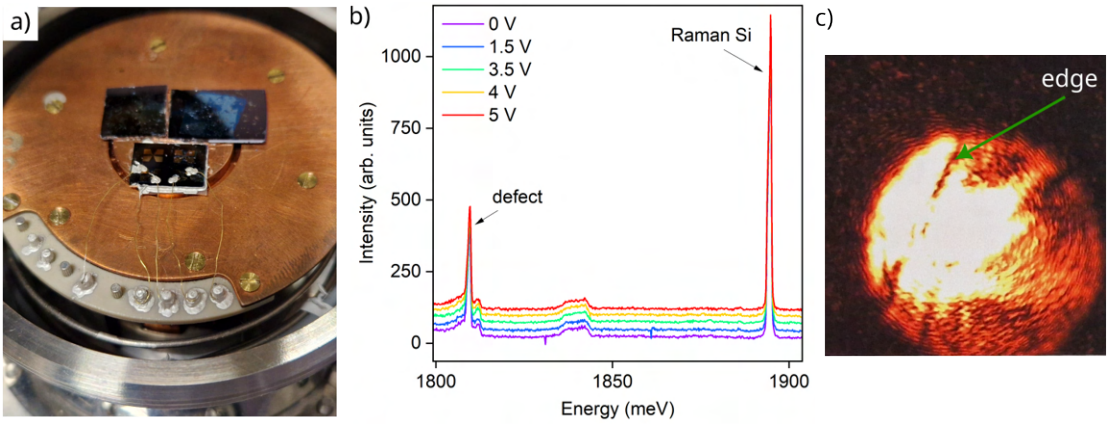

Figure 7.28: a) A photo of an electrically contacted sample glued into the cryostat. b) PL spectra of an exemplary defect show no changes for different applied voltages. c) A screenshot of the available imaging by a defocused laser in the magnet. In the setup, only the edges of the flakes are visible.

At the time of measuring external magnetic field dependencies for the emitter whose behavior correlated with the spin flop transition in $CrPS_4$, we were not able to fully explain the signal fading and around 4 T (fig. 7.27) other effects. We decided to complement the studies by performing polarization-dependent measurements. In the meantime, the studied sample has changed dramatically due to the flattening of hBN layers, which deactivated the studied emitters. Eventually, measurements were performed on previously described samples with electrical contacts.

In the initial experiments, we placed a half-waveplate (HWP or $\lambda/2$ waveplate) behind the beam splitter as depicted in fig. 7.29 (configuration A). Light polarization coming from the laser was additionally corrected by a linear polarizer. The polarizers were positioned relative to each other to maximize the signal (reflected laser line). The HWP mounted behind the beam splitter provided the rotation of polarization of both: excitation and detected beams, mimicking the rotation of the sample.

We collected PL spectra of different defects and of $CrPS_4$ flakes as a function of HWP rotation. We fitted the Lorentzian profile to the Raman signal from silicon and $CrPS_4$, as well as several defect-related peaks. Fig. 7.30 shows the polarization dependencies at various external magnetic fields for silicon Raman signal and an exemplary hBN emitter. Labels on the radial axis of the graphs correspond to the doubled angle of the physical rotation angle of HWP (physical rotation of HWP of 45° corresponds to the 90° rotation of light polarization).

The polarization dependency of silicon resembles a four-leaf clover, and its intensity does not change as a function of magnetic field. However, the magnetic field evolution of the hBN emitter shows more complicated behavior. At 0 T it resembles an '8' with two pronounced

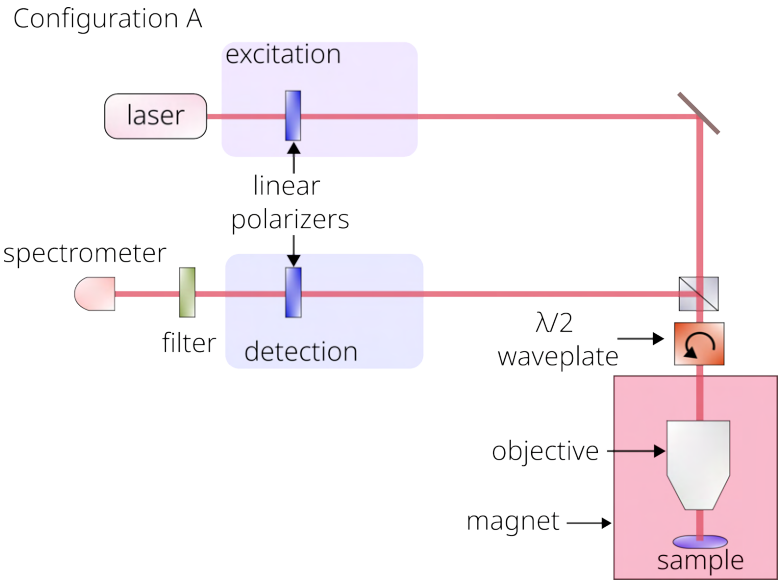

Figure 7.29: Schematic illustration of polarization setup A. Half waveplate is positioned behind the beamsplitter providing the rotation of the polarization of light exciting and detected from the sample.

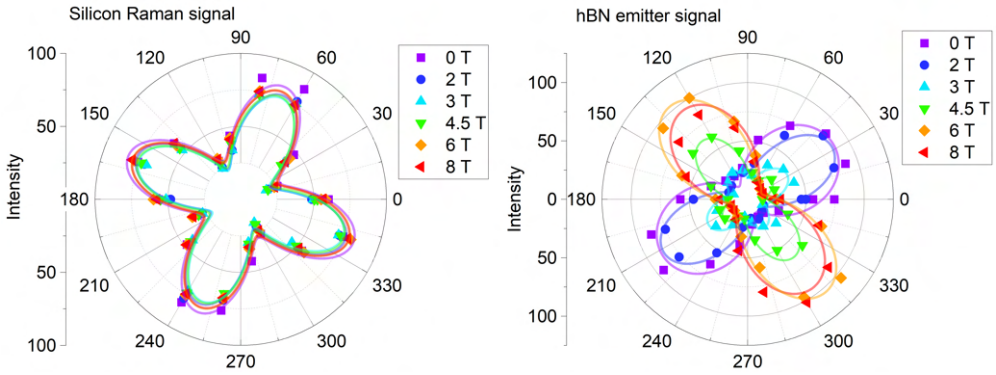

Figure 7.30: External magnetic field evolution of signal intensity as a function of doubled HWP (configuration A) rotation.

maxima. With a rising magnetic field, the intensity of the signal decreases, and at ∼3-4 T the signal resembles an uneven four-leaf clover. At higher magnetic fields we again observe an '8', this time rotated by 90 degrees in relation to the one recorded at 0 T.

To better understand the observed effect we decided to perform measurements in a different configuration granting us independent control of light polarization at excitation and

detection (fig. 7.31). In experiment configuration B one of the HWPs (positioned in the excitation part of the setup) was physically rotated in 0-180° range. Another HWP (positioned in the detection part of the setup) was fixed at one of two positions: at 60° or 105° (these specific angles come from the scale on the mount). The positions correspond to two perpendicular polarizations of light.

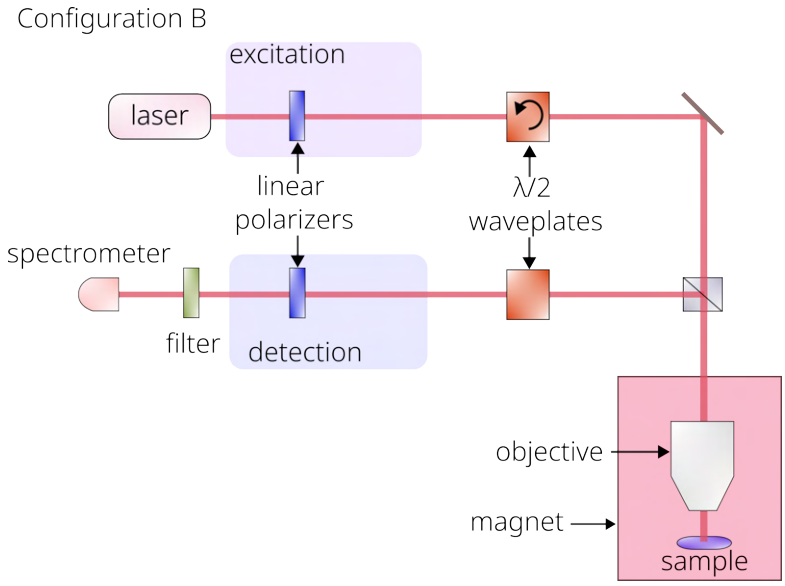

Figure 7.31: Schematic illustration of polarization setup B. One half waveplate is positioned in the 'excitation' part of the setup, and during measurements is physically rotated in 0-180° range, which corresponds to 360° polarization rotation. Another half waveplate is positioned in the 'detection' part of the setup and set in two fixed positions (60° and 105°) physically rotated by 45°.

We performed measurements at various external magnetic fields collecting Raman signals from the substrate and magnetic flakes, as well as several light-emitting defects. For each point, we collected full angular dependency by rotating 'excitation' HWP at 0-180° range, at both settings (60° and 105°) of the 'detection' HWP.

Fig. 7.32 shows Raman spectra collected at 0 T, for two 'detection' HWP settings. The analyzed peaks of different symmetries are marked following the notation found in [287, 288]. Spectra were collected at 10 K, with a 514 nm excitation laser. The signal was collected

from a bulk (>100 nm thick) $CrPS_4$ flake, that was not covered by an hBN layer to avoid background and additional signals.

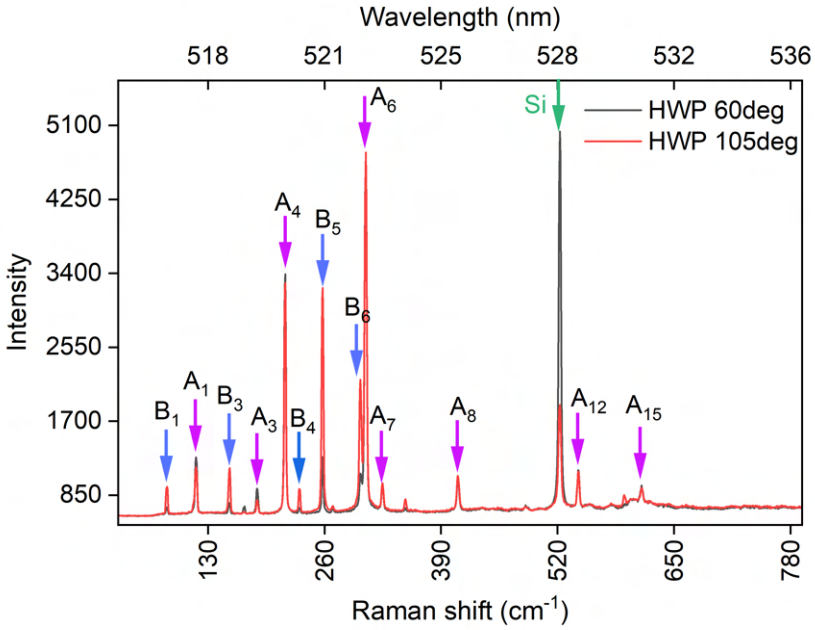

Figure 7.32: Raman spectra of a bulk flake of $CrPS_4$ collected at 10 K and 0 T. Black and red lines correspond to two settings of HWP positioned at the detection part of the polarization setup. Raman modes are marked with letters corresponding to their symmetry.

Fig. 7.33 show the results of polarization-resolved measurements for Raman $CrPS_4$ signal $\sim$85 cm^{-1} corresponding to the B_1 peak [287]. Polar plots present the intensity of the peak extracted from the Lorentzian profile fitting to Raman spectra. Orange points correspond to the 60°, while green points to 105° setting of the 'detection' HWP.

Angular dependencies recorded for two 'detection' HWP settings form two eight-like features rotated by 90°. We also see that the external magnetic field does not change the intensity nor angular dependency of the studied mode. The same result (no changes in the external magnetic field) was obtained for the Raman signal from the silicon.

Analogously, we performed analysis for peaks with symmetry A. Fig. 7.34 depicts po-

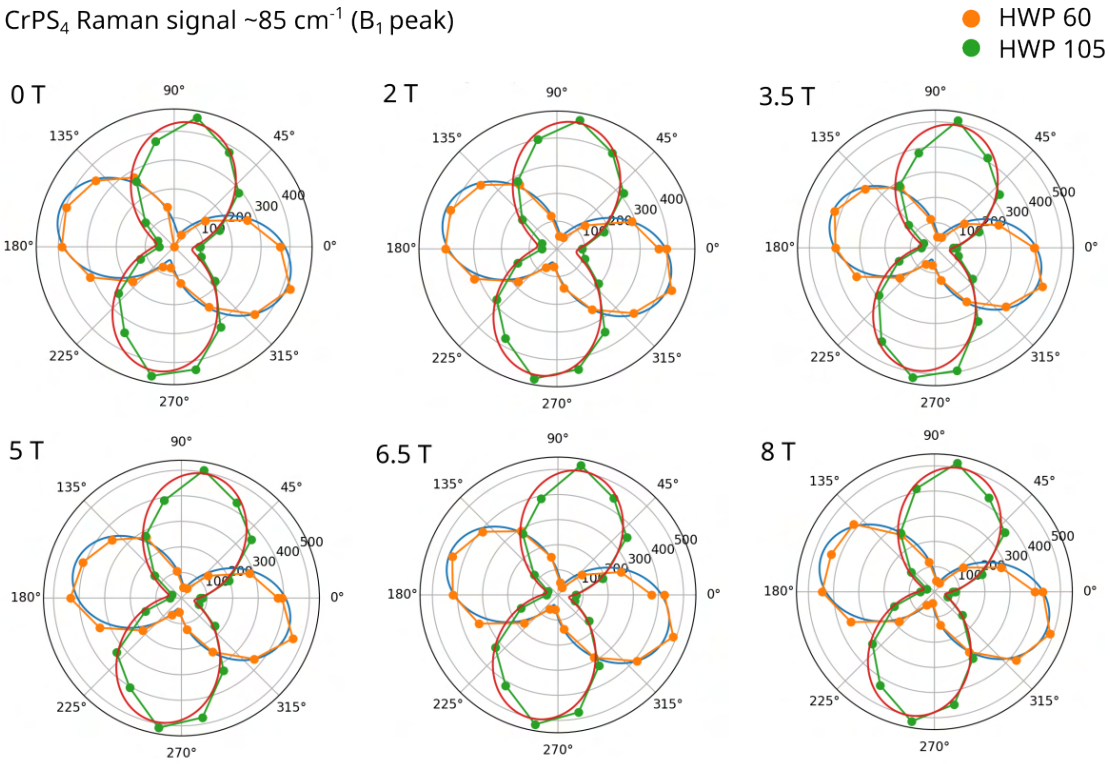

Figure 7.33: Polar plots of the intensity of $CrPS_4$ Raman peak B_1, collected at various external magnetic fields. The angular scale of the plots corresponds to the doubled physical rotation angle of the HWP positioned at the excitation part of the setup. Experimental data are presented as orange or green points connected with lines, while red and blue solid lines show the results of fitting.

lar plots for $CrPS_4$ Raman signal at $\sim$117 cm^{-1} corresponding to A_1 peak. Dependencies recorded for two 'detection' HWP settings also possess two maxima reminiscent of an 'eight', however they are rotated in relation to each other by different angles. Measurements at external magnetic fields unveil an intriguing evolution. Angular dependencies rotate and change their intensities. The change of the external magnetic field of $\sim$3.5-4 T, rotates the angular dependency by 90°. For example, we can compare the green points in fig. 7.34 at 0 T and 3.5 T. An 'eight' like characteristic at 0 T is almost aligned with the 45°-225° axis. At 3.5 T, the 'eight' like characteristic is rotated and aligned with the 135°-315° axis.

This observation, combined with the previously described signal fading (fig. 7.27), led

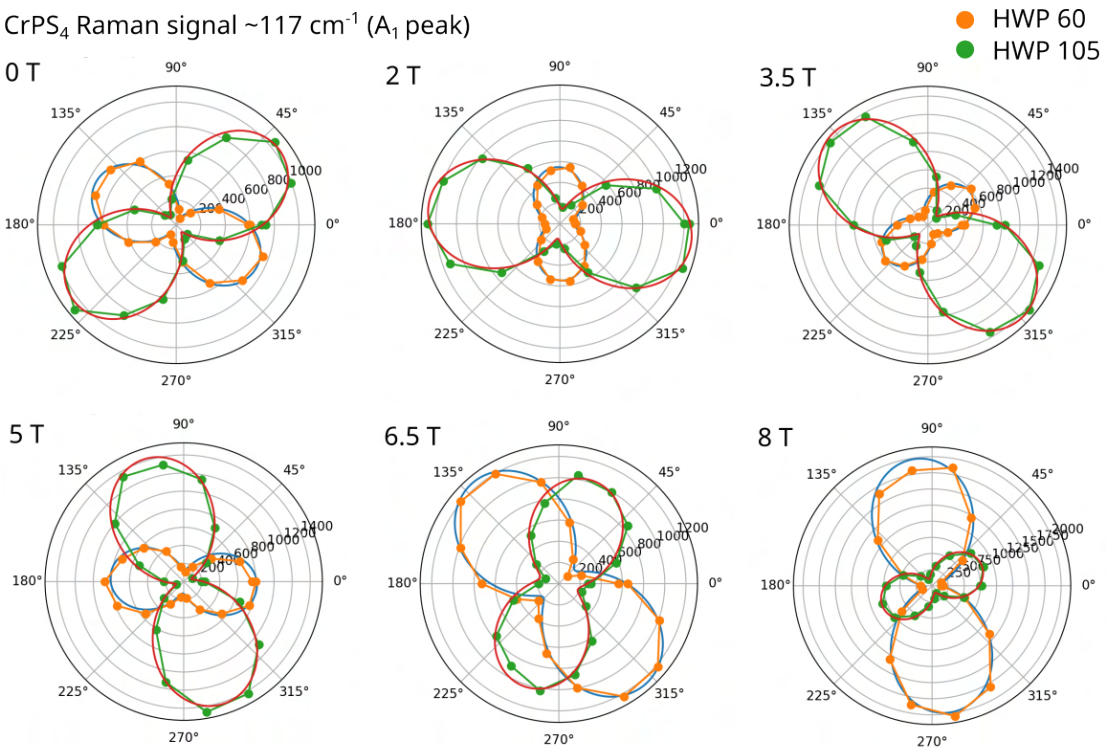

Figure 7.34: Polar plots of the intensity of $CrPS_4$ Raman peak A_1, collected at various external magnetic fields. The angular scale of the plots corresponds to the doubled physical rotation angle of the HWP positioned at the excitation part of the setup. Experimental data are presented as orange or green points connected with lines, while red and blue solid lines show the results of fitting.

us to an explanation related to the Faraday effect. In our setup, light passes through a glass objective. According to the Faraday's effect, the linear polarization of light is rotated by an angle $\beta = \nu B d$, where ν is the Verdet constant characteristic for the material, B is the external magnetic field, d is the distance that light travels in a material. In our configuration, the external magnetic field does change its sign, so light reflected from the sample would be further rotated in the same direction.

Mathematically we can describe measurements in configuration B as follows. The inci-

dent light vector:

$$e_i = \begin{pmatrix} sin(\theta) \\ cos(\theta) \\ 0 \end{pmatrix},$$

where θ depends on the rotation of 'exciting' HWP. The scattered light vectors correspond to two settings of 'detection' HWP:

$$e_s = \begin{pmatrix} -cos(\gamma) \\ sin(\gamma) \\ 0 \end{pmatrix} \text{ or } \quad e_s = \begin{pmatrix} sin(\gamma) \\ cos(\gamma) \\ 0 \end{pmatrix}.$$

Angle γ is set and depends on the position of 'detection' HWP in relation to the laboratory coordinates. Faraday effect results in the linear polarization rotation and can be written as a rotation matrix:

$$F = \begin{pmatrix} cos(\beta) & -sin(\beta) & 0 \\ sin(\beta) & cos(\beta) & 0 \\ 0 & 0 & 1 \end{pmatrix},$$

where β parameter depends linearly on the external magnetic field B.

Raman tensors for silicon (R_{Si}) and $CrPS_4$ (modes with symmetry A and B) in our experimental configuration can be written as [287]:

$$R_{Si} = \begin{pmatrix} 0 & s & 0 \\ s & 0 & 0 \\ 0 & 0 & 0 \end{pmatrix},$$

$$R_{CrPS_4\ B} = \begin{pmatrix} 0 & f\,e^{i\,\phi f} & 0 \\ f\,e^{i\,\phi f} & 0 & g\,e^{i\,\phi g} \\ 0 & g\,e^{i\,\phi g} & 0 \end{pmatrix}, \quad R_{CrPS_4\ A} = \begin{pmatrix} b\,e^{i\,\phi b} & 0 & d\,e^{i\,\phi d} \\ 0 & c\,e^{i\,\phi c} & 0 \\ d\,e^{i\,\phi d} & 0 & a\,e^{i\,\phi a} \end{pmatrix}.$$

Then, the intensity of the detected light is given by the following formula:

$$I \propto |e_s\,F\,R\,F\,e_i|^2, \tag{7.3}$$

where R is the chosen Raman tensor. After simplifying, we learn that the detected signal intensity does not depend on the magnetic field for Raman tensors without the diagonal elements. As shown below, both the Raman signal from the silicon substrate and from the $CrPS_4$ peaks with B symmetry are not affected by the Faraday effect and do not depend on magnetic field. The intensity of the signal depends only on the specific tensor elements and as a sine squared of the excitation polarization angle. Obtained formulas were fitted to the data presented in fig. 7.33. By solving the equation 7.3 for both of the 'detection' HWP settings we see, that the signals should indeed be rotated by 90° in relation to each other.

$$\text{Raman of silicon}: \quad I_{HWP_{60}} \propto s^2 sin^2(\gamma+\theta), \quad I_{HWP_{105}} \propto s^2 cos^2(\gamma+\theta) \tag{7.4}$$

$$\text{Raman CrPS}_4\text{ B}: \quad I_{HWP_{60}} \propto f^2 sin^2(\gamma+\theta), \quad I_{HWP_{105}} \propto f^2 cos^2(\gamma+\theta) \tag{7.5}$$

Raman modes with A symmetry, are characterized by tensors with diagonal elements. By

simplifying the equation 7.3 for $R_{CrPS_4\ A}$, we obtain much more complicated dependency:

$$\begin{aligned}\text{Raman CrPS}_4\text{ A}: \quad I_{HWP_{60}} \propto 1/4\{&b^2+c^2+(-b^2+c^2)\cos[2(\beta+\gamma)]+\\ &\cos[2(\beta-\theta)]\,(-b^2+c^2+(b^2+c^2)\cos[2(\beta+\gamma)])-\\ &2bc\cos(\phi b-\phi c)\sin(2(\beta-\theta))\sin(2(\beta+\gamma)\}.\end{aligned} \tag{7.6}$$

We see, that the intensity of the signal does not depend on a and d elements of the tensor, which is understandable for our experimental configuration (light propagates perpendicular to the xy sample plane). Parameter β appears in the formula, explaining the influence of the external magnetic field on the measurements. The found intensity of peaks with A symmetry depends on parameters b and c as well as ϕb and ϕc. These results are in agreement with the observation from [287], that only the complex Raman tensor can fully describe $CrPS_4$ modes.

In order to explain the four-fold features observed during measurements in configuration A (fig. 7.30), we need to make minor changes to the mathematical notation. In configuration A, one HWP influences exciting and scattered light simultaneously, hence we can describe both light vectors with the same angle (θ). When we simplify the intensity equation 7.3 for silicon Raman tensor, we get the following: $I_{\text{conf. A}} \propto s^2\sin^2(2\theta)$. On the contrary to the result obtained for experimental configuration B, we get the doubled angle θ, which results in the observation of a four-fold signal.

Simulating the behaviour of modes with symmetry A, leads to results consistent with experimental observations. Parameters b and c are responsible for changing the intensity of the signal in one of two perpendicular directions. If $b = c$, we would observe a circle in the polar plot. Parameters ϕb and ϕc can "squeeze" the observed '8' dependence. Changing parameter β, so changing the external magnetic field, causes the signal to shift from one direction to the

perpendicular direction, by lowering its intensity and changing it to a four-fold feature. The presented model was fitted to the data in fig. 7.30. This analysis shows that it is entirely understandable why the PL and Raman modes with A symmetry almost vanish in a magnetic field. This is a result of the rotation of the light polarization induced by the Faraday effect, while at the same time, the Raman intensity of silicon remains completely unaffected. Although this behavior may initially appear counterintuitive, it is important to keep in mind, as it can easily give rise to misinterpretations.

The described simulations and visualizations (Wolfram Mathematica script) can be found in additional materials attached to this work in the file: *Chapter7_modelling.nb*.

Polarization-resolved measurements of hBN emitters

Fig. 7.35 shows PL spectra collected on the edge of a thin $CrPS_4$ flake covered by hBN. Three defect-related peaks were chosen for further analysis. The chosen peaks were characterized by a stable PL emission and were visible even at a high external magnetic field.

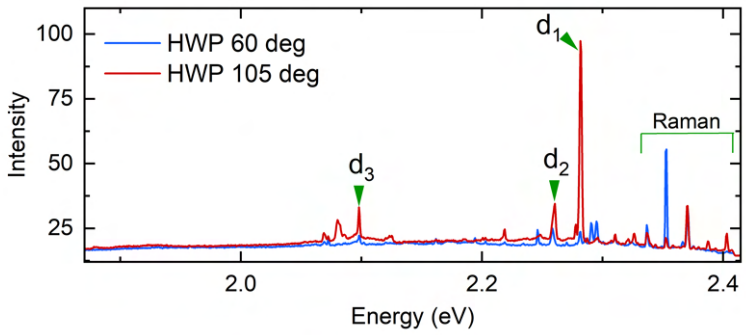

Figure 7.35: PL spectra collected at 0 T (10 K, 514 nm laser) showing three defects for which polarization-resolved measurements in experimental configuration B at various external magnetic fields were made.

Similar to the $CrPS_4$ polarization-resolved Raman characteristic presented before, Lorentzian profiles were fitted to the spectra measured at various magnetic fields with two different detec-

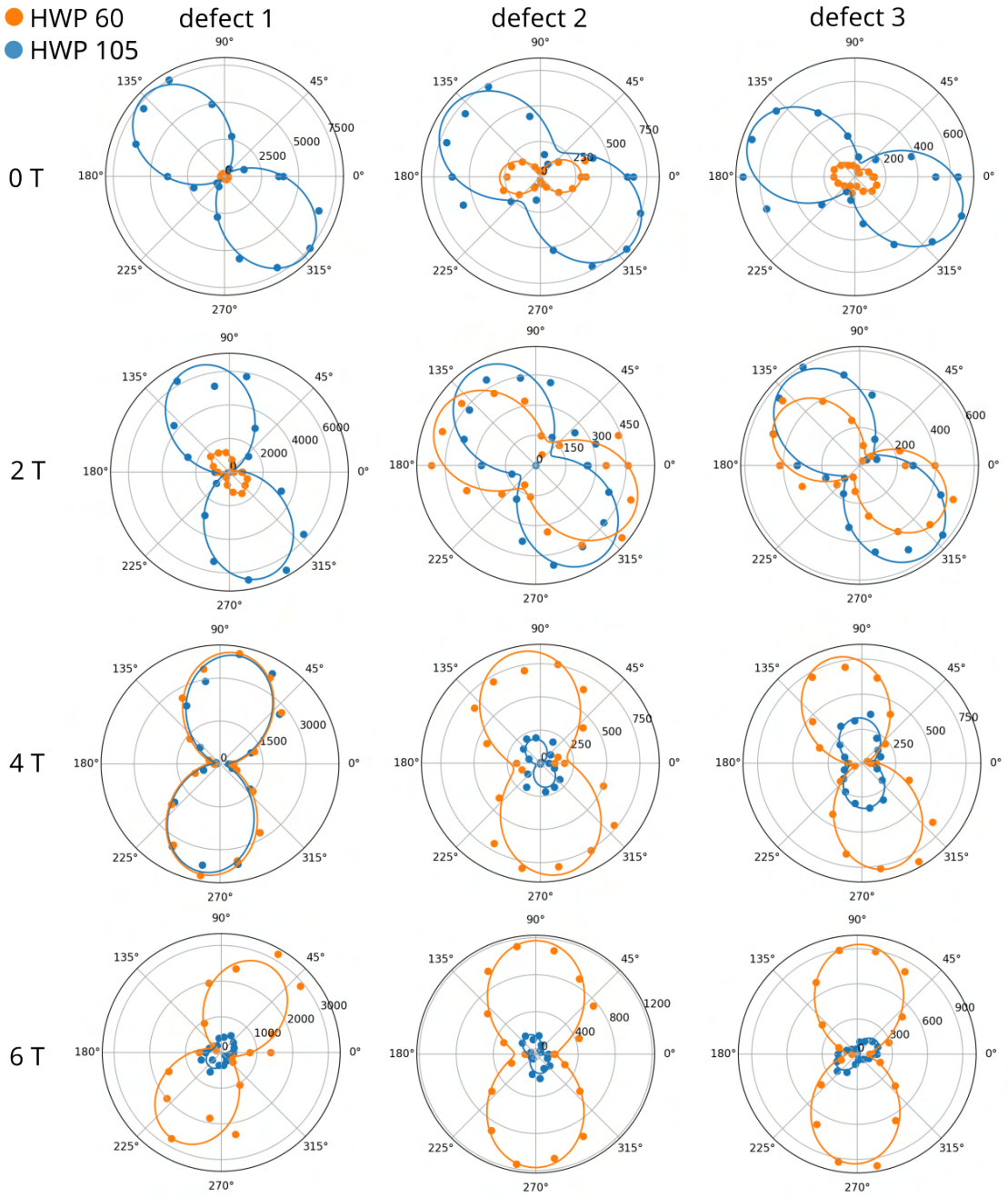

Figure 7.36: Polar plots of the intensity of hBN emitters signal, collected at various external magnetic fields. The angular scale of the plots corresponds to the doubled physical rotation angle of the HWP positioned at the excitation part of the setup (experimental configuration B).

tion half waveplate configurations (marked as HWP 60 and HWP 105). Fig. 7.36 shows the magnetic field evolution of the defect-related emission intensity as a function of excitation light polarization. The behavior of the studied emission is similar to that of $CrPS_4$ Raman modes with A symmetry and can be successfully described by a tensor belonging to the C_2 group (like the previously used $R_{CrPS_4\ A}$). A possible explanation for the possibility of applying Raman formalism to the defect-related PL peaks may be the resonant excitation. In such a scheme, we stimulate directly the defect absorption bands and collect the intra-center luminescence. Similarly to the polarizability consideration in the Raman scattering case, the defect state absorption magnitude depends on the polarization of light. Then, after relaxation to the state from which the emission occurs, the symmetry of this state determines the emitted light polarization.

At zero external magnetic field, the contribution of the peak intensity corresponding to the HWP 60 detection mode is significantly smaller than the one for the HWP 105 detection mode, indicating a big difference in the values between b and c tensor elements, with one of them being close to zero. The recorded angular dependencies are similar for defects 2 and 3, indicating that they may originate form the same defect center or two closely placed, similarly rotated defects. The small discrepancies between the results may be due to inaccuracies of the measurement setup or the instability of the system. Lastly, we can not rule out the observation of a cluster of defects.

The recorded polar dependencies and the presented description indicate that defects found in studied epitaxial hBN manifest dipole-like transitions, which stands in agreement with other reports [293, 294].

7.5.3 Discussion and conclusions

In this chapter, we explored the interaction between color centers in epitaxial hBN and 2D magnets ($CrBr_3$, $CrPS_4$). We presented our studies from the fabrication process, through temperature and external magnetic field measurement, to the polarization-resolved spectroscopic characterization.

Our efforts resulted in the observation of two main effects. One was a change in the hBN defect-related emission energy, with a clear cut-off at the temperature corresponding to the phase transition temperature in a 2D magnet. We observed the effect for both of the studied 2D magnets at points positioned at the edges of the flakes. In the case of $CrBr_3$, the energy shift was $\sim$1 meV, while for $CrPS_4$, it was $\sim$1.5 meV.

The second effect included the sudden change in energy and a drastic intensity drop in hBN defect-related emission at an external magnetic field corresponding to the spin-flop transition in the used 2D magnet ($CrPS_4$). The observed energy shift ($\sim$1.3-1.5 meV) was similar to that recorded in the temperature-dependent studies.

Below, we discuss various explanations of the described phenomena. A direct magnetic interaction between spins in the defect states and a 2D magnet is the first explanation that comes to mind when considering systems consisting of magnetic materials. However, in high external magnetic fields, we do not observe any evident broadening or splitting of the emission peaks. Therefore, the recorded energy shift of the defect-related spectrum rather indicates a small direct magnetic interaction. Our observation is consistent with other reports showing that most color centers found in hBN are insensitive to the applied magnetic fields [295]. However, the magnetic interaction cannot be completely ruled out. In addition to a sudden energy shift during a spin-flop phase transition, we also observed a small, linear change in the defect-related emission energy ($\sim$0.017 meV/T). These small changes

were recorded for hBN defects found in the vicinity of 2D magnet flakes, as well as for those found in just the hBN layer. In this case, we need to be careful with the interpretation, as the experimental limitations allow for the possibility that the effect is an apparatus-related result. However, the observation was repeated on several different defects. Assuming that the magnetic interaction is responsible for the changes in the defect-related emission energy, we could extrapolate the results to a sudden energy shift observed during a phase transition. To achieve the change of $\sim$1.5 meV, the effective magnetic field would have to change by $\sim$90 T. According to the literature, such a high value is not impossible for local fields in the vicinity of 2D magnets [291].

Other possible explanations of the observed effects include more intricate interactions with the local electric field and strain. Temperature-dependent studies show that the energy shifts is the highest at the edges of the flakes. In our analysis, we lean towards the conclusion that the described result originates from the mechanical changes in a 2D magnet appearing during the magnetic phase transition, which induces strain in an hBN layer. We propose that the shrinking and expanding of an underlying 2D magnet with changing temperature leads to substantial stress in the heterostructure. This, in turn, leads to a strain-induced shift in the hBN defect-related emission energy. Such stress-induced changes were also reported in the literature, for example, in hBN layers suspended on microspheres [277].

Our analysis of the hBN defect-related emission energy aligns with the results extracted from the Raman signal of the 2D magnet, which can be used to extract the temperature of the paramagnetic-ferromagnetic phase transition in $CrBr_3$ [279]. It is worth noting, that the energy shift magnitude during the phase transition was more than an order of magnitude bigger for the hBN emitter ($\sim$1 meV) than for the $CrBr_3$ Raman signal ($\sim$0.1 meV). Our results show, that tracking changes of ZPL energy of defects in hBN can provide information about the phase of an encapsulated material.

The studies are complemented by temperature-dependent characteristics of $CrPS_4$ Raman modes, as well as polarization-resolved optical characterization of the 2D magnet Raman modes and color centers emission at various magnetic fields. The performed measurements allowed us to understand processes present in the experimental setup, as well as shed light onto the properties of epitaxial hBN defects.

The presented results definitely do not exhaust the topic of the interaction of hBN defects with 2D magnets, but rather scratch its surface, setting the direction for further research. Characterization with other excitation laser energies and in different setup geometries should be performed to learn more about the origin of the color centers. Another interesting direction would be to create the defects deterministically, for example by neutron or e-beam irradiation, to control their exact position.

Some of the results presented in this chapter were written down in the form of a manuscript, which will soon be submitted to the high-impact scientific journal.

8

Summary and conclusions

In this thesis, we have explored the applications of epitaxial hexagonal boron nitride at two scales: nano-, for its potential in sensing, and macro-, as a substrate for other ultrathin materials.

For the large-scale part of the work, we presented a combined growth technique in which we used MOVPE to grow large-area hBN layers, followed by an MBE growth of $MoSe_2$. The performed optical spectroscopy, morphology, and structural studies revealed a high uniformity of the samples over the whole area of 2" wafers. The used epitaxial hBN spacer improved

the optical quality of $MoSe_2$ layers, as evidenced by narrow and well-resolved excitonic lines in low-temperature photoluminescence measurements.

Additionally, we have developed a wet exfoliation scheme to transfer large-area ($\sim$ cm^2) hBN layers onto other substrates, like Si/SiO_2. The process allowed for better morphology imaging as it removed the hBN wrinkles that typically appear during the MOVPE growth. We found that such a transferred material constitutes an even better substrate for the further MBE growth of $MoSe_2$. A large number of edges found in epitaxial hBN provided uniformly spread nucleation centers that promoted the growth of mostly monolayer $MoSe_2$, in contrast to the weaker nucleation and a higher ratio of multilayer material obtained for the MBE growth on hBN flakes exfoliated from bulk material.

The growth on top of epitaxial hBN transferred on a Si/SiO_2 substrate allowed us to electrically contact the structure, which resulted in electrical control of the $MoSe_2$ charge carrier concentration as evidenced by a change of the neutral to charged exciton ratio. Our results deliver a scalable method of producing high-quality single layers of $MoSe_2$. Further optimization of the proposed approach may result in establishing large-area epitaxial hBN as a template for the growth of various 2D materials, including other TMDC representatives, as well as 2D magnets.

On the nanoscale, we explored the interaction between point defects in epitaxial hBN and 2D magnets like $CrPS_4$ and $CrBr_3$. We presented optical spectroscopy studies of the heterostructures conducted at various temperatures, and in high external magnetic fields. We performed a statistical analysis of the light emission from the defects that are inherently present in the epitaxial hBN samples. The recorded photoluminescence features correspond to the zero-phonon lines and phonon sidebands typically observed for carbon-related defects in hBN.

In our work, we wanted to study whether the color centers found in epitaxial hBN can be

used as local sensors integrated into the heterostructure. Indeed, we observed that the optical response from the hBN layers can be correlated with the phase of the underlying 2D magnet. By varying the temperature of the samples, we observed a change in the energy of the defect-related photoluminescence emission, showing a clear cut-off at the temperature corresponding to the Néel ($CrPS_4$), or Curie ($CrBr_3$) temperature of the 2D magnet. During the measurements in an external magnetic field, we reported a sudden intensity drop and energy shift of the defect-related photoluminescence at the magnetic field corresponding to the spin-flop transition in $CrPS_4$. Possible explanations for the experimental results included mechanical strain, electric charging, and direct magnetic interaction. We complemented the hBN/2D magnet heterostructures studies by performing polarization-resolved measurements, which allowed us to understand the behavior of the used setup, as well as shed light onto the symmetry properties of the 2D magnet and hBN defects.

This work addresses two current research trends from the world of ultrathin materials. On the one hand, it focuses on basic research, exploring fundamental properties of light-emitting point defects in a wide bandgap semiconductor. Such light sources could find use in quantum technologies. The sensitivity of the defect-related light emission to even small, nanoscale environmental changes can be utilized to develop future nanosensors of magnetic field or strain integrated into the device.

On the other hand, this work delves into the optimization of large-area growth methods of high-quality monolayers, addressing the size, uniformity, and reproducibility limits. Such an approach is indispensable for any scalable use of 2D materials in real-life devices.

We hope that further studies in the presented macro-, and nano- directions will result in connecting these two worlds to realize novel functional applications.

[This page intentionally left blank]

List of publications

Publications and preprints directly related to this thesis

1. **K. Ludwiczak**, A. K. Dąbrowska, J. Kucharek, J. Rogoża, M. Tokarczyk, R. Bożek, M. Gryglas-Borysiewicz, T. Taniguchi, K. Watanabe, J. Binder, W. Pacuski, and A. Wysmołek, "Large-Area Growth of High-Optical-Quality $MoSe_2$/hBN Heterostructures with Tunable Charge Carrier Concentration", ACS Applied Materials & Interfaces **16**, 49701–49710 (2024)

2. **K. Ludwiczak**, A. K. Dąbrowska, J. Binder, M. Tokarczyk, J. Iwański, B. Kurowska, J. Turczyński, G. Kowalski, R. Bożek, R. Stępniewski, W. Pacuski, and A. Wysmołek, "Heteroepitaxial Growth of High Optical Quality, Wafer-Scale van der Waals Heterostrucutres", ACS Applied Materials & Interfaces **13**, 47904–47911 (2021)

3. **K. Ludwiczak** et al., "Color centers in large-area hBN as local sensors atomic scale magnetic properties", (2025) *in preparation*

Other publications

3. J. Rogoża, J. Iwański, **K. Ludwiczak**, B. Furtak, A. K. Dąbrowska, M. Tokarczyk, J. Binder, and A. Wysmołek, "Mitigation of Delamination of Epitaxial Large-Area Boron Nitride for Semiconductor Processing", (2025) *in review*

4. I. Niehues, D. Wigger, K. Kaltenecker, A. Klein-Hitpass, P. Roelli, A. K. Dabrowska, **K. Ludwiczak**, P. Tatarczak, J. O. Becker, R. Schmidt, M. Schnell, J. Binder, A. Wysmołek, and R. Hillenbrand, "Nanoscale resolved mapping of the dipole emission of

hBN color centers with a scattering-type scanning near-field optical microscope", Nanophotonics, 1–8 (2025)

5. J. Rogoża, J. Binder, K. V. Voronin, I. Niehues, **K. Ludwiczak**, A. K. Dąbrowska, M. Tokarczyk, R. Bożek, A. Y. Nikitin, R. Hillenbrand, R. Stępniewski, and A. Wysmołek, "Polarisation-dependent Raman enhancement in hexagonal boron nitride membranes", Nanoscale **17**, 3053–3060 (2025)

6. J. Binder, A. K. Dąbrowska, M. Tokarczyk, **K. Ludwiczak**, R. Bożek, G. Kowalski, R. Stepniewski, and A. Wysmołek, "Epitaxial Hexagonal Boron Nitride for Hydrogen Generation by Radiolysis of Interfacial Water", Nano Letters **23**, 1267–1272 (2023)

7. **K. Ludwiczak**, E. Łacińska, J. Binder, I. Lutsyk, M. Rogala, P. Dąbrowski, Z. Klusek, R. Stepniewski, and A. Wysmołek, "Impeded phase transition in 1T-TaS_2: Thermoelectric fingerprint of long-lived mixed states", Solid State Communications **305**, 113749 (2020)

Conferences contributions

Oral contributions

1. 11th Asia-Pacific Workshop on Widegap Semiconductors (APWS 2024), October 2024, Busan, South Korea, contributed talk: *Optically Active Spin Defects in Epitaxial Hexagonal Boron Nitride*
2. International Symposium on Imaging, Sensing, and Optical Memory (ISOM"24), 2024, Himeji, Japan, contributed talk: *Spin Defects in Hexagonal Boron Nitride: Towards Nano-Sensing*
3. International Symposium on Imaging, Sensing, and Optical Memory (ISOM"23), 2023, Takamatsu, Japan, contributed talk: *Hexagonal Boron Nitride - a Two Dimensional Platform for Quantum Sensing*
4. Compound Semiconductor Week, 2023, Jeju, South Korea, contributed talk: *Optical Studies of Color Centers in Epitaxial Hexagonal Boron Nitride*
5. Graphene and other 2D materials, 2022, Łódź, Poland, contributed talk: *Proximity Effect of Two-dimensional Magnets on Hexagonal Boron Nitride: Optical Studies*
6. Graphene Week, 2022, Munich, Germany, contributed talk: *Scaling up van der Waals heterostructures – a combined heteroepitaxial approach*
7. Cleo Pacific Rim, 2022, Sapporo, Japan and on-line, contributed talk: *Probing the emission from hexagonal boron nitride with 2D magnets*
8. MRS Fall Meeting, 2021, Boston, USA and online, contributed talk: *Wafer-Scale Epitaxial $MoSe_2$ on Epitaxial hBN—A Combination of MBE and MOVPE*

9. Graphene and other 2D materials, 2021, Wrocław (online), Poland, contributed talk: *High optical quality of $MoSe_2$ monolayers grown on two-inch wafers of epitaxial hBN: a combined MBE/MOVPE approach"*

10. 49th International School and Conference on the Physics of Semiconductors "Jaszowiec", 2021, online, Poland, contributed talk: *Optical properties of $MoSe_2$ layers grown on 2" h-BN templates a combined MBE/MOVPE approach*

11. Compound Semiconductor Week, 2021, Stockholm, Sweden and online, contributed talk: *Optical Studies Of Wafer-scale Heteroepitaxial Monolayer $MoSe_2$*

Poster contributions

1. Jaszowiec 2024, Szczyrk, Poland, poster: *Electrical control of optical properties of MBE $MoSe_2$/MOVPE hBN structures*

2. ICNS -14, Fukuoka, Japan, poster: *Growth of high optical quality $MoSe_2$ monolayers on epitaxial hBN*

3. Jaszowiec 2023, Szczyrk, Poland, poster: *Investigating the Proximity Effect in h-BN/2D Magnet Heterostructures*

4. Single Photon Workshop, 2022, Seoul, South Korea, poster: *Towards Magnetically Addressed Emission from Defects in Hexagonal Boron Nitride for Single Photon Sources*

Bibliography

[1] A. Robert, P. K. Barkoutsos, S. Woerner, and I. Tavernelli, "Resource-efficient quantum algorithm for protein folding", npj Quantum Information **7**, 1–5 (2021).

[2] A. Gottscholl, M. Diez, V. Soltamov, C. Kasper, D. Krauße, A. Sperlich, M. Kianinia, C. Bradac, I. Aharonovich, and V. Dyakonov, "Spin defects in hBN as promising temperature, pressure and magnetic field quantum sensors", Nature Communications **12**, 1–8 (2021).

[3] K. S. Novoselov, A. K. Geim, S. V. Morozov, D. Jiang, Y. Zhang, S. V. Dubonos, I. V. Grigorieva, and A. A. Firsov, "Electric field in atomically thin carbon films", Science **306**, 666–669 (2004).

[4] K. S. Novoselov, A. Mishchenko, A. Carvalho, and A. H. Castro Neto, "2D materials and van der Waals heterostructures", Science **353**, aac9439 (2016).

[5] S. Haastrup et al., "The computational 2d materials database: high-throughput modeling and discovery of atomically thin crystals", 2D Materials **5**, 042002 (2018).

[6] S. Strite, "GaN, AlN, and InN: A review", Journal of Vacuum Science & Technology B: Microelectronics and Nanometer Structures **10**, 1237 (1992).

[7] S. Nakamura, T. Mukai, and M. Senoh, "Candela-class high-brightness InGaN/AlGaN double-heterostructure blue-light-emitting diodes", Applied Physics Letters **64**, 1687–1689 (1994).

[8] D. J. Elliott, *Ultraviolet laser technology and applications* (Academic Press, 1995), p. 350.

[9] M. Wraback, H. Shen, J. C. Carrano, T. Li, J. C. Campbell, M. J. Schurman, and I. T. Ferguson, "Time-resolved electroabsorption measurement of the electron velocity-field characteristic in GaN", Applied Physics Letters **76**, 1155–1157 (2000).

[10] R. Zedlitz, M. Heintze, and M. B. Schubert, "Properties of amorphous boron nitride thin films", Journal of Non-Crystalline Solids **198-200**, 403–406 (1996).

[11] H. Miyamoto, M. Hirose, and Y. Osaka, "Structural and electronic characterization of discharge-produced boron nitride", Japanese Journal of Applied Physics **22**, L216–l218 (1983).

[12]C. B. Samantaray and R. N. Singh, "Review of synthesis and properties of cubic boron nitride (c-BN) thin films", International Materials Reviews **50**, 313–344 (2005).

[13]L. Vel, G. Demazeau, and J. Etourneau, "Cubic boron nitride: synthesis, physicochemical properties and applications", Materials Science and Engineering: B **10**, 149–164 (1991).

[14]M. A. El Khakani and M. Chaker, "Physical properties of the x-ray membrane materials", Journal of Vacuum Science & Technology B: Microelectronics and Nanometer Structures Processing, Measurement, and Phenomena **11**, 2930–2937 (1993).

[15]Y. Liu, G. (Zhan, Q. Wang, D. He, J. Zhang, A. Liang, T. E. Moellendick, L. Zhao, and X. Li, "Hardness of Polycrystalline Wurtzite Boron Nitride (wBN) Compacts", Scientific Reports **9**, 1–6 (2019).

[16]C. Chen, D. Yin, T. Kato, T. Taniguchi, K. Watanabe, X. Ma, H. Ye, and Y. Ikuhara, "Stabilizing the metastable superhard material wurtzite boron nitride by three-dimensional networks of planar defects", Proceedings of the National Academy of Sciences of the United States of America **166**, 11181–11186 (2019).

[17]K. Momma and F. Izumi, "VESTA 3 for three-dimensional visualization of crystal, volumetric and morphology data", urn:issn:0021-8898 **44**, 1272–1276 (2011).

[18]L. Pauling, *The nature of the chemical bond* (Cornel University Press, 1960).

[19]K. Zhang, Y. Feng, F. Wang, Z. Yang, and J. Wang, "Two dimensional hexagonal boron nitride (2D-hBN): Synthesis, properties and applications", Journal of Materials Chemistry C **5**, 11992–12022 (2017).

[20]W. Olovsson and M. Magnuson, "Rhombohedral and Turbostratic Boron Nitride Polytypes Investigated by X-ray Absorption Spectroscopy", Journal of Physical Chemistry C **126**, 21101–21108 (2022).

[21]M. Moret, A. Rousseau, P. Valvin, S. Sharma, L. Souqui, H. Pedersen, H. Högberg, G. Cassabois, J. Li, J. H. Edgar, and B. Gil, "Rhombohedral and turbostratic boron nitride: X-ray diffraction and photoluminescence signatures", Applied Physics Letters **119**, 262102 (2021).

[22]G. R. Bhimanapati, N. R. Glavin, and J. A. Robinson, "2D Boron Nitride: Synthesis and Applications", Semiconductors and Semimetals **95**, 101–147 (2016).

[23]B. Gil, W. Desrat, A. Rousseau, C. Elias, P. Valvin, M. Moret, J. Li, E. Janzen, J. H. Edgar, and G. Cassabois, "Polytypes of sp2-Bonded Boron Nitride", Crystals **12**, 10.3390/cryst12060782 (2022).

[24]J. Iwański et al., "Revealing polytypism in 2d boron nitride with uv photoluminescence", npj 2D Materials and Applications 2024 8:1 **8**, 1–9 (2024).

[25]K. Watanabe, T. Taniguchi, and H. Kanda, "Direct-bandgap properties and evidence for ultraviolet lasing of hexagonal boron nitride single crystal", Nature Materials **3**, 404–409 (2004).

[26]T. Taniguchi and K. Watanabe, "Synthesis of high-purity boron nitride single crystals under high pressure by using Ba–BN solvent", Journal of Crystal Growth **303**, 525–529 (2007).

[27]T. Taniguchi and S. Yamaoka, "Spontaneous nucleation of cubic boron nitride single crystal by temperature gradient method under high pressure", Journal of Crystal Growth **222**, 549–557 (2001).

[28]G. Cassabois, P. Valvin, and B. Gil, "Hexagonal boron nitride is an indirect bandgap semiconductor", Nature Photonics **10**, 262–266 (2016).

[29]T. B. Hoffman, B. Clubine, Y. Zhang, K. Snow, and J. H. Edgar, "Optimization of Ni–Cr flux growth for hexagonal boron nitride single crystals", Journal of Crystal Growth **393**, 114–118 (2014).

[30]S. Liu, R. He, Z. Ye, X. Du, J. Lin, H. Jiang, B. Liu, and J. H. Edgar, "Large-Scale Growth of High-Quality Hexagonal Boron Nitride Crystals at Atmospheric Pressure from an Fe–Cr Flux", Crystal Growth & Design **17**, 4932–4935 (2017).

[31]L. Schué, I. Stenger, F. Fossard, A. Loiseau, and J. Barjon, "Characterization methods dedicated to nanometer-thick hBN layers", 2D Materials **4**, 015028 (2016).

[32]L. Schué, L. Sponza, A. Plaud, H. Bensalah, K. Watanabe, T. Taniguchi, F. Ducastelle, A. Loiseau, and J. Barjon, "Bright Luminescence from Indirect and Strongly Bound Excitons in h-BN", Physical Review Letters **122**, 067401 (2019).

[33]J. O. Carlsson and P. M. Martin, "Chemical Vapor Deposition", Handbook of Deposition Technologies for Films and Coatings: Science, Applications and Technology, 314–363 (2009).

[34]K. K. Kim, A. Hsu, X. Jia, S. M. Kim, Y. Shi, M. Hofmann, D. Nezich, J. F. Rodriguez-Nieva, M. Dresselhaus, T. Palacios, and J. Kong, "Synthesis of monolayer hexagonal boron nitride on Cu foil using chemical vapor deposition", Nano Letters **12**, 161–166 (2012).

[35]G. Kim, A. R. Jang, H. Y. Jeong, Z. Lee, D. J. Kang, and H. S. Shin, "Growth of high-crystalline, single-layer hexagonal boron nitride on recyclable platinum foil", Nano Letters **13**, 1834–1839 (2013).

[36]M. Gao et al., "Catalyst-free growth of two-dimensional hexagonal boron nitride few-layers on sapphire for deep ultraviolet photodetectors", Journal of Materials Chemistry C 7, 14999–15006 (2019).

[37]T.-A. Chen, C.-P. Chuu, C.-C. Tseng, C.-K. Wen, H.-S. P. Wong, S. Pan, R. Li, T.-A. Chao, W.-C. Chueh, Y. Zhang, Q. Fu, B. I. Yakobson, W.-H. Chang, and L.-J. Li, "Wafer-scale single-crystal hexagonal boron nitride monolayers on Cu (111)", Nature **579**, 219–223 (2020).

[38]Y. Wang et al., "Ultraflat single-crystal hexagonal boron nitride for wafer-scale integration of a 2D-compatible high-κ metal gate", Nature Materials **23**, 1495–1501 (2024).

[39]K. Y. Ma et al., "Epitaxial single-crystal hexagonal boron nitride multilayers on Ni (111)", Nature **606**, 88–93 (2022).

[40]S. Fukamachi, P. Solís-Fernández, K. Kawahara, D. Tanaka, T. Otake, Y. C. Lin, K. Suenaga, and H. Ago, "Large-area synthesis and transfer of multilayer hexagonal boron nitride for enhanced graphene device arrays", Nature Electronics **6**, 126–136 (2023).

[41]Y. Yuan, J. Weber, J. Li, B. Tian, Y. Ma, X. Zhang, T. Taniguchi, K. Watanabe, and M. Lanza, "On the quality of commercial chemical vapour deposited hexagonal boron nitride", Nature Communications **15**, 1–12 (2024).

[42]S. Nakhaie, J. M. Wofford, T. Schumann, U. Jahn, M. Ramsteiner, M. Hanke, J. M. Lopes, and H. Riechert, "Synthesis of atomically thin hexagonal boron nitride films on nickel foils by molecular beam epitaxy", Applied Physics Letters **106**, 213108 (2015).

[43]J. Wrigley, J. Bradford, T. James, T. S. Cheng, J. Thomas, C. J. Mellor, A. N. Khlobystov, L. Eaves, C. T. Foxon, S. V. Novikov, and P. H. Beton, "Epitaxy of boron nitride monolayers for graphene-based lateral heterostructures", 2D Materials **8**, 034001 (2021).

[44]R. Page, J. Casamento, Y. Cho, S. Rouvimov, H. G. Xing, and D. Jena, "Rotationally aligned hexagonal boron nitride on sapphire by high-temperature molecular beam epitaxy", Phys. Rev. Mater. **3**, 064001 (2019).

[45]M. J. Molaei, M. Younas, and M. Rezakazemi, "A Comprehensive Review on Recent Advances in Two-Dimensional (2D) Hexagonal Boron Nitride", ACS Applied Electronic Materials **3**, 5165–5187 (2021).

[46]L. H. Li and Y. Chen, "Atomically Thin Boron Nitride: Unique Properties and Applications", Advanced Functional Materials **26**, 2594–2608 (2016).

[47]B. Yates, M. J. Overy, and O. Pirgon, "The anisotropic thermal expansion of boron nitride", Philosophical Magazine **32**, 847–857 (1975).

[48]C. Elias, P. Valvin, T. Pelini, A. Summerfield, C. J. Mellor, T. S. Cheng, L. Eaves, C. T. Foxon, P. H. Beton, S. V. Novikov, B. Gil, and G. Cassabois, "Direct band-gap crossover in epitaxial monolayer boron nitride", Nature Communications **10**, 1–7 (2019).

[49]R. J. Nemanich, S. A. Solin, and R. M. Martin, "Light scattering study of boron nitride microcrystals", Physical Review B **23**, 6348–6356 (1981).

[50]R. Cuscó, J. Pellicer-Porres, J. H. Edgar, J. Li, A. Segura, and L. Artús, "Pressure dependence of the interlayer and intralayer E2g Raman-active modes of hexagonal BN up to the wurtzite phase transition", Physical Review B **102**, 075206 (2020).

[51]F. Jelezko and J. Wrachtrup, "Single defect centres in diamond: a review", Phys. Status Solidi a **203**, 3207–3225 (2006).

[52]L. Rondin, J. P. Tetienne, T. Hingant, J. F. Roch, P. Maletinsky, and V. Jacques, "Magnetometry with nitrogen-vacancy defects in diamond", Reports on Progress in Physics 77, 056503 (2014).

[53]S. H. Kim, K. H. Park, Y. G. Lee, S. J. Kang, Y. Park, and Y. D. Kim, "Color Centers in Hexagonal Boron Nitride", Nanomaterials **13**, 2344 (2023).

[54]H. Ngoc My Duong, M. A. P. Nguyen, M. Kianinia, T. Ohshima, H. Abe, K. Watanabe, T. Taniguchi, J. H. Edgar, I. Aharonovich, and M. Toth, "Effects of High-Energy Electron Irradiation on Quantum Emitters in Hexagonal Boron Nitride", ACS applied materials & interfaces **10**, 24886–24891 (2018).

[55]T. T. Tran, K. Bray, M. J. Ford, M. Toth, and I. Aharonovich, "Quantum emission from hexagonal boron nitride monolayers", Nature Nanotechnology **11**, 37–41 (2016).

[56]A. Gottscholl, M. Kianinia, V. Soltamov, S. Orlinskii, G. Mamin, C. Bradac, C. Kasper, K. Krambrock, A. Sperlich, M. Toth, I. Aharonovich, and V. Dyakonov, "Initialization and read-out of intrinsic spin defects in a van der Waals crystal at room temperature", Nature Materials **19**, 540–545 (2020).

[57]I. Aharonovich, D. Englund, and M. Toth, "Solid-state single-photon emitters", Nature Photonics **10**, 631–641 (2016).

[58]E. Glushkov, M. Macha, E. Räth, V. Navikas, N. Ronceray, C. Y. Cheon, A. Ahmed, A. Avsar, K. Watanabe, T. Taniguchi, I. Shorubalko, A. Kis, G. Fantner, and A. Radenovic, "Engineering Optically Active Defects in Hexagonal Boron Nitride Using Focused Ion Beam and Water", ACS Nano **16**, 3695–3703 (2022).

[59]H. Zhang, M. Lan, G. Tang, F. Chen, Z. Shu, F. Chen, and M. Li, "Discrete color centers in two-dimensional hexagonal boron nitride induced by fast neutron irradiation", Journal of Materials Chemistry C **7**, 12211–12216 (2019).

[60]S. Karankova, Y. Lee, C. Jang, Y. W. Song, and H. Moon, "One-Step Creation of Quantum Emitter Arrays in Hexagonal Boron Nitride by Local Stress Application", Advanced Optical Materials **13**, 2403018 (2024).

[61]C. Fournier, A. Plaud, S. Roux, A. Pierret, M. Rosticher, K. Watanabe, T. Taniguchi, S. Buil, X. Quélin, J. Barjon, J. P. Hermier, and A. Delteil, "Position-controlled quantum emitters with reproducible emission wavelength in hexagonal boron nitride", Nature Communications **12**, 1–6 (2021).

[62]D. Zhong, S. Gao, M. Saccone, J. R. Greer, M. Bernardi, S. Nadj-Perge, and A. Faraon, "Carbon-Related Quantum Emitter in Hexagonal Boron Nitride with Homogeneous Energy and 3-Fold Polarization", Nano Letters **24**, 1106–1113 (2024).

[63]H. L. Stern, C. M. Gilardoni, Q. Gu, S. Eizagirre Barker, O. F. Powell, X. Deng, S. A. Fraser, L. Follet, C. Li, A. J. Ramsay, H. H. Tan, I. Aharonovich, and M. Atatüre, "A quantum coherent spin in hexagonal boron nitride at ambient conditions", Nature Materials **23**, 1379–1385 (2024).

[64]J. Iwański, J. Kierdaszuk, A. Ciesielski, J. Binder, A. Drabińska, and A. Wysmołek, "Manipulating carbon related spin defects in boron nitride by changing the MOCVD growth temperature", Diamond and Related Materials **147**, 111291 (2024).

[65]W. Liu et al., "Spin-active defects in hexagonal boron nitride", Materials for Quantum Technology **2**, 032002 (2022).

[66]G. Noh, D. Choi, J. H. Kim, D. G. Im, Y. H. Kim, H. Seo, and J. Lee, "Stark Tuning of Single-Photon Emitters in Hexagonal Boron Nitride", Nano Letters **18**, 4710–4715 (2018).

[67]I. Zhigulin, J. Horder, V. Ivády, S. J. White, A. Gale, C. Li, C. J. Lobo, M. Toth, I. Aharonovich, and M. Kianinia, "Stark Effect of Blue Quantum Emitters in Hexagonal Boron Nitride", Physical Review Applied **19**, 044011 (2023).

[68]A. Basha, D.-A. Shaik, P. Palla, and D. Jenkins, "Electrical tuning of quantum light emitters in hBN for free space and telecom optical bands", Scientific Reports **14**, 1–17 (2024).

[69]M. Yu, D. Yim, H. Seo, and J. Lee, "Electrical charge control of h-BN single photon sources", 2D Materials **9**, 035020 (2022).

[70]S. J. White, T. Yang, N. Dontschuk, C. Li, Z. Q. Xu, M. Kianinia, A. Stacey, M. Toth, and I. Aharonovich, "Electrical control of quantum emitters in a Van der Waals heterostructure", Light: Science & Applications **11**, 1–9 (2022).

[71]J. P. So, H. R. Kim, H. Baek, K. Y. Jeong, H. C. Lee, W. Huh, Y. S. Kim, K. Watanabe, T. Taniguchi, J. Kim, C. H. Lee, and H. G. Park, "Electrically driven strain-induced deterministic single-photon emitters in a van der Waals heterostructure", Science Advances 7, eabj3176 (2021).

[72]T. Yang, N. Mendelson, C. Li, A. Gottscholl, J. Scott, M. Kianinia, V. Dyakonov, M. Toth, and I. Aharonovich, "Spin defects in hexagonal boron nitride for strain sensing on nanopillar arrays", Nanoscale **14**, 5239–5244 (2022).

[73]P. Udvarhelyi, T. Clua-Provost, A. Durand, J. Li, J. H. Edgar, B. Gil, G. Cassabois, V. Jacques, and A. Gali, "A planar defect spin sensor in a two-dimensional material susceptible to strain and electric fields", npj Computational Materials **9**, 1–8 (2023).

[74]X. Lyu, Q. Tan, L. Wu, C. Zhang, Z. Zhang, Z. Mu, J. Zúñiga-Pérez, H. Cai, and W. Gao, "Strain Quantum Sensing with Spin Defects in Hexagonal Boron Nitride", Nano Letters **22**, 6553–6559 (2022).

[75]M. Engler and B. Ruisinger, "Hexagonal Boron Nitride (hBN) – Applications from Metallurgy to cosmetics", Ceram. forum Int. **12**, 49–53 (2007).

[76]J. Li, X. Xiao, X. Xu, J. Lin, Y. Huang, Y. Xue, P. Jin, J. Zou, and C. Tang, "Activated boron nitride as an effective adsorbent for metal ions and organic pollutants", Scientific Reports **3**, 3208 (2013).

[77]S. B. Song, S. Yoon, S. Y. Kim, S. Yang, S. Y. Seo, S. Cha, H. W. Jeong, K. Watanabe, T. Taniguchi, G. H. Lee, J. S. Kim, M. H. Jo, and J. Kim, "Deep-ultraviolet electroluminescence and photocurrent generation in graphene/hBN/graphene heterostructures", Nature Communications **12**, 1–9 (2021).

[78]M. J. Allen, V. C. Tung, and R. B. Kaner, "Honeycomb carbon: A review of graphene", Chemical Reviews **110**, 132–145 (2010).

[79]S. Bae et al., "Roll-to-roll production of 30-inch graphene films for transparent electrodes", Nature Nanotechnology **5**, 574–578 (2010).

[80]F. Xia, D. B. Farmer, Y. M. Lin, and P. Avouris, "Graphene field-effect transistors with high on/off current ratio and large transport band gap at room temperature", Nano Letters **10**, 715–718 (2010).

[81]S. Joseph, J. Mohan, S. Lakshmy, S. Thomas, B. Chakraborty, S. Thomas, and N. Kalarikkal, "A review of the synthesis, properties, and applications of 2D transition metal dichalcogenides and their heterostructures", Materials Chemistry and Physics **297**, 127332 (2023).

[82]T. Chowdhury, E. C. Sadler, and T. J. Kempa, "Progress and Prospects in Transition-Metal Dichalcogenide Research beyond 2D", Chemical Reviews **120**, 12563–12591 (2020).

[83]K. F. Mak, C. Lee, J. Hone, J. Shan, and T. F. Heinz, "Atomically thin MoS_2: A new direct-gap semiconductor", Physical Review Letters **105**, 136805 (2010).

[84]A. Splendiani, L. Sun, Y. Zhang, T. Li, J. Kim, C. Y. Chim, G. Galli, and F. Wang, "Emerging photoluminescence in monolayer MoS_2", Nano Letters **10**, 1271–1275 (2010).

[85]J. K. Ellis, M. J. Lucero, and G. E. Scuseria, "The indirect to direct band gap transition in multilayered MoS_2 as predicted by screened hybrid density functional theory", Applied Physics Letters **99**, 43903 (2011).

[86]A. Chaves et al., "Bandgap engineering of two-dimensional semiconductor materials", npj 2D Materials and Applications **4**, 1–21 (2020).

[87]Z. Peng, X. Chen, Y. Fan, D. J. Srolovitz, and D. Lei, "Strain engineering of 2D semiconductors and graphene: from strain fields to band-structure tuning and photonic applications", Light: Science & Applications **9**, 1–25 (2020).

[88]J. Dong, Y. Zhao, and G. Ouyang, "The effect of alloying on the band engineering of two-dimensional transition metal dichalcogenides", Physica E: Low-dimensional Systems and Nanostructures **105**, 90–96 (2019).

[89]H. J. Conley, B. Wang, J. I. Ziegler, R. F. Haglund, S. T. Pantelides, and K. I. Bolotin, "Bandgap engineering of strained monolayer and bilayer MoS_2", Nano Letters **13**, 3626–3630 (2013).

[90]K. F. Mak, K. He, C. Lee, G. H. Lee, J. Hone, T. F. Heinz, and J. Shan, "Tightly bound trions in monolayer MoS_2", Nature Materials **12**, 207–211 (2013).

[91]M. Z. Bellus, F. Ceballos, H. Y. Chiu, and H. Zhao, "Tightly Bound Trions in Transition Metal Dichalcogenide Heterostructures", ACS Nano **9**, 6459–6464 (2015).

[92]X. Xu, W. Yao, D. Xiao, and T. F. Heinz, "Spin and pseudospins in layered transition metal dichalcogenides", Nature Physics **10**, 343–350 (2014).

[93]N. Zibouche, A. Kuc, J. Musfeldt, and T. Heine, "Transition-metal dichalcogenides for spintronic applications", Annalen der Physik **526**, 395–401 (2014).

[94]G. Scuri et al., "Electrically Tunable Valley Dynamics in Twisted WSe_2/WSe_2 Bilayers", Physical Review Letters **124**, 217403 (2020).

[95]G. Pacchioni, "Valleytronics with a twist", Nature Reviews Materials **5**, 480–480 (2020).

[96]K. Ludwiczak, E. Łacińska, J. Binder, I. Lutsyk, M. Rogala, P. Dąbrowski, Z. Klusek, R. Stepniewski, and A. Wysmołek, "Impeded phase transition in 1T-TaS_2: Thermoelectric fingerprint of long-lived mixed states", Solid State Communications **305**, 113749 (2020).

[97]Y. Nakata, K. Sugawara, A. Chainani, H. Oka, C. Bao, S. Zhou, P. Y. Chuang, C. M. Cheng, T. Kawakami, Y. Saruta, T. Fukumura, S. Zhou, T. Takahashi, and T. Sato, "Robust charge-density wave strengthened by electron correlations in monolayer 1T-$TaSe_2$ and 1T-$NbSe_2$", Nature Communications **12**, 1–9 (2021).

[98]Z. Fei, T. Palomaki, S. Wu, W. Zhao, X. Cai, B. Sun, P. Nguyen, J. Finney, X. Xu, and D. H. Cobden, "Edge conduction in monolayer WTe_2", Nature Physics **13**, 677–682 (2017).

[99]C. Xu, B. Li, W. Jiao, W. Zhou, B. Qian, R. Sankar, N. D. Zhigadlo, Y. Qi, D. Qian, F. C. Chou, and X. Xu, "Topological Type-II Dirac Fermions Approaching the Fermi Level in a Transition Metal Dichalcogenide $NiTe_2$", Chemistry of Materials **30**, 4823–4830 (2018).

[100]O. Lopez-Sanchez, D. Lembke, M. Kayci, A. Radenovic, and A. Kis, "Ultrasensitive photodetectors based on monolayer MoS_2", Nature Nanotechnology **8**, 497–501 (2013).

[101]A. Srivastava, M. Sidler, A. V. Allain, D. S. Lembke, A. Kis, and A. Imamoglu, "Optically active quantum dots in monolayer WSe_2", Nature Nanotechnology **10**, 491–496 (2015).

[102]M. Koperski, K. Nogajewski, A. Arora, V. Cherkez, P. Mallet, J. Y. Veuillen, J. Marcus, P. Kossacki, and M. Potemski, "Single photon emitters in exfoliated WSe_2 structures", Nature Nanotechnology **10**, 503–506 (2015).

[103]D. Fu et al., "Molecular Beam Epitaxy of Highly Crystalline Monolayer Molybdenum Disulfide on Hexagonal Boron Nitride", Journal of the American Chemical Society **139**, 9392–9400 (2017).

[104]K. Kang, S. Xie, L. Huang, Y. Han, P. Y. Huang, K. F. Mak, C. J. Kim, D. Muller, and J. Park, "High-mobility three-atom-thick semiconducting films with wafer-scale homogeneity", Nature **520**, 656–660 (2015).

[105]L. Seravalli and M. Bosi, "A Review on Chemical Vapour Deposition of Two-Dimensional MoS_2 Flakes", Materials **14**, 7590 (2021).

[106]N. Aspiotis, K. Morgan, B. März, K. Müller-Caspary, M. Ebert, E. Weatherby, M. E. Light, C. C. Huang, D. W. Hewak, S. Majumdar, and I. Zeimpekis, "Large-area synthesis of high electrical performance MoS_2 by a commercially scalable atomic layer deposition process", npj 2D Materials and Applications **7**, 1–11 (2023).

[107]Y. Zhang et al., "Direct observation of the transition from indirect to direct bandgap in atomically thin epitaxial $MoSe_2$", Nature Nanotechnology **9**, 111–115 (2014).

[108]P. Tonndorf, R. Schmidt, P. Böttger, X. Zhang, J. Börner, A. Liebig, M. Albrecht, C. Kloc, O. Gordan, D. R. T. Zahn, S. Michaelis de Vasconcellos, and R. Bratschitsch, "Photoluminescence emission and Raman response of monolayer MoS_2, $MoSe_2$, and WSe_2", Optics Express **21**, 4908 (2013).

[109]F. Cadiz et al., "Ultra-low power threshold for laser induced changes in optical properties of 2D molybdenum dichalcogenides", 2D Materials **3**, 045008 (2016).

[110]A. Eftekhari, "Molybdenum diselenide ($MoSe_2$) for energy storage, catalysis, and optoelectronics", Applied Materials Today **8**, 1–17 (2017).

[111]C. Kittel, *Introduction to solid state physics* (Wiley, 2005), p. 680.

[112]M. Gibertini, M. Koperski, A. F. Morpurgo, and K. S. Novoselov, "Magnetic 2D materials and heterostructures", Nature Nanotechnology **14**, 408–419 (2019).

[113]X. Jiang, Q. Liu, J. Xing, N. Liu, Y. Guo, Z. Liu, and J. Zhao, "Recent progress on 2D magnets: Fundamental mechanism, structural design and modification", Applied Physics Reviews **8**, 31305 (2021).

[114]N. D. Mermin and H. Wagner, "Absence of Ferromagnetism or Antiferromagnetism in One- or Two-Dimensional Isotropic Heisenberg Models", Physical Review Letters **17**, 1133 (1966).

[115]L. Onsager, "Crystal Statistics. I. A Two-Dimensional Model with an Order-Disorder Transition", Physical Review **65**, 117 (1944).

[116]J. M. Kosterlitz and D. J. Thouless, "Ordering, metastability and phase transitions in two-dimensional systems", Journal of Physics C: Solid State Physics **6**, 1181–1203 (1973).

[117]C. Gong et al., "Discovery of intrinsic ferromagnetism in two-dimensional van der Waals crystals", Nature **546**, 265–269 (2017).

[118]B. Huang, G. Clark, E. Navarro-Moratalla, D. R. Klein, R. Cheng, K. L. Seyler, D. Zhong, E. Schmidgall, M. A. McGuire, D. H. Cobden, W. Yao, D. Xiao, P. Jarillo-Herrero, and X. Xu, "Layer-dependent ferromagnetism in a van der Waals crystal down to the monolayer limit", Nature **546**, 270–273 (2017).

[119]S. Jenkins, L. Rózsa, U. Atxitia, R. F. Evans, K. S. Novoselov, and E. J. Santos, "Breaking through the Mermin-Wagner limit in 2D van der Waals magnets", Nature Communications **13**, 1–8 (2022).

[120]A. J. Freeman and R. E. Watson, "Theory of Direct Exchange in Ferromagnetism", Physical Review **124**, 1439 (1961).

[121]E. Koch, *Correlated Electrons: From Models to Materials*, Vol. 2 (Jülich, 2012), pp. 1–27.

[122]F. Liu et al., "Thermally annealed wafer-scale h-BN films grown on sapphire substrate by molecular beam epitaxy", Applied Physics Letters **116**, 142104 (2020).

[123]D. Lançon, R. A. Ewings, T. Guidi, F. Formisano, and A. R. Wildes, "Magnetic exchange parameters and anisotropy of the quasi-two-dimensional antiferromagnet $NiPS_3$", Physical Review B **98**, 134414 (2018).

[124]Q. Pei, X. C. Wang, J. J. Zou, and W. B. Mi, "Tunable electronic structure and magnetic coupling in strained two-dimensional semiconductor MnPSe3", Frontiers of Physics **13**, 1–8 (2018).

[125]N. C. Frey, A. Bandyopadhyay, H. Kumar, B. Anasori, Y. Gogotsi, and V. B. Shenoy, "Surface-Engineered MXenes: Electric Field Control of Magnetism and Enhanced Magnetic Anisotropy", ACS Nano **13**, 2831–2839 (2019).

[126]X. Jiang, A. V. Kuklin, A. Baev, Y. Ge, H. Ågren, H. Zhang, and P. N. Prasad, "Two-dimensional MXenes: From morphological to optical, electric, and magnetic properties and applications", Physics Reports **848**, 1–58 (2020).

[127]D. Soriano, M. I. Katsnelson, and J. Fernández-Rossier, "Magnetic Two-Dimensional Chromium Trihalides: A Theoretical Perspective", Nano Letters **20**, 6225–6234 (2020).

[128]K. W. Song, "Interlayer superexchange in bilayer chromium trihalides", Physical Review B **107**, 245133 (2023).

[129]Y. O. Kvashnin, A. Bergman, A. I. Lichtenstein, and M. I. Katsnelson, "Relativistic exchange interactions in CrX_3 (X=Cl, Br, I) monolayers", Physical Review B **102**, 115162 (2020).

[130]Y. Sun, R. C. Xiao, G. T. Lin, R. R. Zhang, L. S. Ling, Z. W. Ma, X. Luo, W. J. Lu, Y. P. Sun, and Z. G. Sheng, "Effects of hydrostatic pressure on spin-lattice coupling in two-dimensional ferromagnetic $Cr_2Ge_2Te_6$", Applied Physics Letters **112**, 072409 (2018).

[131]N. Sivadas, M. W. Daniels, R. H. Swendsen, S. Okamoto, and D. Xiao, "Magnetic ground state of semiconducting transition-metal trichalcogenide monolayers", Physical Review B **91**, 235425 (2015).

[132]C. Zener, "Interaction between the d-Shells in the Transition Metals. II. Ferromagnetic Compounds of Manganese with Perovskite Structure", Physical Review **82**, 403 (1951).

[133]X. Zhang, B. Wang, Y. Guo, Y. Zhang, Y. Chen, and J. Wang, "High Curie temperature and intrinsic ferromagnetic half-metallicity in two-dimensional Cr_3X_4 (X = S, Se, Te) nanosheets", Nanoscale Horizons **4**, 859–866 (2019).

[134]M. A. Ruderman and C. Kittel, "Indirect Exchange Coupling of Nuclear Magnetic Moments by Conduction Electrons", Physical Review **96**, 99–102 (1954).

[135]K. Yosida, "Magnetic Properties of Cu-Mn Alloys", Physical Review **106**, 893–898 (1957).

[136]T. Kasuya, "A Theory of Metallic Ferro- and Antiferromagnetism on Zener's Model", Progress of Theoretical Physics **16**, 45–57 (1956).

[137]L. B. Robinson, L. N. Ferguson, and F. Milstein, "Indirect Exchange Coupling of Magnetic Moments in Rare-Earth Metals", Physical Review B **3**, 1025 (1971).

[138]D. Zhang, A. Rahman, W. Qin, X. Li, P. Cui, Z. Zhang, and Z. Zhang, "Prediction of $MnSiTe_3$ as an intrinsic layered half-metal", Physical Review B **101**, 205119 (2020).

[139]K. H. J. Buschow and F. R. de Boer, *Physics of Magnetism and Magnetic Materials* (Springer US, 2003).

[140]N. Maksimovic, R. Day, A. Liebman-Peláez, F. Wan, N. H. Jo, C. Jozwiak, A. Bostwick, E. Rotenberg, S. Griffin, J. Singleton, and J. G. Analytis, "Strongly correlated itinerant magnetism near superconductivity in $NiTa_4Se_8$", Physical Review B **106**, 224429 (2022).

[141]H. Dai, M. Cai, Q. Hao, Q. Liu, Y. Xing, H. Chen, X. Chen, X. Wang, H. H. Fu, and J. Han, "Nonlocal Manipulation of Magnetism in an Itinerant Two-Dimensional Ferromagnet", ACS Nano **16**, 12437–12444 (2022).

[142]E. Vatansever, S. Sarikurt, and R. F. Evans, "Hysteresis features of the transition-metal dichalcogenides VX_2 (X = S, Se, and Te)", Materials Research Express **5**, 046108 (2018).

[143]M. Bonilla, S. Kolekar, Y. Ma, H. C. Diaz, V. Kalappattil, R. Das, T. Eggers, H. R. Gutierrez, M. H. Phan, and M. Batzill, "Strong room-temperature ferromagnetism in VSe_2 monolayers on van der Waals substrates", Nature Nanotechnology **13**, 289–293 (2018).

[144]H. H. Kim et al., "Evolution of interlayer and intralayer magnetism in three atomically thin chromium trihalides", Proceedings of the National Academy of Sciences of the United States of America **166**, 11131–11136 (2019).

[145]D. Ghazaryan et al., "Magnon-assisted tunnelling in van der Waals heterostructures based on CrBr3", Nature Electronics **1**, 344–349 (2018).

[146]D. Zhong, K. L. Seyler, X. Linpeng, N. P. Wilson, T. Taniguchi, K. Watanabe, M. A. McGuire, K. M. C. Fu, D. Xiao, W. Yao, and X. Xu, "Layer-resolved magnetic proximity effect in van der Waals heterostructures", Nature Nanotechnology **15**, 187–191 (2020).

[147]C. Tang, Z. Zhang, S. Lai, Q. Tan, and W. b. Gao, "Magnetic Proximity Effect in Graphene/$CrBr_3$ van der Waals Heterostructures", Advanced Materials **32**, 1908498 (2020).

[148]K. L. Seyler, D. Zhong, B. Huang, X. Linpeng, N. P. Wilson, T. Taniguchi, K. Watanabe, W. Yao, D. Xiao, M. A. McGuire, K. M. C. Fu, and X. Xu, "Valley Manipulation by Optically Tuning the Magnetic Proximity Effect in WSe_2/CrI_3 Heterostructures", Nano Letters **18**, 3823–3828 (2018).

[149]T. P. Lyons, D. Gillard, A. Molina-Sánchez, A. Misra, F. Withers, P. S. Keatley, A. Kozikov, T. Taniguchi, K. Watanabe, K. S. Novoselov, J. Fernández-Rossier, and A. I. Tartakovskii, "Interplay between spin proximity effect and charge-dependent exciton dynamics in $MoSe_2$/$CrBr_3$ van der Waals heterostructures", Nature Communications **11**, 1–9 (2020).

[150]J. Lee, T. Y. Ko, J. H. Kim, H. Bark, B. Kang, S. G. Jung, T. Park, Z. Lee, S. Ryu, and C. Lee, "Structural and Optical Properties of Single- and Few-Layer Magnetic Semiconductor $CrPS_4$", ACS Nano **11**, 10935–10944 (2017).

[151]Y. Peng et al., "Magnetic Structure and Metamagnetic Transitions in the van der Waals Antiferromagnet $CrPS_4$", Advanced Materials **32**, 2001200 (2020).

[152]A. Louisy, G. Ouvrard, D. M. Schleich, and R. Brec, "Physical properties and lithium intercalates of $CrPS_4$", Solid State Communications **28**, 61–66 (1978).

[153]E. Kroumova, M. L. Aroyo, J. M. Perez-Mato, A. Kirov, C. Capillas, S. Ivantchev, and H. Wondratschek, "Bilbao Crystallographic Server: Useful databases and tools for phase-transition studies", Phase Transitions **76**, 155–170 (2003).

[154]S. N. Neal, K. R. O'Neal, A. V. Haglund, D. G. Mandrus, H. A. Bechtel, G. L. Carr, K. Haule, D. Vanderbilt, H. S. Kim, and J. L. Musfeldt, "Exploring few and single layer $CrPS_4$ with near-field infrared spectroscopy", 2D Materials **8**, 035020 (2021).

[155]R. A. Susilo, B. G. Jang, J. Feng, Q. Du, Z. Yan, H. Dong, M. Yuan, C. Petrovic, J. H. Shim, D. Y. Kim, and B. Chen, "Band gap crossover and insulator–metal transition in the compressed layered $CrPS_4$", npj Quantum Materials **5**, 1–8 (2020).

[156]Q. L. Pei, X. Luo, G. T. Lin, J. Y. Song, L. Hu, Y. M. Zou, L. Yu, W. Tong, W. H. Song, W. J. Lu, and Y. P. Sun, "Spin dynamics, electronic and thermal transport properties of two-dimensional $CrPS_4$ single crystal", Journal of Applied Physics **119**, 043902 (2016).

[157]J. Son et al., "Air-Stable and Layer-Dependent Ferromagnetism in Atomically Thin van der Waals $CrPS_4$", ACS Nano **15**, 16904–16912 (2021).

[158]H. L. Zhuang and J. Zhou, "Density functional theory study of bulk and single-layer magnetic semiconductor $CrPS_4$", Physical Review B **94**, 195307 (2016).

[159]R. Wu, A. Ross, S. Ding, Y. Peng, F. He, Y. Ren, R. Lebrun, Y. Wu, Z. Wang, J. Yang, A. Brataas, and M. Kläui, "Magnetotransport Study of van der Waals $CrPS_4$/ (Pt,Pd) Heterostructures: Spin-Flop Transition and Room-Temperature Anomalous Hall Effect", Physical Review Applied **17**, 064038 (2022).

[160]F. Wu, M. Gibertini, K. Watanabe, T. Taniguchi, I. Gutiérrez-Lezama, N. Ubrig, and A. F. Morpurgo, "Gate-Controlled Magnetotransport and Electrostatic Modulation of Magnetism in 2D Magnetic Semiconductor $CrPS_4$", Advanced Materials **35**, 2211653 (2023).

[161]J. Y. Seo, S. Lim, H. J. Shin, K. W. Jeong, J. M. Hong, K. Moon, M. K. Kim, N. Lee, and Y. J. Choi, "Probing the weak limit of magnetocrystalline anisotropy through a spin–flop transition in the van der Waals antiferromagnet $CrPS_4$", NPG Asia Materials **16**, 1–9 (2024).

[162]M. J. Houmes, S. Mañas-Valero, A. Bermejillo-Seco, E. Coronado, P. G. Steeneken, and H. S. van der Zant, "Highly Anisotropic Mechanical Response of the Van der Waals Magnet $CrPS_4$", Advanced Functional Materials **34**, 2310206 (2024).

[163]T. Fas, M. Wlazło, M. Birowska, M. Rybak, M. Zinkiewicz, L. Oleschko, M. Goryca, Ł. Gondek, B. Camargo, J. Szczytko, A. K. Budniak, Y. Amouyal, E. Lifshitz, and J. Suffczyński, "Direct Optical Probing of the Magnetic Properties of the Layered Antiferromagnet $CrPS_4$", 10.48550/arXiv.2407.17912 (2024).

[164]J. A. Venables, G. D. T. Spiller, and M. Hanbucken, "Nucleation and growth of thin films", Reports on Progress in Physics **47**, 399 (1984).

[165]A. Pimpinelli and J. Villain, *Physics of crystal growth* (Cambridge University Press, 1998), p. 377.

[166]W. J. Lorenz and G. Staikov, "2D and 3D thin film formation and growth mechanisms in metal electrocrystallization – an atomistic view by in situ STM", Surface Science **335**, 32–43 (1995).

[167]K. Pakuła, A. Dabrowska, M. Tokarczyk, R. Bożek, J. Binder, G. Kowalski, A. Wysmołek, and R. Stepniewski, "Fundamental mechanisms of hBN growth by MOVPE", arXiv:1906.05319 (2019).

[168]Y. Kobayashi and T. Akasaka, "Hexagonal BN epitaxial growth on (0 0 0 1) sapphire substrate by MOVPE", Journal of Crystal Growth **310**, 5044–5047 (2008).

[169]S. Sundaram, P. Vuong, A. Mballo, T. Ayari, S. Karrakchou, G. Patriarche, P. L. Voss, J. P. Salvestrini, and A. Ougazzaden, "MOVPE of GaN-based mixed dimensional heterostructures on wafer-scale layered 2D hexagonal boron nitride - A key enabler of III-nitride flexible optoelectronics", APL Materials **9**, 061101 (2021).

[170]D. Chugh, J. Wong-Leung, L. Li, M. Lysevych, H. H. Tan, and C. Jagadish, "Flow modulation epitaxy of hexagonal boron nitride", 2D Materials **5**, 045018 (2018).

[171]A. K. Dąbrowska, M. Tokarczyk, G. Kowalski, J. Binder, R. Bożek, J. Borysiuk, R. Stepniewski, and A. Wysmołek, "Two stage epitaxial growth of wafer-size multilayer h-BN by metal-organic vapor phase epitaxy - A homoepitaxial approach", 2D Materials **8**, 15017 (2020).

[172]J. M. Chalmers and P. R. Griffiths, *Volume 1. Theory and Instrumentation, Handbook of Vibrational Spectroscopy*, Vol. 1 (John Wiley and Sons, Ltd, 2002).

[173]D. C. Harris and M. D. Bertolucci, "Symmetry and spectroscopy : an introduction to vibrational and electronic spectroscopy", 550 (1989).

[174]A. Smekal, "Zur Quantentheorie der Dispersion", Naturwissenschaften **11**, 873–875 (1923).

[175]C. V. Raman and K. S. Krishnan, "A new type of secondary radiation", Nature **121**, 501–502 (1928).

[176]M. Tsuboi, J. M. Benevides, and G. J. Thomas, "Raman Tensors and their application in structural studies of biological systems", Proceedings of the Japan Academy. Series B, Physical and Biological Sciences **85**, 83 (2009).

[177]C. F. Coll and C. F. Melius, "Theoretical calculation of Raman scattering cross sections for use in flame analysis", 10.2172/7364420 (1976).

[178]A. Oleś, *Metody doświadczalne fizyki ciała stałego* (Wydawawnictwa Naukowo-Techniczne, 1998).

[179]R. Saito, Y. Tatsumi, S. Huang, X. Ling, and M. S. Dresselhaus, "Raman spectroscopy of transition metal dichalcogenides", Journal of Physics. Condensed Matter **28**, 353002 (2016).

[180]A. Jorio, R. Saito, G. Dresselhaus, and M. S. Dresselhaus, *Raman Spectroscopy in Graphene Related Systems* (Wiley-VCH, Jan. 2011).

[181]M. Bogaard and R. H. and, "Raman intensities and cartesian polarizability derivatives", Molecular Physics **41**, 1281–1289 (1980).

[182]A. C. Ferrari, J. C. Meyer, V. Scardaci, C. Casiraghi, M. Lazzeri, F. Mauri, S. Piscanec, D. Jiang, K. S. Novoselov, S. Roth, and A. K. Geim, "Raman spectrum of graphene and graphene layers", Physical Review Letters **97**, 187401 (2006).

[183]C. Lee, H. Yan, L. E. Brus, T. F. Heinz, J. Hone, and S. Ryu, "Anomalous lattice vibrations of single- and few-layer MoS_2", ACS Nano **4**, 2695–2700 (2010).

[184]Y. Ding, W. Zheng, Z. Lin, Y. Zhu, R. Zhu, M. Jin, and F. Huang, "Raman tensor of layered MoS_2", Optics Letters **45**, 1313–1316 (2020).

[185]I. P. Herman, "Chapter 14 - photoluminescence", in *Optical diagnostics for thin film processing*, edited by I. P. Herman (Academic Press, San Diego, 1996), pp. 619–636.

[186]J. Wang, J. Ardelean, Y. Bai, A. Steinhoff, M. Florian, F. Jahnke, X. Xu, M. Kira, J. Hone, and X. Y. Zhu, "Optical generation of high carrier densities in 2D semiconductor heterobilayers", Science Advances **5**, eaax0145 (2019).

[187]J. Xiao, M. Zhao, Y. Wang, and X. Zhang, "Excitons in atomically thin 2D semiconductors and their applications", Nanophotonics **6**, 1309–1328 (2017).

[188]T. Mueller and E. Malic, "Exciton physics and device application of two-dimensional transition metal dichalcogenide semiconductors", npj 2D Materials and Applications **2**, 1–12 (2018).

[189]N. P. Wilson, W. Yao, J. Shan, and X. Xu, "Excitons and emergent quantum phenomena in stacked 2D semiconductors", Nature **599**, 383–392 (2021).

[190]M. Amani et al., "Near-unity photoluminescence quantum yield in MoS_2", Science **350**, 1065–1068 (2015).

[191]A. Kormányos, G. Burkard, M. Gmitra, J. Fabian, V. Zólyomi, N. D. Drummond, and V. Fal'ko, "k·p theory for two-dimensional transition metal dichalcogenide semiconductors", 2D Materials **2**, 022001 (2015).

[192]T. Cao, G. Wang, W. Han, H. Ye, C. Zhu, J. Shi, Q. Niu, P. Tan, E. Wang, B. Liu, and J. Feng, "Valley-selective circular dichroism of monolayer molybdenum disulphide", Nature Communications **3**, 1–5 (2012).

[193]H. Zeng, J. Dai, W. Yao, D. Xiao, and X. Cui, "Valley polarization in MoS_2 monolayers by optical pumping", Nature Nanotechnology **7**, 490–493 (2012).

[194]A. O. Slobodeniuk, P. Koutenský, M. Bartoš, F. Trojánek, P. Malý, T. Novotný, and M. Kozák, "Ultrafast valley-selective coherent optical manipulation with excitons in WSe_2 and MoS_2 monolayers", npj 2D Materials and Applications **7**, 1–7 (2023).

[195]J. R. Schaibley, H. Yu, G. Clark, P. Rivera, J. S. Ross, K. L. Seyler, W. Yao, and X. Xu, "Valleytronics in 2D materials", Nature Reviews Materials **1**, 1–15 (2016).

[196]M. A. Lampert, "Mobile and immobile effective-mass-particle complexes in nonmetallic solids", Phys. Rev. Lett. **1**, 450–453 (1958).

[197]P. Y. Yu and M. Cardona, *Fundamentals of semiconductors: physics and materials properties* (Springer, 2010), p. 775.

[198]M. I. Dyakonov, *Spin physics in semiconductors*, edited by M. I. Dyakonov, Vol. 157 (Springer International Publishing, 2017).

[199]T. Deilmann and K. S. Thygesen, "Interlayer Trions in the MoS_2/WS_2 van der Waals Heterostructure", Nano Letters **18**, 1460–1465 (2018).

[200]J. S. Ross, S. Wu, H. Yu, N. J. Ghimire, A. M. Jones, G. Aivazian, J. Yan, D. G. Mandrus, D. Xiao, W. Yao, and X. Xu, "Electrical control of neutral and charged excitons in a monolayer semiconductor", Nature Communications **4**, 1–6 (2013).

[201]D. Newbury, D. Joy, C. Lyman, P. Echlin, E. Lifshin, J. Michae, J. Goldstein, and I. Charles, "ning Electron Micros id X-Ray Microanalysis", (2013).

[202]V. K. Zworykin, "The Scanning Electron Microscope", Scientific American **167**, 111–113 (1942).

[203]S. Roddaro, P. Pingue, V. Piazza, V. Pellegrini, and F. Beltram, "The optical visibility of graphene: Interference colors of ultrathin graphite on SiO_2", Nano Letters **7**, 2707–2710 (2007).

[204]M. Yi and Z. Shen, "A review on mechanical exfoliation for the scalable production of graphene", Journal of Materials Chemistry A **3**, 11700–11715 (2015).

[205]A. Castellanos-Gomez, M. Barkelid, A. M. Goossens, V. E. Calado, H. S. Van Der Zant, and G. A. Steele, "Laser-thinning of MoS_2: On demand generation of a single-layer semiconductor", Nano Letters **12**, 3187–3192 (2012).

[206]G. K. White and M. L. Minges, "Thermophysical properties of some key solids: An update", International Journal of Thermophysics **18**, 1269–1327 (1997).

[207]P. Tatarczak, J. Iwański, A. Krystyna Dąbrowska, M. Tokarczyk, J. Binder, R. Stepniewski, and A. Wysmołek, "Strain modulation of epitaxial h-BN on sapphire: the role of wrinkle formation for large-area two-dimensional materials", Nanotechnology **35**, 175703 (2023).

[208]J. Iwański, P. Tatarczak, M. Tokarczyk, A. K. Dąbrowska, J. Pawłowski, J. Binder, G. Kowalski, R. Stępniewski, and A. Wysmołek, "Temperature induced giant shift of phonon energy in epitaxial boron nitride layers", Nanotechnology **34**, 015202 (2022).

[209]J. Binder, A. K. Dąbrowska, M. Tokarczyk, K. Ludwiczak, R. Bożek, G. Kowalski, R. Stepniewski, and A. Wysmołek, "Epitaxial Hexagonal Boron Nitride for Hydrogen Generation by Radiolysis of Interfacial Water", Nano Letters **23**, 1267–1272 (2023).

[210]M. Tokarczyk, A. K. Dabrowska, G. Kowalski, R. Bożek, J. Iwański, J. Binder, R. Stepniewski, and A. Wysmołek, "Effective substrate for the growth of multilayer h-BN on sapphire–substrate off-cut, pre-growth, and post-growth conditions in metal-organic vapor phase epitaxy", 2D Materials **10**, 025010 (2023).

[211]M. Wang, H. Li, T. J. Ko, M. S. Shawkat, E. Okogbue, C. Yoo, S. S. Han, M. A. Islam, K. H. Oh, and Y. Jung, "Manufacturing strategies for wafer-scale two-dimensional transition metal dichalcogenide heterolayers", Journal of Materials Research **35**, 1350–1368 (2020).

[212]S. V. Mandyam, H. M. Kim, and M. Drndić, "Large area few-layer TMD film growths and their applications", Journal of Physics: Materials **3**, 024008 (2020).

[213]Y. Zhan, Z. Liu, S. Najmaei, P. M. Ajayan, and J. Lou, "Large-area vapor-phase growth and characterization of MoS_2 atomic layers on a SiO_2 substrate", Small **8**, 966–971 (2012).

[214]X. Duan, C. Wang, J. C. Shaw, R. Cheng, Y. Chen, H. Li, X. Wu, Y. Tang, Q. Zhang, A. Pan, J. Jiang, R. Yu, Y. Huang, and X. Duan, "Lateral epitaxial growth of two-dimensional layered semiconductor heterojunctions", Nature Nanotechnology **9**, 1024–1030 (2014).

[215]T. J. Dai, Y. Q. Chen, Z. Y. Zhou, J. Sun, X. S. Peng, and X. Z. Liu, "Two-dimensional $MoSe_2$/graphene heterostructure thin film with wafer-scale continuity via van der Waals epitaxy", Chemical Physics Letters **755**, 137762 (2020).

[216]S. W. Park, Y. J. Jo, S. Bae, B. H. Hong, and S. K. Lee, "Synthesis of Large-Scale Transition Metal Dichalcogenides for Their Commercialization", Applied Science and Convergence Technology **29**, 133–142 (2020).

[217]H. Li, X. Zhu, Z. K. Tang, and X. H. Zhang, "Low-temperature photoluminescence emission of monolayer MoS_2 on diverse substrates grown by CVD", Journal of Luminescence **199**, 210–215 (2018).

[218]T. Severs Millard, A. Genco, E. M. Alexeev, S. Randerson, S. Ahn, A. R. Jang, H. Suk Shin, and A. I. Tartakovskii, "Large area chemical vapour deposition grown transition metal dichalcogenide monolayers automatically characterized through photoluminescence imaging", npj 2D Materials and Applications **4**, 1–9 (2020).

[219]A. Delhomme, G. Butseraen, B. Zheng, L. Marty, V. Bouchiat, M. R. Molas, A. Pan, K. Watanabe, T. Taniguchi, A. Ouerghi, J. Renard, and C. Faugeras, "Magneto-spectroscopy of exciton Rydberg states in a CVD grown WSe_2 monolayer", Applied Physics Letters **114**, 232104 (2019).

[220]S. Shree, A. George, T. Lehnert, C. Neumann, M. Benelajla, C. Robert, X. Marie, K. Watanabe, T. Taniguchi, U. Kaiser, B. Urbaszek, and A. Turchanin, "High optical quality of MoS_2 monolayers grown by chemical vapor deposition", 2D Materials **7**, 015011 (2020).

[221]M. Marx, S. Nordmann, J. Knoch, C. Franzen, C. Stampfer, D. Andrzejewski, T. Kümmell, G. Bacher, M. Heuken, H. Kalisch, and A. Vescan, "Large-area MoS_2 deposition via MOVPE", Journal of Crystal Growth **464**, 100–104 (2017).

[222]E. Xenogiannopoulou, P. Tsipas, K. E. Aretouli, D. Tsoutsou, S. A. Giamini, C. Bazioti, G. P. Dimitrakopulos, P. Komninou, S. Brems, C. Huyghebaert, I. P. Radu, and A. Dimoulas, "High-quality, large-area $MoSe_2$ and $MoSe_2/Bi_2Se_3$ heterostructures on AlN(0001)/Si(111) substrates by molecular beam epitaxy", Nanoscale **7**, 7896–7905 (2015).

[223]Y. Wei, C. Hu, Y. Li, X. Hu, K. Yu, L. Sun, M. Hohage, and L. Sun, "Initial stage of MBE growth of $MoSe_2$ monolayer", Nanotechnology **31**, 315710 (2020).

[224]Y. Wei, C. Hu, Y. Li, X. Hu, M. Hohage, and L. Sun, "Growth oscillation of $MoSe_2$ monolayers observed by differential reflectance spectroscopy", Journal of Physics Condensed Matter **32**, 155001 (2020).

[225]A. Ohtake and Y. Sakuma, "Effect of Substrate Orientation on $MoSe_2$/GaAs Heteroepitaxy", Journal of Physical Chemistry C **124**, 5203 (2020).

[226]Z. He, T. Wei, W. Huang, W. Zhou, P. Hu, Z. Xie, H. Chen, S. Wu, and S. Li, "Electrostatically Enhanced Electron-Phonon Interaction in Monolayer 2H-$MoSe_2$ Grown by Molecular Beam Epitaxy", ACS Applied Materials and Interfaces **12**, 44067–44073 (2020).

[227]Y. Xia, J. Zhang, Z. Yu, Y. Jin, H. Tian, Y. Feng, B. Li, W. Ho, C. Liu, H. Xu, C. Jin, and M. Xie, "A Shallow Acceptor of Phosphorous Doped in $MoSe_2$ Monolayer", Advanced Electronic Materials **6**, 1900830 (2020).

[228]W. Pacuski et al., "Narrow Excitonic Lines and Large-Scale Homogeneity of Transition-Metal Dichalcogenide Monolayers Grown by Molecular Beam Epitaxy on Hexagonal Boron Nitride", Nano Letters **20**, 3058–3066 (2020).

[229]M. Grzeszczyk, K. Olkowska-Pucko, K. Nogajewski, K. Watanabe, T. Taniguchi, P. Kossacki, A. Babiński, and M. R. Molas, "Exposing the trion's fine structure by controlling the carrier concentration in hBN-encapsulated MoS_2", Nanoscale **13**, 18726–18733 (2021).

[230]A. Nagashima, N. Tejima, Y. Gamou, T. Kawai, and C. Oshima, "Electronic dispersion relations of monolayer hexagonal boron nitride formed on the Ni(111) surface", Physical Review B **51**, 4606–4613 (1995).

[231]R. Geick, C. H. Perry, and G. Rupprecht, "Normal modes in hexagonal boron nitride", Physical Review **146**, 543–547 (1966).

[232]F. Cadiz et al., "Excitonic linewidth approaching the homogeneous limit in MoS_2-based van der Waals heterostructures", Physical Review X **7**, 021026 (2017).

[233]L. Zhang et al., "Efficient and Layer-Dependent Exciton Pumping across Atomically Thin Organic–Inorganic Type-I Heterostructures", Advanced Materials **30**, 1803986 (2018).

[234]J. Ye, T. Yan, B. Niu, Y. Li, and X. Zhang, "Nonlinear dynamics of trions under strong optical excitation in monolayer $MoSe_2$", Scientific Reports **8**, 1–8 (2018).

[235]G. Wang, E. Palleau, T. Amand, S. Tongay, X. Marie, and B. Urbaszek, "Polarization and time-resolved photoluminescence spectroscopy of excitons in $MoSe_2$ monolayers", Applied Physics Letters **106**, 112101 (2015).

[236]J. Wierzbowski, J. Klein, F. Sigger, C. Straubinger, M. Kremser, T. Taniguchi, K. Watanabe, U. Wurstbauer, A. W. Holleitner, M. Kaniber, K. Müller, and J. J. Finley, "Direct exciton emission from atomically thin transition metal dichalcogenide heterostructures near the lifetime limit", Scientific Reports **7**, 1–6 (2017).

[237]R. M. Macfarlane, "Analysis of the Spectrum of d3 Ions in Trigonal Crystal Fields", The Journal of Chemical Physics **39**, 3118 (1963).

[238]T. Godde, D. Schmidt, J. Schmutzler, M. Aßmann, J. Debus, F. Withers, E. M. Alexeev, O. Del Pozo-Zamudio, O. V. Skrypka, K. S. Novoselov, M. Bayer, and A. I. Tartakovskii, "Exciton and trion dynamics in atomically thin $MoSe_2$ and WSe_2: Effect of localization", Physical Review B **94**, 165301 (2016).

[239]W. S. Yun, S. W. Han, S. C. Hong, I. G. Kim, and J. D. Lee, "Thickness and strain effects on electronic structures of transition metal dichalcogenides: 2H-MX_2 semiconductors (M = Mo, W; X = S, Se, Te)", Physical Review B **85**, 033305 (2012).

[240]J. Kierdaszuk, P. Kaźmierczak, R. Bożek, J. Grzonka, A. Krajewska, Z. Zytkiewicz, M. Sobanska, K. Klosek, A. Wołoś, M. Kamińska, A. Wysmołek, and A. Drabińska, "Surface-enhanced raman scattering of graphene caused by self-induced nanogating by gan nanowire array", Carbon **128**, 70–77 (2018).

[241]M. Cowie, R. Plougmann, Y. Benkirane, L. Schué, Z. Schumacher, and P. Grütter, "How high is a MoSe 2 monolayer?", Nanotechnology **33**, 125706 (2021).

[242]M. Heilmann, A. S. Prikhodko, M. Hanke, A. Sabelfeld, N. I. Borgardt, and J. M. J. Lopes, "Influence of Proximity to Supporting Substrate on van der Waals Epitaxy of Atomically Thin Graphene/Hexagonal Boron Nitride Heterostructures", ACS Applied Materials and Interfaces **12**, 8897–8907 (2020).

[243]M. Heilmann, V. Deinhart, A. Tahraoui, K. Höflich, and J. M. J. Lopes, "Spatially controlled epitaxial growth of 2D heterostructures via defect engineering using a focused He ion beam", npj 2D Materials and Applications **5**, 1–7 (2021).

[244]X. Zhang, F. Zhang, Y. Wang, D. S. Schulman, T. Zhang, A. Bansal, N. Alem, S. Das, V. H. Crespi, M. Terrones, and J. M. Redwing, "Defect-Controlled Nucleation and Orientation of WSe_2 on hBN: A Route to Single-Crystal Epitaxial Monolayers", ACS Nano **13**, 3341–3352 (2019).

[245]Y. C. Lin et al., "Direct synthesis of van der Waals solids", ACS Nano **8**, 3715–3723 (2014).

[246]N. Lundt, E. Cherotchenko, O. Iff, X. Fan, Y. Shen, P. Bigenwald, A. V. Kavokin, S. Höfling, and C. Schneider, "The interplay between excitons and trions in a monolayer of $MoSe_2$", Applied Physics Letters **112**, 031107 (2018).

[247]P. Soubelet, J. Klein, J. Wierzbowski, R. Silvioli, F. Sigger, A. V. Stier, K. Gallo, and J. J. Finley, "Charged Exciton Kinetics in Monolayer $MoSe_2$ near Ferroelectric Domain Walls in Periodically Poled $LiNbO_3$", Nano Letters **21**, 959–966 (2021).

[248]H. Naito, Y. Makino, W. Zhang, T. Ogawa, T. Endo, T. Sannomiya, M. Kaneda, K. Hashimoto, H. E. Lim, Y. Nakanishi, K. Watanabe, T. Taniguchi, K. Matsuda, and Y. Miyata, "High-throughput dry transfer and excitonic properties of twisted bilayers based on CVD-grown transition metal dichalcogenides", Nanoscale Advances **5**, 5115–5121 (2023).

[249]S. Singh, J. Deb, U. Sarkar, and S. Sharma, "$MoSe_2$ Crystalline Nanosheets for Room-Temperature Ammonia Sensing", ACS Applied Nano Materials **3**, 9375–9384 (2020).

[250]S. Nisar, G. Dastgeer, M. Shahzadi, Z. M. Shahzad, E. Elahi, A. Irfan, J. Eom, H. Kim, and D.-k. Kim, "Gate-assisted $MoSe_2$ transistor to detect the streptavidin via supporter molecule engineering", Materials Today Nano **24**, 100405 (2023).

[251]Y. Meng, T. Wang, C. Jin, Z. Li, S. Miao, Z. Lian, T. Taniguchi, K. Watanabe, F. Song, and S. F. Shi, "Electrical switching between exciton dissociation to exciton funneling in $MoSe_2/WS_2$ heterostructure", Nature Communications **11**, 1–6 (2020).

[252]F. Tagarelli, E. Lopriore, D. Erkensten, R. Perea-Causín, S. Brem, J. Hagel, Z. Sun, G. Pasquale, K. Watanabe, T. Taniguchi, E. Malic, and A. Kis, "Electrical control of hybrid exciton transport in a van der Waals heterostructure", Nature Photonics **17**, 615–621 (2023).

[253]K. Ludwiczak, A. K. Dąbrowska, J. Binder, M. Tokarczyk, J. Iwański, B. Kurowska, J. Turczyński, G. Kowalski, R. Bożek, R. Stępniewski, W. Pacuski, and A. Wysmołek, "Heteroepitaxial Growth of High Optical Quality, Wafer-Scale van der Waals Heterostrucutres", ACS Applied Materials & Interfaces **13**, 47904–47911 (2021).

[254]K. Ludwiczak, A. K. Dąbrowska, J. Kucharek, J. Rogoża, M. Tokarczyk, R. Bożek, M. Gryglas-Borysiewicz, T. Taniguchi, K. Watanabe, J. Binder, W. Pacuski, and A. Wysmołek, "Large-Area Growth of High-Optical-Quality $MoSe_2$/hBN Heterostructures with Tunable Charge Carrier Concentration", ACS Applied Materials & Interfaces **16**, 49701–49710 (2024).

[255]G. Baudler M. ; Brauer, *Handbuch der präparativen anorganischen chemie*, ger (Ferdinand Enke Verlag, Stuttgart, 1954).

[256]T. Su, M. Lohmann, J. Li, Y. Xu, B. Niu, M. Alghamdi, H. Zhou, Y. Cui, R. Cheng, T. Taniguchi, K. Watanabe, and J. Shi, "Current-induced CrI_3 surface spin-flop transition probed by proximity magnetoresistance in Pt", 2D Materials **7**, 045006 (2020).

[257]B. Huang, G. Clark, D. R. Klein, D. MacNeill, E. Navarro-Moratalla, K. L. Seyler, N. Wilson, M. A. McGuire, D. H. Cobden, D. Xiao, W. Yao, P. Jarillo-Herrero, and X. Xu, "Electrical control of 2D magnetism in bilayer CrI_3", Nature Nanotechnology **13**, 544–548 (2018).

[258]S. Jiang, L. Li, Z. Wang, K. F. Mak, and J. Shan, "Controlling magnetism in 2D CrI_3 by electrostatic doping", Nature Nanotechnology **13**, 549–553 (2018).

[259]M. J. Madou, *Fundamentals of Microfabrication*, 2nd ed. (CRC Press, Oct. 2018).

[260]G. Marin, "Inclined lithography and photoresist optimization for fabrication of 3D mesh structures", PhD thesis (Aalto University, Nov. 2014).

[261]N. V. Proscia, Z. Shotan, H. Jayakumar, P. Reddy, C. Cohen, M. Dollar, A. Alkauskas, M. Doherty, C. A. Meriles, and V. M. Menon, "Near-deterministic activation of room-temperature quantum emitters in hexagonal boron nitride", Optica **5**, 1128 (2018).

[262]M. Fischer, A. Sajid, J. Iles-Smith, A. Hötger, D. I. Miakota, M. K. Svendsen, C. Kastl, S. Canulescu, S. Xiao, M. Wubs, K. S. Thygesen, A. W. Holleitner, and N. Stenger, "Combining experiments on luminescent centres in hexagonal boron nitride with the polaron model and ab initio methods towards the identification of their microscopic origin", Nanoscale **15**, 14215 (2023).

[263]P. Khatri, I. J. Luxmoore, and A. J. Ramsay, "Phonon sidebands of color centers in hexagonal boron nitride", Physical review B **100**, 125305 (2019).

[264]D. Wigger, R. Schmidt, O. Del Pozo-Zamudio, J. A. Preuß, P. Tonndorf, R. Schneider, P. Steeger, J. Kern, Y. Khodaei, J. Sperling, S. M. De Vasconcellos, R. Bratschitsch, and T. Kuhn, "Phonon-assisted emission and absorption of individual color centers in hexagonal boron nitride", 2D Materials **6**, 035006 (2019).

[265]H. L. Stern, R. Wang, Y. Fan, R. Mizuta, J. C. Stewart, L. M. Needham, T. D. Roberts, R. Wai, N. S. Ginsberg, D. Klenerman, S. Hofmann, and S. F. Lee, "Spectrally Resolved Photodynamics of Individual Emitters in Large-Area Monolayers of Hexagonal Boron Nitride", ACS Nano **13**, 4538–4547 (2019).

[266]X. Li, G. D. Shepard, A. Cupo, N. Camporeale, K. Shayan, Y. Luo, V. Meunier, and S. Strauf, "Nonmagnetic Quantum Emitters in Boron Nitride with Ultranarrow and Sideband-Free Emission Spectra", ACS Nano **11**, 6652–6660 (2017).

[267]S. X. Li, T. Ichihara, H. Park, G. He, D. Kozawa, Y. Wen, V. B. Koman, Y. Zeng, M. Kuehne, Z. Yuan, S. Faucher, J. H. Warner, and M. S. Strano, "Prolonged photostability in hexagonal boron nitride quantum emitters", Communications Materials **4**, 1–11 (2023).

[268]J. Serrano, A. Bosak, R. Arenal, M. Krisch, K. Watanabe, T. Taniguchi, H. Kanda, A. Rubio, and L. Wirtz, "Vibrational properties of hexagonal boron nitride: Inelastic X-ray scattering and Ab Initio calculations", Physical Review Letters **98**, 095503 (2007).

[269]Z. Zhang, J. Shang, C. Jiang, A. Rasmita, W. Gao, and T. Yu, "Direct Photoluminescence Probing of Ferromagnetism in Monolayer Two-Dimensional CrBr 3", Nano Letters **19**, 3138–3142 (2019).

[270]Ł. Kipczak, A. Karmakar, M. Grzeszczyk, R. Janiszewska, T. Woźniak, Z. Chen, J. Pawłowski, K. Watanabe, T. Taniguchi, A. Babiński, M. Koperski, and M. R. Molas, "Resonant Raman scattering of few layers $CrBr_3$", Scientific Reports **14**, 1–10 (2024).

[271]A. L. Exarhos, D. A. Hopper, R. N. Patel, M. W. Doherty, and L. C. Bassett, "Magnetic-field-dependent quantum emission in hexagonal boron nitride at room temperature", Nature Communications **10**, 222 (2019).

[272]J. Wu, Y. Yao, M. L. Lin, M. Rösner, Z. Du, K. Watanabe, T. Taniguchi, P. H. Tan, S. Haas, and H. Wang, "Spin–Phonon Coupling in Ferromagnetic Monolayer Chromium Tribromide", Advanced Materials **34**, 2108506 (2022).

[273]M. Wu, Z. Li, and S. G. Louie, "Optical and magneto-optical properties of ferromagnetic monolayer $CrBr_3$: A first-principles GW and GW plus Bethe-Salpeter equation study", Physical Review Materials **6**, 014008 (2021).

[274]M. Grzeszczyk, S. Acharya, D. Pashov, Z. Chen, K. Vaklinova, M. van Schilfgaarde, K. Watanabe, T. Taniguchi, K. S. Novoselov, M. I. Katsnelson, and M. Koperski, "Strongly Correlated Exciton-Magnetization System for Optical Spin Pumping in $CrBr_3$ and CrI_3.", Advanced Materials **35**, 2209513 (2023).

[275]N. Mendelson et al., "Identifying carbon as the source of visible single-photon emission from hexagonal boron nitride", Nature Materials **20**, 321–328 (2021).

[276]A. Gale, D. Scognamiglio, I. Zhigulin, B. Whitefield, M. Kianinia, I. Aharonovich, and M. Toth, "Manipulating the Charge State of Spin Defects in Hexagonal Boron Nitride", Nano Letters **23**, 6141–6147 (2023).

[277]X. Chen et al., "Activated Single Photon Emitters And Enhanced Deep-Level Emissions in Hexagonal Boron Nitride Strain Crystal", Advanced Functional Materials **34**, 2306128 (2024).

[278]W. B. Zhang, Q. Qu, P. Zhu, and C. H. Lam, "Robust intrinsic ferromagnetism and half semiconductivity in stable two-dimensional single-layer chromium trihalides", Journal of Materials Chemistry C **3**, 12457–12468 (2015).

[279]D. P. Kozlenko, O. N. Lis, S. E. Kichanov, E. V. Lukin, N. M. Belozerova, and B. N. Savenko, "Spin-induced negative thermal expansion and spin–phonon coupling in van der Waals material $CrBr_3$", npj Quantum Materials 2021 6:1 **6**, 1–5 (2021).

[280]M. Balkanski, R. F. Wallis, and E. Haro, "Anharmonic effects in light scattering due to optical phonons in silicon", Physical Review B **28**, 1928–1934 (1983).

[281]S. Kim, S. Yoon, H. Ahn, G. Jin, H. Kim, M. H. Jo, C. Lee, J. Kim, and S. Ryu, "Photoluminescence Path Bifurcations by Spin Flip in Two-Dimensional $CrPS_4$", ACS Nano **16**, 16385–16393 (2022).

[282]P. Gu, Q. Tan, Y. Wan, Z. Li, Y. Peng, J. Lai, J. Ma, X. Yao, S. Yang, K. Yuan, D. Sun, B. Peng, J. Zhang, and Y. Ye, "Photoluminescent Quantum Interference in a van der Waals Magnet Preserved by Symmetry Breaking", ACS Nano **14**, 1003–1010 (2020).

[283]J. Rogoża, J. Binder, K. V. Voronin, I. Niehues, K. Ludwiczak, A. K. Dąbrowska, M. Tokarczyk, R. Bożek, A. Y. Nikitin, R. Hillenbrand, R. Stępniewski, and A. Wysmołek, "Polarisation-dependent Raman enhancement in hexagonal boron nitride membranes", Nanoscale **17**, 3053–3060 (2025).

[284]K. P. Korona, A. Wysmol/ek, K. Pakul/a, R. Stepniewski, J. M. Baranowski, I. Grzegory, B. L/ucznik, M. Wróblewski, and S. Porowski, "Exciton region reflectance of homoepitaxial gan layers", Applied Physics Letters **69**, 788–790 (1996).

[285]R. Cuscó, B. Gil, G. Cassabois, and L. Artús, "Temperature dependence of raman-active phonons and anharmonic interactions in layered hexagonal bn", Phys. Rev. B **94**, 155435 (2016).

[286]S. Calder, A. V. Haglund, Y. Liu, D. M. Pajerowski, H. B. Cao, T. J. Williams, V. O. Garlea, and D. Mandrus, "Magnetic structure and exchange interactions in the layered semiconductor $CrPS_4$", Physical Review B **102**, 10.1103/PhysRevB.102.024408 (2020).

[287]S. Kim, J. Lee, C. Lee, and S. Ryu, "Polarized Raman Spectra and Complex Raman Tensors of Antiferromagnetic Semiconductor $CrPS_4$", Journal of Physical Chemistry C **125**, 2691–2698 (2021).

[288]M. H. Nguyen, S. Son, G. Park, W. Na, J. G. Park, and H. Cheong, "Temperature dependent Raman study of antiferromagnetic $CrPS_4$", Journal of Materials Chemistry C **12**, 12468–12473 (2024).

[289]R. Cusco, B. Gil, G. Cassabois, L. Artus, A. Lluis, R. Cuscó, and L. Artús, "Temperature dependence of Raman-active phonons and anharmonic interactions in layered hexagonal BN ", BN. Physical Review B **94**, 155435 (2016).

[290]Y. Peng et al., "Controlling Spin Orientation and Metamagnetic Transitions in Anisotropic van der Waals Antiferromagnet $CrPS_4$ by Hydrostatic Pressure", Advanced Functional Materials **32**, 2106592 (2022).

[291]N. Paul, Y. Zhang, and L. Fu, "Giant proximity exchange and flat Chern band in 2D magnet-semiconductor heterostructures", Science Advances **9**, eabn1401 (2023).

[292]S. Guo, S. Germanis, T. Taniguchi, K. Watanabe, F. Withers, and I. J. Luxmoore, "Electrically Driven Site-Controlled Single Photon Source", ACS Photonics **10**, 2549–2555 (2023).

[293]M. Kianinia, C. Bradac, B. Sontheimer, F. Wang, T. T. Tran, M. Nguyen, S. Kim, Z. Q. Xu, D. Jin, A. W. Schell, C. J. Lobo, I. Aharonovich, and M. Toth, "All-optical control and super-resolution imaging of quantum emitters in layered materials", Nature Communications **9**, 1–8 (2018).

[294]D. Yim, M. Yu, G. Noh, J. Lee, and H. Seo, "Polarization and Localization of Single-Photon Emitters in Hexagonal Boron Nitride Wrinkles", ACS Applied Materials and Interfaces **12**, 36362–36369 (2020).

[295]M. Koperski, K. Nogajewski, and M. Potemski, "Single photon emitters in boron nitride: More than a supplementary material", Optics Communications **411**, 158–165 (2018).